Chemical rock weathering in North America as source of dissolved silica and sink of atmospheric CO$_2$

Dissertation zur Erlangung des Doktorgrades der Naturwissenschaften im

Fachbereich Geowissenschaften der Universität Hamburg

Vorgelegt von

Nils Jansen

aus

Aachen

Hamburg

2010

Als Dissertation angenommen vom Fachbereich Geowissenschaften der Universität Hamburg

Auf Grund der Gutachten von Prof. Dr Jens Hartmann

und Prof. Dr. Stephan Kempe

Hamburg, den 3.2.2010

_____
Professor Dr. Jürgen Oßenbrügge

Contents

List of Publications

The presented thesis is based on the work on studies which have been published or are prepared for publication in internationally peer reviewed journals. A list of publications the Ph.D.-candidate contributed to is given below. Individual contributions to those publications are given in Appendix E. The chapters 2.1 – 2.4 and 3 of the presented thesis are contained in Jansen et al. (2010) while chapter 4 will be published in Jansen et al. (in prep.). Contributions from the other publications listed here will be cited in the text at the appropriate position.

In preparation and submitted

Jansen, N., Hartmann, J., Lauerwald, R. and Kempe, S., in prep. Bicarbonate fluxes and CO_2 consumption related to chemical weathering on the North American Continent.

Hartmann, J., Dürr, H.H., **Jansen, N.** and Meybeck, M., submitted. Differences between the geochemical composition of the continental crust and the terrestrial surface. Submitted to Journal of Geochemical Exploration.

Published

Abu Ghazleh, S., Hartmann, J., **Jansen, N.** and Kempe, S., 2009. Water input requirements of the rapidly shrinking Dead Sea. Naturwissenschaften 96 (5), 637-643.

Hartmann, J., **Jansen, N.**, Dürr, H.H., Harashima, A., Okubo, K. and Kempe, S., 2010. Predicting riverine dissolved silica fluxes into coastal zones from a hyperactive region and analysis of their first order controls. International Journal of Earth Sciences 99 (1), 207-230.

Hartmann, J., **Jansen, N.**, Dürr, H.H., Kempe, S. and Köhler, P., 2009. Global CO_2-consumption by chemical weathering: what is the contribution of highly active weathering regions? Global and Planetary Change 69 (4), 185-194.

Jansen, N., Hartmann, J., Lauerwald, R., Dürr, H.H., Kempe, S., Loos, S. and Middelkoop, H., 2010. Dissolved Silica mobilization in the conterminous USA. Chemical Geology 270 (1-4), 90-109.

Hartmann, J., **Jansen, N.**, Kempe, S. and Dürr, H.H., 2007. Geochemistry of the river Rhine and the upper Danube: Recent trends and lithological influence on baselines. Journal of Environmental Science for Sustainable Society 1, 39-46.

1 General Introduction

1.1 Global cycles and weathering

The earth can be seen as ensemble of the compartments atmosphere, hydrosphere, biosphere and lithosphere. Analyzing and understanding matter fluxes between the different compartments and their interactions is crucial to understanding the evolution of our home planet and object of the research on global biogeochemical cycles.

One of the major elementary cycles on earth is that of carbon. Carbon is a key element of life. The global carbon cycle is subject to physical, chemical, biological, and geological processes that proceed on timescales from less than days to millions of years (cf. Bolin et al., 1979). Carbon in the atmosphere, e.g. atmospheric CO_2, is considered to be a major impact factor on global climate (cf. IPCC, 2007). On geological timescales, chemical weathering of silicate rocks is one of the major controls on atmospheric CO_2 concentration (pCO_2) (Kempe, 1979; Zeebe and Caldeira, 2008; Pagani et al., 2009). Thus, the transformation of silicate minerals into carbonate minerals is a major control of long-term climate changes in earth history (cf. Holland, 1978; Walker et al., 1981; Berner et al., 1983; Kempe and Degens, 1985; Ludwig et al., 1998; Hartmann et al., 2009).

Chemical weathering of silicate minerals also marks the start of the bioavailable part of the silicon cycle (e.g.Derry et al., 2005). Dissolved silica (DSi) is a major nutrient for many aquatic systems and certain terrestrial plants (e.g. Epstein, 1999; Ragueneau et al., 2009). Following its mobilization by chemical weathering, DSi passes through terrestrial and continental aquatic cycles in which it may be retained before being transported to the oceans in rivers (cf. Conley et al., 1993; Alexandre et al., 1997; Conley, 2002; Humborg et al., 2006). Output from rivers is a major source of DSi in coastal waters (DeMaster, 1981; Beusen et al., 2009; e.g. Ragueneau et al., 2009) and a major control of algal species composition (Officer and Ryther, 1980). DSi availability can also affect the oceanic carbon pump (Sieracki et al., 1993).

The two cycles of carbon and silicon are intimately linked by rock weathering. This study focuses on modeling DSi mobilization and atmospheric CO_2 consumption by chemical rock weathering.

1.2 Models of elementary fluxes resulting from chemical weathering

Chemical weathering has been in scientific discussion since the 19th and early 20th century (e.g. Roth, 1893; Clarke, 1924). Its role in global biogeochemical cycles came into focus of a broader community of researchers since the works of Livingstone (1963) and Garrels and Mackenzie (1967). Livingstone (1963) assembled existing data for worldwide rivers to global average elementary concentrations.

Garrels and Mackenzie (1967) assumed elementary signatures of individual weathering reactions and retraced their contributions to spring waters in the Sierra Nevada.

The latter approach is the foundation for one of the two established methods to model weathering induced fluxes of dissolved HCO_3^- and the resulting atmospheric CO_2 consumption by weathering. The "reverse approach" quantifies contributions of different sources for HCO_3^- in rivers by attributing elementary signatures ("end members") to them (e.g.Meybeck, 1987; Gaillardet et al., 1999; Roy et al., 1999; Velbel and Price, 2007). The prediction quality of model using the reverse approach depends largely on the choice of end members. End members can represent inputs from, e.g., the atmosphere, weathering reactions of certain minerals, or agriculture. However, extrapolation of models using the reverse approach is difficult as their source data and the assumed end member elemental ratios describe only their calibration area.

The second method ("forward approach") was inspired by the temperate stream model of Meybeck (cf. Meybeck, 1987). This model used data from French catchments to rank different chemical erosion rates for 10 lithological classes (Meybeck, 1987). Models using the forward approach apply statistical methods on large numbers of calibrating catchments to derive functions for weathering induced fluxes of HCO_3^- (Bluth and Kump, 1994), CO_2 (Amiotte-Suchet and Probst, 1995; Hartmann, 2009) or DSi (Bluth and Kump, 1994; Beusen et al., 2009). Those functions, relating catchment attributes to elementary fluxes, mostly include lithology and runoff. For basalt, a model using runoff and temperature was published by Desert et al. (2003). The quality of model predictions using the forward approach largely depends on quality and quantity of catchments for model calibration and on quality of available spatial data to define catchment attributes. Extrapolation of models using the forward approach is possible to the extent of applied spatial data, considering representativeness of the calibration area.

For modeling the ratio of CO_2 consumption (here used as: the transformation of atmospheric/soil CO_2 into dissolved HCO_3^- counterbalanced by cations released from chemical weathering) on weathering induced HCO_3^- flux it is necessary to distinguish carbonates and silicates as weathering source rocks (cf. Amiotte-Suchet et al., 2003). While silicate mineral weathering induced HCO_3^- flux originates entirely from atmospheric/soil CO_2, carbonate mineral weathering induced HCO_3^- flux stems to at least 50 % from the carbonate minerals. Amiotte-Suchet et al. (2003) relied on lithological classes to differentiate between carbonate and silicate contributions. However, field studies suggest significant contributions of carbonates in weathering outputs from predominantly silicate rocks (e.g. granite: Mast et al., 1990). Hartmann (2009) introduced a methodology to correct those contributions by using elemental ratios of calcium and sodium.

1.3 Identified research gaps

Existing global forward models for HCO_3^- fluxes (Gibbs and Kump, 1994) and CO_2 consumption (Amiotte-Suchet and Probst, 1995; Hartmann et al., 2009) by chemical weathering were calibrated on regional datasets and extrapolated to the global scale. However, it has not been satisfactorily tested that those models appropriately predict matter fluxes in areas they were not calibrated on. Moreover, the coarse applied lithological maps may not sufficiently represent the small, intensively weathering areas, which were shown to contribute significantly to CO_2 consumption by chemical weathering (Hartmann et al., 2009).

Processes governing chemical weathering, e.g. mineral dissolution kinetics, hydrological flow processes or plant influences, are well understood on the laboratory or local scale. However, these processes may not be represented sufficiently in existing global models of CO_2 consumption by chemical weathering, as those used only lithology and runoff as predictor variables (Amiotte-Suchet and Probst, 1995; Hartmann et al., 2009). Improved resolution of spatial data and an extended catchment database for calibration could increase the representativeness of models and allow incorporating additional predictors to increase the accuracy of representation of processes governing chemical weathering. Moreover, the multilithological modeling approach, and the distinction of carbonate HCO_3^- using elemental Ca/Na ratios (Hartmann, 2009) was calibrated in Japan, a steep, highly active weathering region. In the calibrating dataset, anthropogenic impacts could be neglected (Hartmann, 2009). To increase stability of the model approach for global application, it should be tested on a different setting and correction for anthropogenic impacts should be considered.

Furthermore, general circulation models (GCM) could profit from incorporating a spatially explicit global weathering model as weathering module. This allows identifying regions that are most relevant for the climate-weathering feedback, and evaluate the feedback strength (Hartmann, 2008). However, implementing spatially explicit weathering models into GCM requires upscaling the spatially explicit models to the grid resolution of the GCM, which is typically 2 to 3.75°. Upscaling effects also have been neglected in most existing global spatially explicit models (Bluth and Kump, 1994; Amiotte-Suchet and Probst, 1995).

1.4 Contributions of this thesis

The presented thesis aims to contribute to development of a global spatial explicit model of fluvial dissolved elementary fluxes. Existing modeling approaches are improved and applied to a large hydrochemical database. A number of works have led to the techniques and methods employed in the presented thesis. The author contributed to the works of Hartmann et al. (2007; 2009; 2010; submitted) and Abu Ghazleh et al. (2009; compare also Appendix E).

Work on geochemical baselines in the basins of Rhine and upper Danube demonstrated the great importance of small areas of easily weatherable lithology classes (Hartmann et al., 2007). While a study on DSi mobilization in Japan demonstrated the applicability of a multilithological model approach and highlighted the importance of data quality and resolution for model development (Hartmann et al., 2010). For that study area, the development of a new lithological map with increased resolution compared to the most advanced existing map (Dürr et al., 2005) proved beneficial for model calibration (Hartmann et al., 2010). Furthermore, that study highlighted the advantages of higher resolution of digital elevation models, which were further assessed on the slopes of the Dead Sea (Abu Ghazleh et al., 2009).

Extrapolating the results of a forward model for CO_2 consumption by chemical weathering calibrated on Japanese catchments (Hartmann, 2009) resulted in a global CO_2 consumption by chemical weathering of 237 10^6 t C a^{-1} (Hartmann et al., 2009). The result is close to existing numbers; however, the extrapolation showed for the first time that only 9 % of the global land surface area contributed 50 % of that amount. This highlights the importance to resolve and identify small, highly active weathering areas, specifically for studies considering global change. During research for that study, a literature review resulted in new insights on the geochemical composition of continental surfaces (Hartmann et al., submitted). Application of the literature data resulted in significant differences between terrestrial surface and upper continental crust that highlight the important role of earth surface processes for the geochemical fractionation of the continental crust. It was concluded that using average elemental compositions of the upper continental crust is not sufficient for modelling earth surface elementary fluxes.

Building on the knowledge gained in these studies, in the presented thesis forward models are developed for DSi mobilization and CO_2 consumption by chemical weathering in North America to test

1) whether the predictors used in existing models can be applied to the data of North America and if implementation of new predictors improves model results,
2) whether the existing models represent the predicted fluxes for North America appropriately,
3) what the contribution of high yielding areas to total fluxes in North America is and where these areas are situated.

For that, new models for DSi mobilization and CO_2 consumption by chemical weathering are calibrated in North America. To calibrate the models, emphasis was given to hydrochemical data quality and high resolution of applied spatial data. A new lithological map of North America was

4

assembled (Jansen et al., 2010) exceeding the spatial resolution of the most advanced existing homogenous lithological map covering North America (Dürr et al., 2005) by a factor higher than 150 (Chapter 2).

The high quality of hydrochemical data and resolution of spatial data allowed for qualitative assessment of potential impact of the factors land cover and temperature on DSi mobilization by chemical weathering (Chapter 3). In addition, a comparison of the developed DSi mobilization model with existing DSi mobilization models that were calibrated in other regions allows assessing their representativeness for North America.

The developed models for HCO_3^- fluxes resulting from chemical weathering and associated CO_2 consumption allow for a quantitative assessment of modeled land cover influence (Chapter 4). Further emphasis is given to the error in correction of HCO_3^- fluxes for contributions of carbonate weathering. Extrapolation of the models also highlights the contributions of highly active weathering regions to CO_2 consumption by chemical weathering and their positions in North America.

2 Lithological map of North America

2.1 Introduction to lithological classification

Lithological maps describe the chemical and physical properties of rocks. They are important tools for modeling global geochemical cycles, because lithology is an important control of elementary fluxes induced by chemical weathering (Amiotte-Suchet and Probst, 1993; Bluth and Kump, 1994; Horton et al., 1999; Beusen et al., 2009; Hartmann, 2009). Lithological maps were already used for quantification of water chemistry by Gibbs (1967). Existing lithological maps covering the North American continent were presented by Bluth and Kump (1991), Amiotte-Suchet et al. (2003), and Dürr et al. (2005); each of them is a global lithological map. The first two maps are raster datasets with spatial resolutions of 2° and 1°, respectively. The map of Dürr et al. (2005) is a vector-based map with a resolution of 1:25mio. Lithological maps, like other thematic maps for discrete data, use a classification scheme to describe rock lithology. Classification is a constant compromise between exactness and simplicity. The existing maps use 13, 6 and 15 classes in the area of North America, respectively (Excluding water and ice). Considering the importance of lithology as predictor for chemical weathering rates, a new, more detailed lithological map of North America is developed and presented herein.

2.2 Map sources

The presented lithologic map uses geographical features from existing regional North American geological maps. Translation of geological information into lithological units is done using descriptions from these maps or additional literature describing the geologic units. The source data of the lithological map are shown in figure 1 and listed in table 1.

2.3 Methods of translation

2.3.1 Step one: Translating geological information into lithological information

Most of the lithological units by Dürr et al. (2005) were used, but the classes *complex lithology* (CL) and *precambrian rocks* (PR) were omitted and some classes were added to increase detail (Table 2). The two digit classification scheme ("XX") applied by Dürr et al. (2005) was expanded by two dimensions to "XXYYZZ". The three levels are in the following called XX, YY and ZZ (Table 2). Level XX classifies the lithology; level YY gives additional information (e.g. grain size of sediments); and level ZZ adds special information (e.g. coal occurrences). The classes were chosen to increase representation of attributes that are potentially relevant for chemical weathering studies.

According to this classification, a coal bearing sandstone would be labeled "SSSSCL", a slightly metamorphosed basalt would be labeled "VB__MT", etcetera. The complete set of lithological classes is listed in table 2. Classification causes problems when competing attributes could be given to the same unit. This may happen at any level and was treated with care. Emphasizing the general idea to give priority to the more weathering affine units, the following rules were adhered to prioritize in case of classification conflicts:

- As soon as carbonates are mentioned in the source data, even as cement, they will be mentioned in the map: XX is classified SM or SC.
- If evaporites are mentioned in the source data, either XX or ZZ are classified EV.
- On level ZZ, priority is given to anoxic indicators (CL, BS).
- On all levels, emphasis is given to lithological classes that have larger assumed impact on chemical weathering rates.
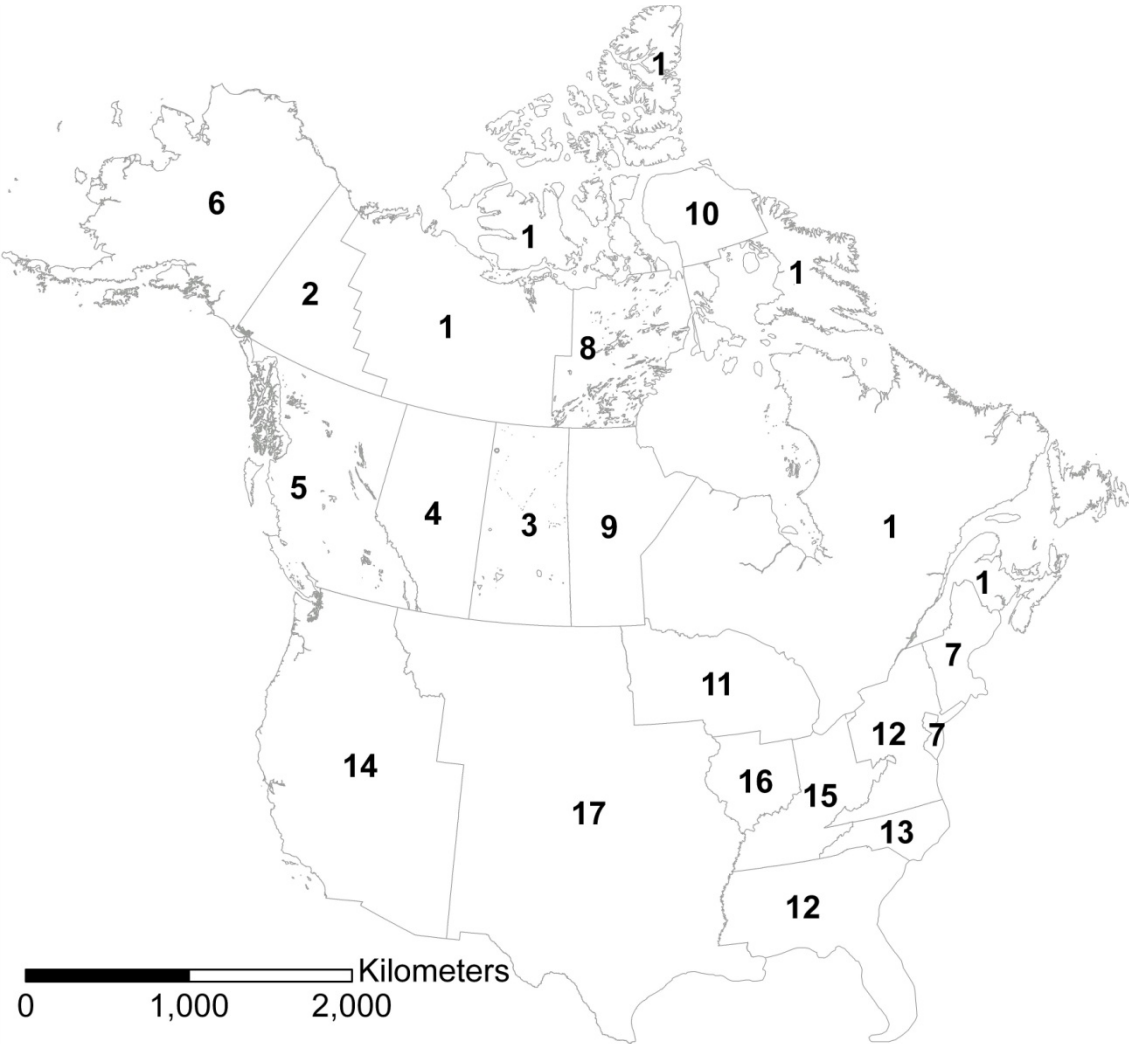
Figure 1: Map of regional sources of the lithological map of North America, the area codes given here are described in table 1.

Table 1: References for the lithological map of North America (Regional positions of the area codes are given in figure 1)

Area code	Geological shape reference	Lithological information reference
1	(Wheeler et al., 1997)	(Douglas et al., 1970)
		(Wheeler et al., 1997)
2	(Gordey and Makepeace, 2000)	(Gordey and Makepeace, 2000)
3	(Macdonald and Slimmon, 1999)	(Macdonald and Slimmon, 1999)
4	(Hamilton et al., 2004)	(Buschkuehle, 2003)
		(Douglas et al., 1970)
		(Douglas et al., 1974)
		(Frazier and Schwimmer, 1987)
		(Macdonald and Slimmon, 1999)
		(Hamblin, 1997)
		(Hamilton et al., 2004)
		(Hayes et al., 1994)
		(Irish, 1971)
		(Massey et al., 2005)
		(McMechan and Dawson, 1995)
		(Okulitch, 2006)
		(Ollerenshaw, 1970)
		(Pollock et al., 2000)
		(Powers, 1931)
		(Pruett and Murray, 1991)
		(Richardson et al., 1990)
		(Yeo et al., 2002)
5	(Massey et al., 2005)	(Massey et al., 2005)
6	(Moll et al., 1997)	(Beikman, 1980)
7	(Dicken et al., 2005b)	(Dicken et al., 2005b)
	(Nicholson et al., 2006)	(Nicholson et al., 2006)
8	(Geological Survey of Canada, 2008)	(Aspler and Chiarenzelli, 1997)
		(Ernst and Buchan, 2004)
		(Hadlari and Rainbird, 2000)
		(Hadlari et al., 2006)
		(Schau, 1993)
		(Tella et al., 2007)
9	(Schledewitz and Lindal, 2005)	(Schledewitz and Lindal, 2005)
10	(Geological Survey of Canada, 2008)	(Blackadar et al., 1968)
		(Johns and Young, 2006)
		(Geological Survey of Canada, 2008)
11	(Cannon et al., 1999)	(Cannon et al., 1999)
12	(Dicken et al., 2005a)	(Dicken et al., 2005a)
13	(Dicken et al., 2007)	(Dicken et al., 2007)
14	(Ludington et al., 2005)	(Ludington et al., 2005)
15	(Nicholson et al., 2005)	(Nicholson et al., 2005)
16	(Nicholson et al., 2007)	(Nicholson et al., 2007)
17	(Stoeser et al., 2005)	(Stoeser et al., 2005)

Table 2: Short codes and long names for the lithological classes applied in the presented lithological map

XX	First level lithological information
AD	Alluvial deposits
DS	Dune sands
EV	Evaporites
LO	Loess
SU	Unconsolidated sediments
SC	Carbonate sedimentary rocks
SM	Mixed sedimentary rocks
SS	Siliciclastic sedimentary rocks
MT	Metamorphic rocks
PA	Acid plutonic rocks
PI	Intermediate plutonic rocks
PB	Basic plutonic rocks
VA	Acid volcanic rocks
VI	Intermediate volcanic rocks
VB	Basic volcanic rocks
PY	Pyroclastics
WB	Water bodies
IG	Ice and glaciers
UN	Lithology unknown

YY	Second level lithological information
SS	Sandstone or coarser dominates clastic fraction
SH	Shale or siltstone dominates clastic fraction
MX	No grain size domination distinguishable
PU	Pure limestone; limestone occurrence in non-sedimentary units
PY	pyroclastics mentioned
AM	amphibolite mentioned
XE	xenoliths mentioned
GR	greenstone mentioned

| ZZ	Third level lithological information
MT	metamorphosis mentioned, but parent rock still named
VR	volcanic rock mentioned in non-volcanic units
PR	plutonic rock mentioned in non-plutonic units
SR	sedimentary rocks in non-sedimentary units
SU	unconsolidated sediments mentioned in non-sedimentary units
BS	black shale, oil shale or similar mentioned
CL	Lignite, peat or coal occurrences mentioned
GL	glacial drift mentioned (including till)
EV	evaporites mentioned
CH	chert mentioned
WE	weathering explicitly mentioned

The geological maps listed in table 1 were translated into lithological maps according to those rules. Lithologic interpretation given by the source data was not re-interpreted in the process. This led to jumps in lithology at map intersections (Figure 2), but could not be avoided because for eliminating these, a much deeper research would have been necessary. It was decided to trust the specialists who authored the geological maps in their judgment.

2.3.2 Step Two: Assembling one lithological map from the regional source maps

Following the translation of the lithological maps, the individual maps were assembled into one single map. However, first, some corrections were done for the geographical features of the maps which are described below.

For some units, regional geological maps in Canada show unknown lithologies; these polygons are replaced with those from a coarser scale geological map (Wheeler et al., 1997) which gives lithological information.
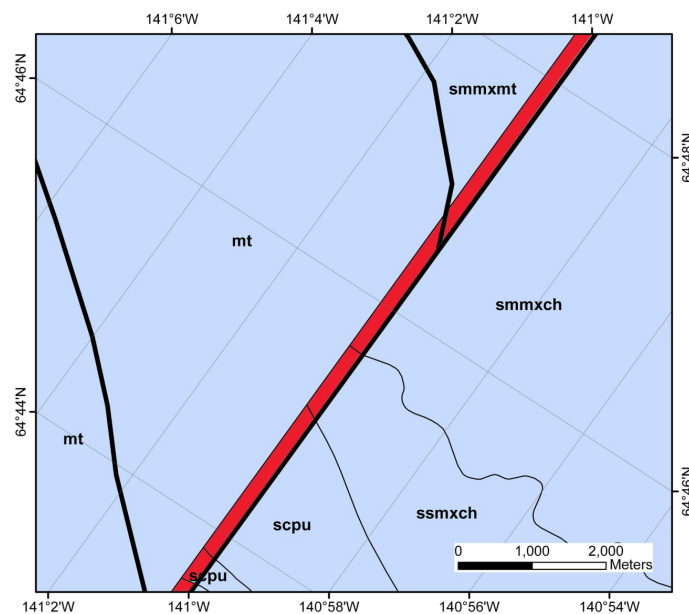
Figure 2: An example for overlapping maps. The bold black lines at the western side of the map represent the original polygons from the geological map of Alaska (Moll et al., 1997). The curved thin black lines are the geological polygons of the geological map of Yukon (Gordey and Makepeace, 2000). The red area overlapped and was merged to the Yukon map and adopted its lithological attributes. Labels name the lithological units, it is observable that units of both maps do not exactly fit together. Please mind the scale.

At map intersections, a large number of features overlap on small areas due to overlaps in the source maps. The overlapping parts have been merged to one of the two conflicting maps, thus adopting all lithological attributes from it. At the border of Canada and Alaska, the features are merged to the geological map of Yukon (Gordey and Makepeace, 2000), which has a higher spatial resolution than the Alaskan map (Moll et al., 1997). Figure 2 gives an example for merged areas between Alaska and

10

Yukon. On inner-Canadian borders, the features were merged to the feature with the smaller feature number, which is basically a random merge to one of the neighboring features. There was no individual check for each polygon, because they are small (most <100m in diameter) but many (>1000). Within the border of the Saskatchewan map (Macdonald and Slimmon, 1999) are some polygons that overlap each other. The overlapping parts were merged to the smaller neighbor, highlighting smaller polygons.

In the geological maps from the conterminous USA, about 40 000 overlapping features were found, each overlap less than 100 m wide. The overlapping areas were converted into new polygons. Those polygons were merged automatically to the neighboring polygon with the longest shared border using functionality of the ArcGIS "eliminate"-tool. Apart from overlapping areas, gaps between different geological maps existed, which were filled with new polygons. 83000 new polygons were created of which only two were larger than 1 km²; the third largest was barely 63m wide with an area of 0.5 km². Those polygons were treated the same way as overlapping areas and merged to the neighbor polygon sharing the longest border. Between Canada and the maps from the conterminous USA, 5342 areas were found to overlap; they were merged to the U.S. maps for consistency.

The different geological maps, now sharing consistent borders, were eventually combined into one lithological map of North America, which is described below.

2.4   Result: The lithological Map of North America

The new lithological map of North America (Figure 3) consists of 262 111 polygons with an average size of 75 km². The 19 used level XX classifications are in detail described below.

2.4.1   Lithological classes

2.4.1.1   Alluvial deposits (AD):

This class is comprised of young fluvial sediments associated with rivers. It was only applied if the geological map stated alluvium, alluvial fans or alluvial terraces. Regionally only two large areas of AD are mapped east of the Mississippi and at the lower reaches of the Delaware River. There is a classification overlay between AD and SU (*unconsolidated sediments*) in the source data as large areas are classified SU following the geological map information that could instead be named AD.

2.4.1.2   Dune sands (DS):

Dune sands are aeolian deposits composed of well sorted, mostly fine grained sands. Their prime occurrence is in dry areas in the south west of the conterminous USA.

2.4.1.3   Loess (LO):

Loess deposits are aeolian sediments consisting mostly of silt and carbonate grains. The classification was only applied if the source data gave loess as geological unit. LO is the rarest occurring lithological class consisting of only 370 polygons covering 0.16 % of North America. This is probably an underestimation attributed to thin loess sediments which are not shown on geological maps (Bettis et al., 2003) and the indistinct transition to SU. It is expected that some loess is contained in the large areas covered by SU. Regionally most LO is mapped in the far northwestern region of the conterminous USA.

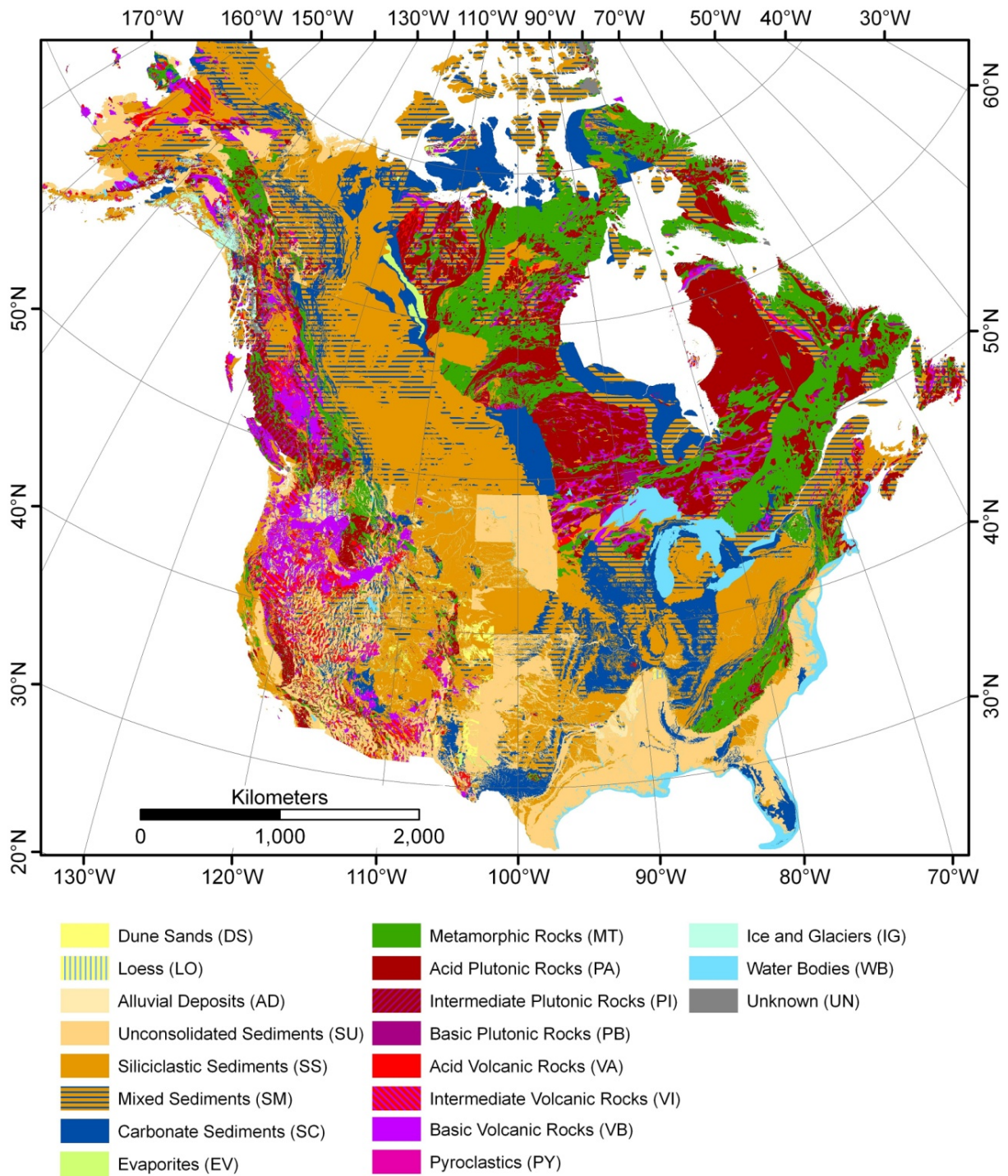### 2.4.1.4   Unconsolidated sediments (SU):

Unconsolidated sediments are widely distributed, especially in the U.S. They are dominant in the southeast, from the Atlantic coast to the Gulf of Mexico. SU represents different kinds of sediments that are not yet consolidated. Most are young, while not necessarily in their first weathering cycle. Transitions to the previously described classes AD, DS and LO as well as to *consolidated sedimentary rocks* (SS) are not well defined in the source data. This is observable in North Dakota (figure 3), where almost the entire state was classified as SU, while the surrounding states are dominated by consolidated sediments (classified as SS). This obvious inconsistency was kept unchanged because classifications from the geological source maps were not reinterpreted (just translated) for lithological classification.
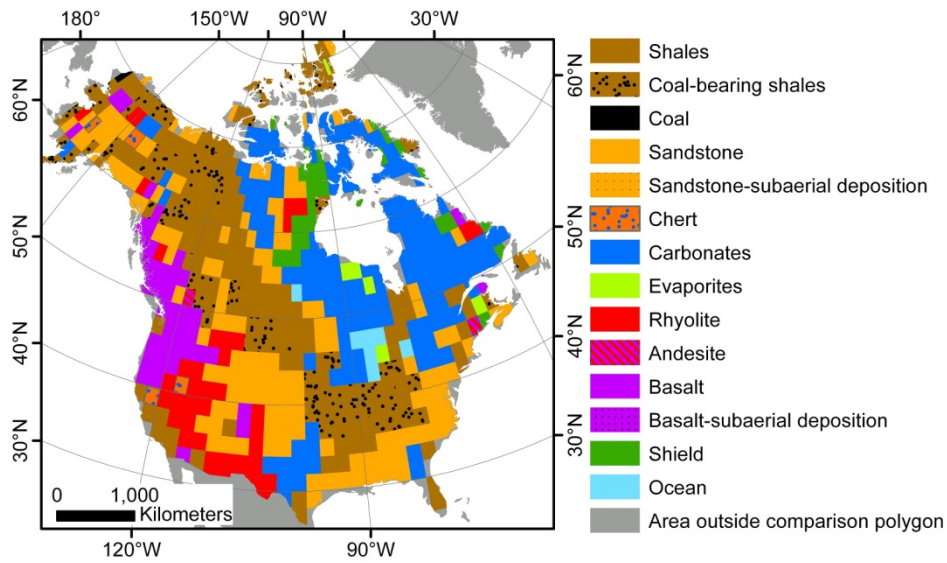
2.4.1.5   Evaporites (EV):

Evaporites contain mostly chlorides or sulfates. This class can contribute significantly to river chemistry (e.g. Hartmann et al., 2007) due to its high weathering rates (Meybeck, 1987). Additionally, it is the only lithological class expected to significantly release chloride during weathering. It was mapped in small areas in and around Texas and Oklahoma as well as some large occurrences in the Northwest Territories. EV is rare and occupies a proportion of 0.26 % of the entire map.

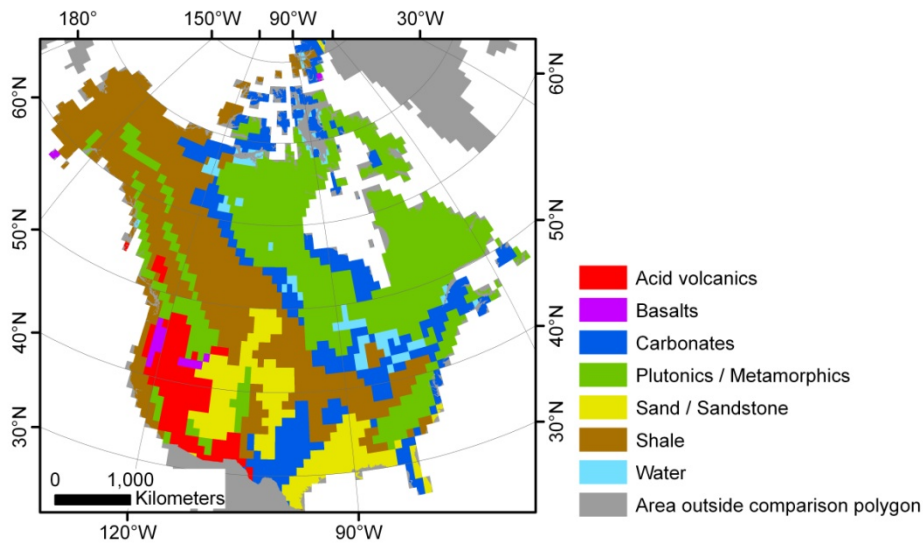### 2.4.1.6   Carbonate sedimentary rocks (SC):

Covering 11.05 % of the aerial proportion of North America, SC is important for dissolved material fluxes. Carbonates, both limestone and dolomite were grouped in this class, as well as rock units dominated by carbonates. Also marble was grouped in this class on account of its chemical composition.

Figure 3: The new lithological map of North America

Legend:
- Dune Sands (DS)
- Loess (LO)
- Alluvial Deposits (AD)
- Unconsolidated Sediments (SU)
- Siliciclastic Sediments (SS)
- Mixed Sediments (SM)
- Carbonate Sediments (SC)
- Evaporites (EV)
- Metamorphic Rocks (MT)
- Acid Plutonic Rocks (PA)
- Intermediate Plutonic Rocks (PI)
- Basic Plutonic Rocks (PB)
- Acid Volcanic Rocks (VA)
- Intermediate Volcanic Rocks (VI)
- Basic Volcanic Rocks (VB)
- Pyroclastics (PY)
- Ice and Glaciers (IG)
- Water Bodies (WB)
- Unknown (UN)

Figure 4: Comparison of the existing lithological maps covering North America from A) Bluth and Kump (1991), B) Amiotte-Suchet et al. (2003) and C) Dürr et al. (2005)

2.4.1.7 Mixed sedimentary rocks (SM):

Sedimentary rocks of this class show some occurrence of carbonates while the dominant rock type is of siliciclastic nature. They are the second most abundant class (13.94 % of the map) and are often associated with SC. As soon as carbonates were mentioned in the geology source data (if not evaporites were also prominently mentioned), even as cement, rock units were classified SM; if carbonates dominated, the class SC was used.

2.4.1.8 Siliciclastic sedimentary rocks (SS):

This sedimentary class is the most abundant in North America; it covers 23.42 % of the map area. Apart from its wide general distribution, a large band of SS draws from the northern Northwest Territories to the central U.S. Among rocks classified as SS are conglomerate, sandstone, siltstone, mudstone and shale (because of only slight metamorphic alterations). Knowing that SS will still contain some carbonates, carbonate impact was minimized as far as possible (no carbonate rocks were named in source data of SS-classified units). Quartzites were also classified as SS because of their close resemblance to sandstone.

2.4.1.9 Metamorphic rocks (MT):

This is one of the large lithological classes in terms of abundance (12.68 % of the map, average size of individual polygons: 167 km²) and certainly the one with the largest geochemical variability. MT rock types range from schist over gneiss, amphibolite and pyroxenite to serpentinite; they also still contain occurrences of marble and quartzite. The weatherability for these rocks varies largely (Meybeck, 1987). Most MT occurs in eastern Canada, but also some in the Appalachians and northern Rocky Mountains.

2.4.1.10 Acid plutonic rocks (PA):

This class consists mainly of granite and granitoids. The border to PI has been drawn by the quartz content: plutonic rocks containing quartz were grouped in PA. Accordingly, a granodiorite or a quartz diorite would still belong to PA. *Acid plutonic rocks* are by far the most abundant plutonic rocks. They cover 12.32 % of North America and form large polygons with an average size of 162 km². PA occurs predominantly in eastern Canada, but is also scattered in the mountainous regions of the Atlantic and Pacific coasts.

2.4.1.11 Intermediate plutonic rocks (PI):

PI is chemically situated between basic and acid plutonic rocks but also includes units with undetermined exact plutonic rock type. It was introduced to further sharpen the view on chemical composition of plutonic rocks and its influence on weathering rates. PI consists mainly of diorite-type

15

rocks. As soon as gabbroid rocks occurred as major unit, the class PB was chosen. Regionally, most PI appears in the Northern Rocky mountains.

2.4.1.12 Basic plutonic rocks (PB):

This class is the least abundant plutonic rock class. It covers 0.56 % of North America and shows only very small polygons with an average size of 23.4 km^2. Gabbroid rocks as well as ultramafic rocks were grouped in this class. The main occurrence of PB is situated north of Lake Superior, but PB also occurs in small patches close to other plutonic rocks.

2.4.1.13 Acid volcanic rocks (VA):

This is the smallest volcanic lithological class by area and average polygon size. It covers 0.99 % of North America and was mapped as 8 651 polygons with an average area of 22.8 km^2. It consists mainly of rhyolite, trachyte and similar rock types. VA appears widespread in Nevada, but there is also one large occurrence west of Lake Superior.

2.4.1.14 Intermediate volcanic rocks (VI):

Analogue to the plutonic lithological classes, VI is chemically situated between VA and VB. It is composed mainly of dacite and andesite but also chosen if no exact volcanic rock type was identified. With 48 km^2, the average polygon area is significantly larger than that of VA while the total count is similar. This could be an indication of less viscosity of intermediate lava compared to acid lava, resulting in longer flows and larger areas. Most VI occurrences are situated west of the Rocky Mountains close to the Pacific coast.

2.4.1.15 Basic volcanic rocks (VB):

VB, the most abundant volcanic lithological class, covers 3.96 % of North America. It is almost completely composed of basalt and its subtypes. Large occurrences are mapped in the vicinity of the Rocky Mountains and west to northeast of Lake Superior.

2.4.1.16 Pyroclastics (PY):

Pyroclastics combine large contact surface with unstable minerals or even volcanic glass to exhibit a very high vulnerability to weathering. The class was introduced in the Japan lithological map in order to emphasize this characteristic (Hartmann et al., 2010). It only covers a small area of 0.26 % of North America. The average polygon sizes are the smallest of all lithological classes, being only 21.3 km². *Pyroclastics* consists predominantly of tuffs, but also contain volcanic breccias. It can be either consolidated or unconsolidated. PY was mapped throughout the western region of North America.

2.4.2 Lithological classes representing non-lithological units

2.4.2.1 Water bodies (WB):

This class combines occurrences of mapped water in the source data. However, the presented map is focused on lithology, not on water; it does not try to offer a complete water body dataset and should not be used as such. About 8800 water bodies were mapped in the geological maps whose average area is close to 55 km^2, which is but a tiny fraction of the number of water bodies existing in North America. Also a large part of WB is actually the Atlantic Ocean, which is mapped as WB close to the coastline, or the Great Lakes. In most of the Canadian area, no WB is mapped at all.

2.4.2.2 Ice and glaciers (IG):

Similar to WB, this class was just taken from the geological maps. No work was done to improve the quality of the glacial dataset. It is not recommended to use the IG extend for glacial studies. Furthermore, it is expected that some of the *unknown* (UN) lithologies (compare 2.4.2.3) are situated under glacial coverage and could instead be attributed to this class. Most IG is mapped in the far north of the Rocky Mountains at the border between Canada and Alaska.

2.4.2.3 Unknown (UN):

For some regions (0.62 %) the available geological maps of North America contain blind spots. These were labeled unknown, here. Most UN occurs close to some IG lithological classes in the northern Rocky Mountains and in the far north Northern Territories.

2.5 Comparison to previous lithological maps

The comparison with existing lithological maps covering the North American continent reveals large differences between those maps and the new map (Figure 4 A-C). The intersection of the map from Bluth and Kump (1991) with the North American continent (ESRI, 2008) includes 151 polygons with an average size of 121 000 km² (Figure 4 A). The same part of the map developed by Amiotte-Suchet et al. (2003) includes 137 different lithology polygons with an average area of 136 500 km² (Figure 4 B). Resolution increased significantly with the map of Dürr et al. (2005) whose map's North American part consists of 1472 polygons with an average area of 12 857 km² (Figure 4 C). Comparisons between the classes of the new lithological map of North America and those of existing maps are given in table 4 (comparing the new map with Bluth and Kump, 1991), table 5 (comparing with Amiotte-Suchet et al., 2003) and table 6 (comparing with Dürr et al., 2005). Note that a subscript "D" (XX$_D$) will be added to the lithological classes by Dürr et al. (2005), to reduce confusion with the classes used in the presented map (in short: "new map").

Carbonate-rich lithological classes uniformly dominate about 25 % of the North American continent, as Bluth and Kump (1991), Dürr et al. (2005) and the new map agree (Table 3). The latter two differentiate carbonate-rich lithological classes into carbonate sedimentary rocks (SC) and mixed carbonate-non carbonate sedimentary rocks (SM). The map of Amiotte-Suchet et al. (2003) shows barely 15 % carbonate. Those carbonates are contained to 56 % by carbonate-rich sedimentary classes of the new map (SC + SM); another 30 % are located within non carbonate-sedimentary classes. Carbonates in the map of Bluth and Kump (1991) are only to small proportions represented by SC and SM in the new map (12 % and 14 % respectively). 55 % of them are classified MT or PA in the new map. The sums of carbonate-rich sediments (SC and SM) in the map of Dürr et al. (2005) and the new map are virtually the same. However, SM_D is in the new map mostly split between SC (23 %) and SS (41 %) and is only contained to 15 % by SM.

Non-carbonate sediments amount to 41 %, 33 % and 37 % in the maps of Amiotte-Suchet et al. (2003), Dürr et al. (2005) and the new map, respectively. In the map of Bluth and Kump (1991), siliciclastic sediments are distributed over 57 % of the North American continent. The map of Dürr et al. (2005) and the new map differentiate between consolidated and unconsolidated sediments and differ from each other in detail. In the here presented map, most siliciclastic sediments are grouped in SU and SS, while the map of Dürr et al. (2005) gives higher values for AD and LO, for whose description Dürr et al. (2005) consult additional literature. Moreover, Dürr et al. (2005) use the lithological class *Complex lithology* (CL), which is composed mostly of sedimentary rocks (cf. Hartmann et al., 2009) and is omitted in the new map because of increased spatial resolution and more descriptive levels, which unfold the *complex lithology*. *Sandstone* and *shale* of Bluth and Kump (1991) are also mostly mapped as *siliciclastic sedimentary rocks* in the new map. However, 16 % of the *sandstone* and 26 % of the *shale* are situated within carbonate sedimentary lithological classes (SC and SM) of the new map. s*and/sandstone* and *shale* of Amiotte-Suchet et al. (2003) are situated also mostly within siliciclastic sedimentary units of the new map, but still a significant proportion is represented by carbonate-rich classes (SC + SM; 9 % for s*and/sandstone* and 27 % for s*hale*). The sedimentary classes of the map of Dürr et al. (2005) match those of the new map generally well. However, for the classes SS_D and SU_D of Dürr et al. (2005), some carbonate-rich sedimentary lithological classes are mapped in the new map (SC, SM 22 % and 10 % respectively). The class AD_D, which is far less represented in the new map, was replaced mostly (67 %) by SU; the class LO_D from Dürr et al. (2005) is represented by SS, SC, SU and SM (35 %, 28 %m 20 % and 13 % respectively) in the new map. The lithological class CL_D from Dürr et al. (2005) was broken down into 19 % SM, 16 % SS, 15 % PA, 13 % MT and 10 % VB in the new map.

Plutonic and metamorphic rocks amount to about 30 % of the area of North America in the maps of Amiotte-Suchet et al. (2003), Dürr et al. (2005) and the new map. While they are combined as one lithological class in the map of Amiotte-Suchet et al. (2003), Dürr et al. (2005) differentiate between metamorphic, precambrian as well as acid and basic plutonic rocks. Although summing up to about the same area, the details again differ between the new map and the one of Dürr et al. (2005). However, this could be due to a slightly different attribution, as intermediate plutonic rocks are now distinguished while they were combined in Dürr et al. (2005). Moreover, constraints between plutonic and metamorphic rocks are not easy to isolate. Consequently, Bluth and Kump (1991) concentrate this group of lithological classes into one class (*shield rocks*), which however barely amounts to 3 % of the area of North America in their map. The *shield rocks* classified by Bluth and Kump (1991) are composed largely of MT (49 %) and PA (28 %) in the new map but also contain 10 % SM. *Plutonics/metamorphics* from Amiotte-Suchet et al. (2003) are equally distributed by one third MT and one third PA. The rest is mostly sediments, including 9 % SM, and 4 % VB. The lithological classes MT_D and PA_D of Dürr et al. (2005) are also dominated by those two lithological classes in the new map, too (81 % and 61 % respectively). Nevertheless, they additionally contain significant amounts of SM (8 % and 6 % respectively).

Volcanic rocks amount to about 7 % of the North American surface area in the maps of Amiotte-Suchet et al. (2003), Dürr et al. (2005) and the new map. While Amiotte-Suchet et al. (2003) attribute most of the volcanic rocks as *acid volcanic rocks*, Dürr et al. (2005) attribute all as *basic and intermediate volcanic rocks* (VB_D). The map of Bluth and Kump (1991) holds ca. 14 % volcanic rocks split evenly between *basalt* and *rhyolite* with a very small amount of *andesite*. While *basalt* of Bluth and Kump (1991) still contain 29 % VB+VI in the new map, *rhyolite* only is represented by 7 % VA and 7 % VI while it contains 29 % SU, 16 % SS, 9 % SM, 9 % PA and 7 % SC. *Basalt* from the map of Amiotte-Suchet et al. (2003) contain 42 % VB + 13 % VI, 26 % SU+SS and 9 % VA. However, the *acid volcanic rocks* are dominated by SU and SS (47 %) and contain a proportion of VB (16 %) that is more than double that of VA (7 %), the rest is made up of VI (8 %). The map of Dürr et al. (2005) does not show any occurrences of acid and intermediate volcanic rocks. *Basic volcanic rocks* are composed of 28 % VB, 12 % VI and 8 % VA in the new map, plus 25 % SS+SU and 6 % SM+SC.

Table 3: Comparison of the four existing lithological maps covering North America. Comparable lithological classes are combined into the one used by this study, even if nomenclature of the source map differs slightly.

Lithology	This study Area %	Dürr et al. (2005) Area %	Amiotte-Suchet et al. (2003) Area %	Bluth and Kump (1991) Area %
Dune sands (DS)	0.35 %			
Evaporites (EV)	0.26 %			0.89 %
Loess (LO)	0.16 %	3.58 %		
SUM "exotic" sediments	0.77 %	3.58 %	0.00 %	0.89 %
Carbonate sedimentary rocks (SC)	11.05 %	13.74 %	15.54 %	23.28 %
Mixed sedimentary rocks (SM)	13.94 %	11.05 %		
SUM carbonate-rich sediments	24.99 %	24.79 %	15.54 %	23.28 %
Sand / sandstone			10.05 %	23.52 %
Shale			30.84 %	32.73 %
Siliciclastic sedimentary rocks (SS)	23.42 %	15.69 %		
Unconsolidated sediments (SU)	13.30 %	6.88 %		
Alluvial deposits (AD)	0.29 %	3.79 %		
Coal				0.08 %
Chert				0.77 %
Complex lithology (CL)		7.13 %		
SUM siliciclastic sediments	37.01 %	33.49 %	40.89 %	57.10 %
Plutonic / metamorphic			34.30 %	
Metamorphic rocks (MT)	12.68 %	19.16 %		
Precambrian shields (PR)		4.76 %		3.06 %
Acid plutonic rocks (PA)	12.32 %	6.55 %		
Basic plutonic rocks (PB)	0.56 %	0.04 %		
Intermediate plutonic rocks (PI)	1.24 %			
SUM metamorphic / plutonic	26.80 %	30.51 %	34.30 %	3.06 %
Acid volcanic rocks (VA)	0.99 %		5.88 %	7.31 %
Basic volcanic rocks (VB)	3.96 %	5.78 %	0.76 %	6.72 %
Intermediate volcanic rocks (VI)	1.70 %			0.34 %
Pyroclastics	0.26 %			
SUM volcanic	6.91 %	5.78 %	6.64 %	14.37 %
Ice / glaciers (IG)	0.40 %			
Water bodies (WB)	2.51 %	1.83 %	2.62 %	1.30 %
Unknown (UN)	0.62 %			
SUM other units	3.53 %	1.83 %	2.62 %	1.30 %

Table 4: Comparison between the lithological classes of this study and those in the map of Bluth and Kump (1991). This table reads only per row; it translates to how each lithological class of Bluth and Kump (1991) is represented by current lithological classes. Marked combinations directly correspond to each other.

Bluth and Kump (1991)	NULL A)	AD	DS	EV	LO	SC	SM	SS	SU	This study MT	PA	PB	PI	VA	VB	VI	PY	WB	IG	UN
NULL A)	0.0%	0.4%	0.0%	0.2%	0.0%	20.8%	18.9%	11.2%	11.3%	9.7%	5.8%	0.6%	2.0%	0.2%	2.3%	1.7%	0.1%	11.8%	0.5%	2.6%
Evaporites	0.3%	0.0%	0.0%	0.0%	0.0%	32.0%	38.1%	11.4%	0.0%	0.7%	5.9%	0.0%	0.0%	0.0%	0.5%	3.1%	0.0%	6.0%	0.0%	2.1%
Chert	0.1%	0.0%	0.0%	0.0%	0.0%	0.6%	8.9%	20.5%	26.2%	16.7%	6.3%	1.3%	0.7%	4.3%	7.0%	6.4%	0.4%	0.5%	0.0%	0.1%
Carbonates	0.4%	0.0%	0.2%	0.2%	0.0%	11.7%	13.8%	6.5%	5.8%	24.1%	30.5%	1.3%	0.2%	0.4%	2.9%	0.7%	0.0%	1.2%	0.0%	0.2%
Sandstone	0.2%	0.1%	0.9%	0.0%	0.1%	5.9%	10.2%	33.4%	21.1%	11.6%	7.5%	0.3%	0.9%	0.7%	3.4%	1.1%	0.2%	0.8%	1.2%	0.4%
Sandstone sub B)	1.0%	0.0%	0.0%	0.0%	0.0%	0.0%	57.1%	41.9%	0.0%	0.0%	0.0%	0.0%	0.0%	0.0%	0.0%	0.0%	0.0%	0.0%	0.0%	0.0%
Shales	0.2%	1.0%	0.2%	0.9%	0.1%	9.4%	17.0%	34.0%	17.4%	5.3%	7.8%	0.3%	0.3%	0.7%	2.4%	0.7%	0.0%	1.5%	0.2%	0.6%
Coal-b. shales C)	0.4%	0.0%	0.0%	0.2%	0.0%	19.7%	17.9%	41.0%	7.6%	4.8%	2.5%	0.2%	1.1%	0.1%	1.6%	0.7%	0.1%	1.0%	0.4%	0.7%
Coal	1.0%	0.0%	0.0%	0.0%	0.0%	0.8%	40.5%	53.7%	0.0%	0.0%	0.0%	1.0%	0.0%	0.0%	2.9%	0.0%	0.0%	0.0%	0.0%	0.0%
Shield	1.1%	0.0%	0.0%	0.0%	0.0%	2.6%	10.1%	2.4%	0.0%	48.9%	27.7%	0.5%	1.7%	0.6%	2.9%	0.8%	0.0%	0.1%	0.0%	0.6%
Rhyolite	0.1%	0.9%	1.1%	0.4%	0.0%	7.1%	9.2%	16.1%	28.8%	6.3%	9.2%	0.1%	0.9%	6.5%	6.8%	4.5%	1.1%	0.6%	0.0%	0.2%
Andesite	0.0%	0.0%	0.0%	0.0%	0.0%	2.6%	17.1%	22.5%	0.0%	32.7%	12.3%	0.8%	5.9%	0.3%	4.6%	1.5%	0.0%	0.0%	0.0%	0.0%
Basalt	0.2%	0.2%	0.1%	0.0%	2.1%	2.0%	8.2%	16.5%	10.4%	9.1%	9.0%	0.8%	7.1%	2.3%	19.2%	9.4%	1.7%	0.6%	0.3%	0.7%
Basalt-sub B)	1.4%	0.0%	0.0%	0.0%	0.0%	0.2%	11.8%	0.8%	0.0%	22.8%	4.0%	0.4%	54.2%	0.0%	0.8%	2.0%	0.5%	0.0%	0.8%	0.2%
Ocean	0.0%	0.0%	0.0%	0.0%	0.0%	23.3%	5.2%	9.3%	0.0%	4.7%	3.5%	0.1%	0.0%	0.2%	2.4%	0.1%	0.0%	51.3%	0.0%	0.0%

A) NULL means that area is not covered by one map that is covered by the other.

B) sub = subaerial deposition.

C) Coal bearing shales.

Table 5: Comparison between the lithological classes of this study and those in the map of Amiotte-Suchet et al. (2003). This table reads only per row; it translates how each lithological class of Amiotte-Suchet (2003) is represented by current lithological classes. Marked combinations directly correspond to each other.

Amiotte-Suchet et al. (2003)	This study																			
	NULL A)	AD	DS	EV	LO	SC	SM	SS	SU	MT	PA	PB	PI	VA	VB	VI	PY	WB	IG	UN
NULL A)	0.0%	0.4%	0.0%	0.0%	0.0%	23.9%	16.2%	9.6%	8.6%	10.8%	4.9%	0.6%	2.7%	0.1%	2.4%	2.2%	0.0%	15.5%	0.4%	1.6%
Carbonate	0.7%	0.3%	0.3%	1.1%	0.0%	34.2%	23.6%	19.6%	10.0%	2.9%	2.8%	0.3%	0.1%	0.2%	0.7%	0.4%	0.0%	1.7%	0.0%	1.3%
Sand/S.stone	0.0%	1.7%	1.6%	0.0%	0.1%	5.4%	3.9%	35.3%	48.1%	0.5%	0.4%	0.0%	0.0%	0.1%	1.2%	0.2%	0.1%	1.0%	0.0%	0.2%
Shale	0.2%	0.1%	0.3%	0.0%	0.1%	8.6%	18.5%	44.7%	13.0%	2.9%	1.8%	0.3%	1.6%	0.5%	3.7%	1.8%	0.2%	0.4%	1.1%	0.2%
Plutonic / metamorphic	0.4%	0.0%	0.0%	0.2%	0.0%	3.0%	9.5%	8.4%	2.5%	32.4%	32.8%	1.0%	1.8%	1.0%	4.1%	1.3%	0.2%	0.6%	0.2%	0.6%
Acid volcanic	0.0%	0.3%	0.8%	0.0%	2.2%	3.7%	5.1%	10.2%	36.9%	1.8%	4.3%	0.1%	0.4%	7.5%	15.8%	7.6%	2.3%	0.7%	0.0%	0.1%
Basalts	0.3%	0.3%	0.3%	0.0%	1.8%	0.6%	0.7%	10.5%	16.0%	1.0%	1.0%	0.0%	0.2%	8.5%	41.5%	12.6%	0.2%	1.8%	0.0%	2.7%
Water	0.9%	0.0%	0.0%	1.2%	0.0%	16.8%	15.4%	10.8%	0.0%	5.8%	8.9%	2.2%	0.1%	0.3%	1.4%	0.4%	0.0%	35.0%	0.1%	0.5%

A) NULL means that area is not covered by one map that is covered by the other.

Table 6: Comparison between the lithological classes of this study and those in the map of Dürr et al. (2005). This table reads only per row; it translates how each lithological class of Dürr et al. (2005) is represented by current lithological classes. Marked combinations directly correspond to each other.

Dürr et al. (2005)	this study																			
	NULL [A)]	AD	DS	EV	LO	SC	SM	SS	SU	MT	PA	PB	PI	VA	VB	VI	PY	WB	IG	UN
NULL[A)]	0.0%	0.0%	0.0%	0.0%	0.0%	24.6%	19.6%	7.6%	3.5%	10.2%	3.6%	0.5%	2.0%	0.1%	1.6%	1.2%	0.0%	18.7%	0.0%	6.7%
AD$_D$	0.2%	3.3%	0.9%	1.0%	0.1%	3.5%	3.3%	9.0%	66.7%	1.2%	2.7%	0.1%	0.0%	2.1%	1.8%	1.9%	0.5%	1.7%	0.0%	0.1%
LO$_D$	0.0%	0.0%	1.8%	0.0%	0.7%	28.2%	13.2%	34.8%	20.0%	0.0%	0.0%	0.0%	0.0%	0.0%	0.5%	0.2%	0.1%	0.7%	0.0%	0.0%
SC$_D$	0.5%	0.5%	0.3%	0.9%	0.0%	32.3%	21.3%	20.5%	15.9%	2.4%	2.1%	0.2%	0.3%	0.2%	1.4%	0.4%	0.1%	0.6%	0.1%	0.1%
SM$_D$	0.0%	0.3%	0.7%	0.1%	0.0%	23.8%	14.8%	40.8%	13.8%	2.8%	0.8%	0.1%	0.0%	0.2%	0.4%	0.1%	0.0%	1.2%	0.0%	0.1%
SS$_D$	0.2%	0.2%	0.4%	0.1%	0.0%	3.7%	18.4%	59.6%	12.5%	1.4%	1.1%	0.1%	0.1%	0.2%	1.1%	0.5%	0.0%	0.3%	0.0%	0.1%
SU$_D$	0.3%	0.3%	1.2%	0.1%	0.0%	2.3%	8.3%	39.5%	39.6%	1.2%	1.0%	0.1%	0.2%	0.5%	1.9%	2.2%	0.0%	0.7%	0.5%	0.0%
CL$_D$	0.6%	0.1%	0.0%	0.1%	0.1%	6.3%	18.7%	15.8%	6.7%	13.0%	14.5%	1.1%	2.5%	2.2%	9.8%	4.2%	0.2%	0.3%	3.0%	0.7%
MT$_D$	0.5%	0.0%	0.0%	0.0%	0.0%	1.0%	8.0%	1.9%	0.5%	41.7%	39.3%	0.9%	0.8%	0.6%	3.6%	0.7%	0.0%	0.1%	0.0%	0.5%
PR$_D$	0.4%	0.0%	0.0%	0.7%	0.1%	5.6%	28.1%	11.1%	4.9%	28.5%	9.8%	2.3%	1.3%	0.5%	3.8%	1.8%	0.2%	0.6%	0.2%	0.0%
PA$_D$	0.2%	0.0%	0.1%	0.2%	0.1%	1.2%	6.2%	4.9%	5.1%	19.5%	41.7%	1.8%	8.4%	1.5%	3.9%	2.4%	0.3%	0.4%	1.5%	0.8%
PB$_D$	2.7%	0.0%	0.0%	0.0%	0.0%	0.0%	43.2%	0.0%	0.0%	5.5%	16.9%	20.3%	1.0%	0.2%	10.2%	0.0%	0.0%	0.0%	0.0%	0.0%
VB$_D$	1.1%	0.3%	0.1%	0.0%	2.0%	2.2%	4.1%	11.4%	17.1%	3.4%	3.3%	0.4%	3.1%	7.7%	27.7%	11.6%	3.2%	0.5%	0.6%	0.3%
WB$_D$	0.1%	0.0%	0.0%	1.2%	0.0%	14.2%	6.5%	8.3%	0.1%	0.9%	3.1%	0.2%	0.0%	0.1%	0.3%	0.1%	0.0%	61.7%	0.0%	3.1%

[A)] NULL means that area is not covered by one map that is covered by the other.

2.6 Example for application of lithological maps: Geochemistry of the earth surface

Apart from being employed as a tool in models of elementary fluxes from chemical weathering (compare chapters 3 and 4), lithological maps can also be a tool to determine the elemental composition of earth's terrestrial surface. The terrestrial surface is not only the easiest accessible part of the lithosphere, but also the part in which most relevant reactions for the exogenic cycles take place. It is the lower boundary of the so called "critical zone", understanding of which is an interdisciplinary challenge for earth scientists (Brantley et al., 2007).

A study presented by Hartmann et al. (submitted) reviews literature extensively to quantify the elementary contents of the lithological classes from the global lithological map of Dürr et al. (2005). The resulting elementary contents for sodium and calcium were compared with findings of elementary content regionally calibrated in North America, using a large rock analysis database (Chapter 4.3.3). Global application of the elemental compositions of the lithological map show that the terrestrial surface is depleted in individual elements (e.g. sodium) when compared to the upper crust. Hartmann et al. (submitted) attribute this loss to weathering, which dissolves elements with different rates from individual minerals (e.g. Goldich, 1938). Other elements (e.g. calcium) are enriched on the terrestrial surface when compared to the continental crust. This is in part attributed to carbonate-rich marine sediments that are uplifted at active continental margins (Hartmann et al., submitted).

2.7 Conclusions from lithological map development

Comparison of the different lithological maps of North America shows that although the existing maps agree on the general picture with the here presented new map, details, especially for less abundant lithological classes, differ largely. However, even small rock occurrences, especially of weathering-affine lithological classes like *evaporites*, *carbonate sedimentary rocks*, or *basic volcanic rocks* (Meybeck, 1987), can change elementary fluxes induced by chemical weathering significantly. Thus, they are important to be adequately represented by a lithological map.

Nevertheless, the here presented map is certainly not perfect. Inconsistencies between the underlying geological classifications of the source maps induce error (compare the lithological classes in figure 2). Additionally, the coverage of the large loess areas of North America (Bettis et al., 2003) could be improved, which is underestimated in the map because it is likely to be too thin for inclusion in the geological source maps. The class *metamorphic rocks* (MT) still comprises of a large number of different rock types with different characteristics with regard to weathering. In future maps, this class could be extended into two classes. One class would be used for basic metamorphic

rocks (e.g. amphibolite, greenstone) and one for acid metamorphic rocks and shale, which are more resistant to weathering. Further, especially regarding a future global lithological map, thick laterites should be acknowledged, as they, although not rocks themselves, shield bedrock from weathering and thus reduce elementary fluxes (Stallard and Edmond, 1983; Edmond et al., 1995; Porder et al., 2007). Furthermore, rock age, which has been suggested as factor influencing rock weathering rates (e.g. Dahlgren et al., 1999) could be included in future versions of the map.

The studies presented in the following chapters do not fully exploit the potential of the YY and ZZ levels of the lithological map (Table 2). Nevertheless, those levels are subject to further research and could be improved in future versions of the lithological map.

Concluding the comparison to previous lithological maps covering North America, it should be emphasized that lithology is a scale dependent parameter. The lithological classes of the different maps show a different rock composition and different spatial representations. Thus, models and functions developed with one lithological map should be applied to others only with great care and considering the regionally different rock compositions of each lithological class.

3 Dissolved silica mobilization in the conterminous USA

3.1 Introduction

Dissolved silica is a major nutrient for many aquatic systems and certain terrestrial plants (e.g. Epstein, 1999; Ragueneau et al., 2009). Although much of it passes through a biogenic silica pool and is recycled therein, ecologically available dissolved silica (DSi; representing SiO_2) starts its path in the silicon cycles with chemical weathering of silicate rocks (Derry et al., 2005). If the weathering agent is atmospheric/soil CO_2, cations resulting from the dissolution of silicates can form a long-term sink for CO_2. The transformation of silicate rocks to carbonate rocks is a major control of long-term climate changes in earth history (Kempe and Degens, 1985; Berner, 1995; Ludwig et al., 1998; Hartmann et al., 2009).

Following its mobilization by chemical weathering, large parts of the DSi pass through terrestrial biologic silica cycles (cf. Alexandre et al., 1997; Conley, 2002) before reaching continental aquatic systems. Within those, more biologically induced silica cycles exist that may lead to retention in lakes and reservoirs (cf. Conley et al., 1993; Humborg et al., 2006) before being transported towards the oceans. Output from rivers is a major source of DSi in coastal waters (DeMaster, 1981; Treguer et al., 1995; Kristiansen and Hoell, 2002; Beusen et al., 2009; Dürr et al., 2009; Ragueneau et al., 2009) and a major control of algal community composition (Officer and Ryther, 1980). DSi limitation can lead to harmful algal blooms (Smayda, 1990) and its abundance influences the oceanic carbon pump (Sieracki et al., 1993). For an overview of the biologic effects of DSi in coastal waters see Ragueneau et al. (2009). The catchments used in this study are picked for minimal influence of silica transformation processes to highlight the factors controlling DSi mobilization by chemical weathering.

The literature focusing DSi mobilization is scarce. Thus, and because silicate weathering represents the "ultimate" source of ecologically available DSi (Derry et al., 2005), literature on silicate weathering is included when assessing potential factors of DSi mobilization.

A combination of runoff and lithology has been identified as major control of silicate rock weathering rates and associated DSi fluxes in many studies. Previous studies compared sub-catchments dominated by different rock types (e.g. Horton et al., 1999), or large numbers of monolithological catchments (Meybeck, 1987; Bluth and Kump, 1994), to isolate weathering rates for single rock types (the "monolithological approach"). More recent global scale studies use a multilithological approach, incorporating aerial proportions of lithological classes in analyzed catchments (Beusen et al., 2009;

Hartmann et al., 2010). Gibbs (1967) already used aerial proportions of lithological classes for water salinity statistics of multiple catchments.

In the laboratory, temperature has been shown to increase weathering rates of individual minerals (Brady and Carroll, 1994) and rock types (diorite: White et al., 1999a; basalt: Navarre-Sitchler and Brantley, 2007). In field studies focusing on single lithologies, a positive relation between temperature and weathering rate was shown for basaltic (Brady et al., 1999) and granitic (White and Blum, 1995; Oliva et al., 2003; Riebe et al., 2004) catchments as well. However, despite the knowledge of its relevance for chemical weathering reactions, regional and global studies assessing more complex lithological settings could not identify temperature as major predictor for DSi fluxes from the terrestrial into the fluvial system (Beusen et al., 2009; Hartmann et al., 2010). Nevertheless, temperature influence may be represented in those studies through correlations with other applied predictors.

Runoff and temperature in the weathering environment are influenced by the presence of soil (c.f. Raymond et al., 2008). Furthermore, the respiration of organic matter in soils increases CO_2 partial pressure tremendously, which has been shown to increase weathering rates in simulations (Schwartzman and Volk, 1989), the laboratory (Berg and Banwart, 2000) and in local field studies (Navarre-Sitchler and Thyne, 2007). Nevertheless, thick soils can limit rock weathering rates by shielding the rock from weathering agents (cf. Stallard and Edmond, 1983; Boeglin and Probst, 1998; Rad et al., 2006). Yeast and filamentous fungi (Eckhardt, 1979) as well as organic ligands (Brady and Carroll, 1994; Berg and Banwart, 2000) have been shown in laboratory studies to intensify silicate mineral weathering rates. In plot scale studies, lichens (Brady et al., 1999) and trees (Moulton et al., 2000) have been shown to increase basalt rock weathering rates compared to non-vegetated catchments. On coarser scales, the relation between land cover and DSi mobilization is difficult to assess. Internal Si-cycling between plant tissues, soil solution, and soil minerals is significant, compared to the export of DSi into the fluvial system (Alexandre et al., 1997; Lucas, 2001; Conley, 2002; Conley et al., 2008). DSi export also varies largely with the growing state of the ecosystem (Fulweiler and Nixon, 2005; Conley et al., 2008); internal plant Si storage even fluctuates with grazing stress (Massey et al., 2007). A significant predictor to represent the influence of land cover on silicate weathering rates has hitherto not been identified on continental or global scales.

Supply of fresh, unweathered material is essential for chemical silicate weathering to proceed (Raymo et al., 1988; Dalai et al., 2002; West et al., 2005). The quantity of available fresh parent rock material is closely related to physical denudation rates, whose influence is represented by a number of factors in literature. For longer timescales, terrigenous sediment abundance or Sr isotope ratios are used as indicators for physical weathering (Berner and Kothavala, 2001). Drever and Zobrist

(1992) show a negative relation between elevation and DSi concentration for Alpine catchments, which they interpret as representing a combination of the potential factors physical denudation, temperature and soil thickness. Gradient of slope has been utilized as predictor for DSi mobilization in Japan, which is characterized by steep slopes (Hartmann et al., 2010). However, the complex influence of gradient of slope on physical denudation (Montgomery and Brandon, 2002; Aalto et al., 2006) impedes interpretation of this predictor with respect to material supply for chemical weathering. Other studies use parameters representing suspended river sediment to describe physical denudation (Gaillardet et al., 1999; West et al., 2005; Hagedorn and Cartwright, 2009). Apart from physical denudation, weathering exposition time is a potential factor on fresh material availability. It was found to significantly decrease DSi fluxes in an experimental field study with young volcanic tephra (Dahlgren et al., 1999).

Although many factors influencing chemical silicate weathering are well known from laboratory and local scale, their effects are still not clearly identified on continental or global scale. This study investigates the hypothesis that lithology and runoff exert a major influence on DSi mobilization (Bluth and Kump, 1994; Hartmann et al., 2010). To test this hypothesis, multilithological model equations similar to those introduced by Hartmann et al. (2010) are applied and tested on catchments with little anthropogenic influence in the conterminous USA, using a new lithological map with increased resolution. Scatter plots of model residuals are analyzed for trends correlating with additional parameters to identify further potential factors of DSi mobilization. Using this method, and applying data with significantly improved spatial resolution, factors not identified in previous studies on large scales (e.g. Bluth and Kump, 1994) could be established. The transferability of regionally calibrated models to other world regions, or even the whole world, is discussed by comparing our results to those of previous studies (Bluth and Kump, 1994; Hartmann et al., 2010).

3.2 Methods and Data

A schematic view of the methodology applied is shown in figure 5; details are described in the following chapters.
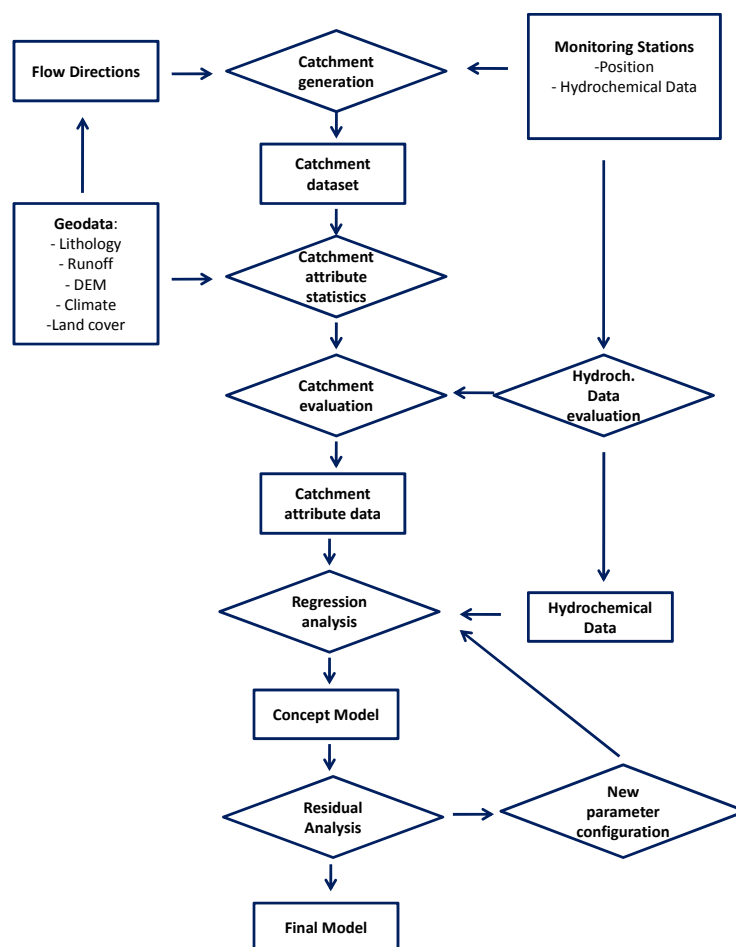
Figure 5: Schematic diagram of the study workflow. From geodata, catchments and their attributes are calculated and evaluated. Regression analyses are performed with the catchment attributes and redone with other parameter settings after residual analysis in an iterative process to eventually find a final model.

A lithological map was developed for North America using published geological maps. A detailed description of the map is given in chapter 2. However, some lithological classes hold only very small mapped areas in the analyzed catchments. To maintain model robustness, these classes were aggregated with others: The four unconsolidated sedimentary classes *alluvial deposits* (AD), *dune sediments* (DS), *loess* (LO) and *unconsolidated sediments* (SU) were condensed in the class SU+ (compare Table 1). *Basic volcanic rocks* (VB) and *pyroclastics* (PY), both expected to show high weathering rates and characterized by a comparable chemical composition, were combined as VB+. *Basic* (PB) and *intermediate* (PI) *plutonic rocks* were combined as PB+. *Acid* (VA) and *intermediate* (VI) *volcanic rocks* were combined as VA+, following Dürr et al. (2005). The 18 original classes of the lithological map as well as the nine lithological classes used in this study and their abbreviations are shown in table 7; mostly abbreviations will be used in the following.

Table 7: Lithological classes used in this study, their abbreviations and aerial proportion in the conterminous USA and in the area of the catchments used for model calibration.

Herein used abbreviation	Lithologic classes from the Map	Proportion of conterminous USA [%]	Proportion of assessed catchments [%]
SU+[A)]	Unconsolidated sediments (SU)	28.86	20.53
	Dune sands (DS)	0.87	0.12
	Loess (LO)	0.41	0.28
	Alluvial deposits (AD)	0.73	0.30
SS	Siliciclastic sedimentary rocks (SS)	29.81	38.48
SM	Mixed sedimentary rocks (SM)	6.45	7.32
SC	Carbonate sedimentary rocks (SC)	11.73	10.79
MT	Metamorphic rocks (MT)	5.73	6.25
PB+[A)]	Basic plutonic rocks (PB)	0.28	0.31
	Intermediate plutonic rocks (PI)	0.17	0.06
PA	Acid plutonic rocks (PA)	3.91	5.75
VB+[A)]	Basic volcanic rocks (VB)	4.29	5.98
	Pyroclastics (PY)	0.37	0.12
VA+[A)]	Acid volcanic rocks (VA)	1.60	0.89
	Intermediate volcanic rocks (VI)	1.93	2.69
WB	Water bodies (WB)	2.73	0.11
--	Evaporites (EV, not analyzed in this study)	0.11	0.02
--	Ice and glaciers (IG, not analyzed in this study)	0.00	0.00

[A)] For simplicity, the combined lithological classes (indicated by the "+") will later be addressed with the name of their dominating individual class: e.g. "Unconsolidated sediments (SU+)".

All catchment parameters were calculated using the functionality of the software ArcGIS (ESRI® Version 9.3.1). The HYDRO1k digital elevation model for North America (USGS, 2000) with a resolution of 1 km^2 was used to calculate the catchment parameters "mean altitude" and "gradient of slope" as well as to draw the geographical extent of the selected catchments. For comparison, the highly DEM-resolution-sensitive (Wolock and McCabe, 2000) factor gradient of slope was also calculated using a SRTM digital elevation model with a spatial resolution of 3 arc seconds (ca. 100 x 100 m, Jarvis et al., 2006).

Runoff data were obtained from the Global Runoff Data Center (GRDC - Fekete et al., 2000). Even though the spatial resolution is low (0.5°), that dataset is calibrated with river discharge and thus is expected to represent a sufficiently realistic runoff (Fekete et al., 2002). Runoff data were used as a model predictor as well as for calculating DSi yields from DSi concentrations. Average precipitation and temperature of the catchments, as well as their seasonality, were obtained from the WorldClim dataset with a grid size of 30" (Hijmans et al., 2005).

Land cover data were taken from the GLOBCOVER dataset (Arino et al., 2007). Some of the original classes were rearranged in this study to reduce the number of parameters. Original and rearranged

classes are shown in table 8. Data on irrigated areas were obtained from the global irrigation map (Siebert et al., 2005). A subset of the SOTER global soil dataset (Batjes, 2006) was used to derive predictors for soil-pH, C_{org} content and bulk density. Population density data from the gridded population of the world v3 were used (CIESIN and CIAT, 2005).

Table 8: Land-cover classes from Arino et al. (2007), their aerial abundances in the conterminous USA and in the area of the catchments that were assessed for model calibration, as well as the classes used in this study

Class Number	Class used in this study	Original class name	Proportion of conterminous USA [%]	Proportion of assessed catchments [%]
LC1	Cultivated land	A11 - cultivated terrestrial areas and managed lands	18.13	21.23
LC2	Broadleaved forest	A12 - natural and semi-natural terrestrial vegetation - woody / trees / broadleaved	29.63	25.73
LC3	Needle leaved forest	A12 - natural and semi-natural terrestrial vegetation - woody/ trees / needle-leaved	16.74	21.19
LC4	Shrubs	A12 - natural and semi-natural terrestrial vegetation - shrubs	14.77	7.56
LC5	Grasslands	A12 - natural and semi-natural terrestrial vegetation - herbaceous	15.97	23.53
LC6	Sparse	A12 - natural and semi-natural terrestrial vegetation	0.00	0.00
LC7	Aquatic vegetation	A24 - natural and semi-natural aquatic vegetation	0.69	0.15
LC8	Artificial surfaces	B15 - artificial surfaces and associated areas - urban > 50 %	0.39	0.05
LC9	Bare areas	B15 - artificial surfaces and associated areas - bare areas	0.08	0.01
LC10	Water and ice	B28 - inland water bodies	3.60	0.57

Hydrochemical data from the WQN and NAWQA networks (Alexander et al., 1996; USGS, 2008b) were combined into one dataset containing 4 508 monitoring stations. From these stations a subset was selected according to two main criteria: 1) At least twelve consecutive monthly measurements of DSi concentration and instant discharge must be available to calculate meaningful annual averages. 2) Annual averages must provide a matching ion balance (Error < 10 %). The positions of stations matching these criteria were fitted onto a HYDRO1k derived river network. Stations that could not be accurately positioned or whose calculated catchments were obscured by channels or artificial waterways were omitted. For the remaining stations, catchments were calculated using ArcGIS 9.3 (ESRI®) "Spatial Analyst"-functionality and flow direction data from HYDRO1k. The calculated catchment areas were checked for consistency with given monitoring station information on the contributing drainage area and with a second river dataset (ESRI, 2008). Catchments satisfying the previous criteria were visually checked for anthropogenic or water-body influence using population density, land cover and water-body data (CIESIN and CIAT, 2005; Arino et al., 2007; ESRI, 2008). If water bodies or larger settlements were situated at the main stem of the river, a major

tributary or close to the monitoring station, that station was omitted. Additionally, average GRDC-runoff was required to be above zero for each catchment, as streams providing twelve chemical analyses per year are expected to show at least some runoff. Of the 4 508 stations, 142 passed all criteria; their average DSi fluxes were included into the analysis, covering 313 annual cycles of DSi flux data. The average catchment size of the monitoring stations is 3 890 km^2; the covered area sums up to 552 000 km^2 (Figure 6). Descriptive statistics of all catchment parameters are given in table 9.

Table 9: Descriptive statistics of the average catchment characteristics. Data sources are given in the main text.

	Mean	Median	Minimum	Maximum	Std.dev.
Area [km²]	3900	820	10	37000	7500
SiO$_2$ [µ mol L^{-1}]	164.5	129.2	29.27	807.4	116.3
SiO$_2$ [t km^{-2}a^{-1}]	2.684	2.240	0.000	23.137	2.826
GRDC-runoff [mm a^{-1}]	344.5	286.5	0.054	2283	307.4
Gradient of slope H1k [°] [A]	2.138	0.706	0.057	10.55	2.597
Gradient of slope SRTM [°] [B]	6.149	2.931	0.481	26.00	6.019
Pop.density [capita km^{-2}]	170.0	145.4	3.000	931.2	141.9
EV [aerial %]	0.0	0.0	0.0	0.3	0.000
MT [aerial %]	7.8	0.0	0.0	99.8	0.192
SC [aerial %]	17.8	0.7	0.0	100.0	0.280
SM [aerial %]	7.4	0.0	0.0	99.9	0.173
SS [aerial %]	33.1	20.5	0.0	100.0	0.355
WB [aerial %]	0.1	0.0	0.0	1.2	0.002
PA [aerial %]	5.2	0.0	0.0	100.0	0.156
PB+ [aerial %]	0.5	0.0	0.0	20.9	0.023
VA+ [aerial %]	2.4	0.0	0.0	65.9	0.095
VB+ [aerial %]	3.8	0.0	0.0	93.1	0.121
SU+ [aerial %]	22.0	1.2	0.0	100.0	0.350
Precipitation [mm a^{-1}]	950.0	938.6	319.2	2707	386.4
Temperature [°C]	9.362	9.022	-2.336	20.41	5.545
LC1 [aerial %]	18.0	8.6	0.0	80.8	20.5
LC2 [aerial %]	34.9	28.6	0.0	100.0	27.5
LC3 [aerial %]	26.3	15.0	0.0	99.8	29.4
LC4 [aerial %]	3.6	0.0	0.0	48.5	8.3
LC5 [aerial %]	16.7	12.8	0.0	74.3	14.8
LC8 [aerial %]	0.0	0.0	0.0	0.3	0.1
LC9 [aerial %]	0.0	0.0	0.0	0.5	0.1
LC10 [aerial %]	0.3	0.0	0.0	5.2	0.7
Soil-pH [C]	2.708	2.852	1.000	4.568	0.826
Soil Corg [C]	2.796	2.907	1.462	4.000	0.657
Soil Bulk density [C]	4.329	4.109	2.000	5.370	0.596
Mean altitude [m]	834.3	409.5	11.64	3648	907.7
Irrigated lands [ha cell^{-1}]	12633	198.9	0.000	509915	50494

[A] Values from HYDRO1k-dataset with approximately 1000x1000m cell resolution.

[B] Values from SRTM-dataset with approximately 100x100m cell resolution.

[C] Soil parameters are classified in the original data. They do not provide units.
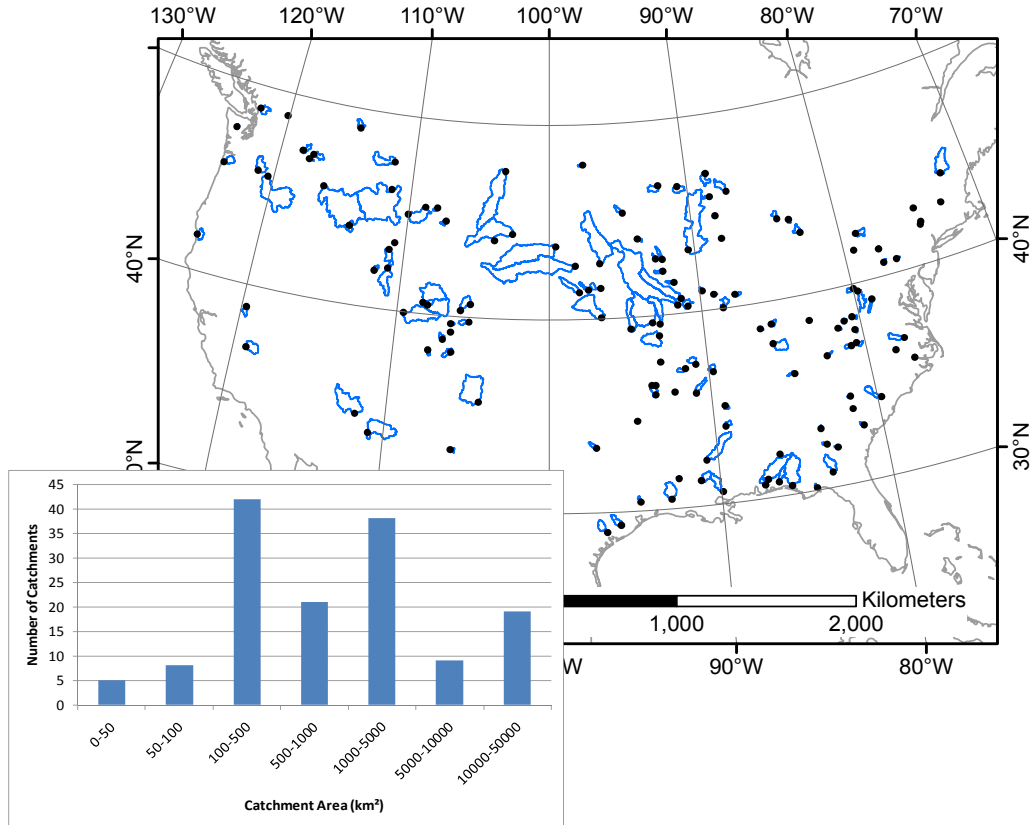
Figure 6: Monitoring station locations (and shapes of their catchments) assessed in this study and distribution of catchment sizes. Average catchment size is 3 890 km². For monitoring stations where no catchment is visible, the catchment is smaller than the space the dot representing the site location occupies.

DSi yields (given in t SiO_2 km^{-2} a^{-1}) are the product of discharge-weighted annual average concentrations and long-term GRDC-runoff (Fekete et al., 2000). Discharge-weighted annual average DSi yields provide better estimates of "real" yields than those calculated with arithmetic annual means (e.g. Fulweiler and Nixon, 2005). Discharge weighting (cf. Kempe, 1982; Sferratore et al., 2006) of DSi concentrations and other water chemistry parameters was done using the measured instant discharge, while GRDC-runoff was used to calculate yield from discharge-weighted concentrations as described in equation 1.

$$\text{Equation 1)} \quad f_{DSi} = \frac{\sum_1^i \frac{\sum_1^n c_{DSi,n,i} \cdot Q_{n,i}}{\sum_1^n Q_{n,i}} \cdot (q \cdot A)}{i \cdot 1000}$$

Equation 1: Discharge weighting for each catchment using measured DSi concentration (c) and instant discharge (Q) per twelve month period (i) and month (n) as well as GRDC-runoff (q) and the catchment area (A).

Discharge-weighted DSi flux with f_{DSi} = DSi yield [t SiO_2 km^{-2} a^{-1}], c = concentration [mg L^{-1}], Q = instant discharge measured at the site and time of sampling [L s^{-1}], i = number of available full twelve month periods, n = number of sample month within i, and q = GRDC-runoff for each catchment [L a^{-1} m^{-2}]. The equation is divided by 1 000 to change the unit from mg m^{-2} a^{-1} to t km^{-2} a^{-1}. The model aims at

33

understanding long-term processes, therefore q, which represents long-term runoff, was used to calculate yields, while Q, which reflects the situation in the moment of sampling, was used for discharge weighting. For 74 considered catchments, additional daily discharge data were available from NAWQA data and used for comparison of resulting DSi yields.

To examine the potential controlling factors of DSi mobilization, multilithological model equations similar to those introduced in Hartmann et al. (2010) were applied in the conterminous USA and tested for statistical significance using the software Statistica 8.0 (STATSOFT®). Scatter plot analysis for trends of relative model residuals with excluded parameters were used to identify further potential controlling factors of DSi mobilization. To include those factors, model equations were adapted (incorporating different parameter configurations) and analyzed again in an iterative process. For the scatter plot analysis of relative residuals that will be discussed below, one single station with a relative residual of -6.9 was treated as an outlier and thus omitted. Relative residuals were calculated as division of the term observed minus predicted by observed. The model that best combines prediction quality and parameter significance is described and discussed below.

3.3 Results

The observed DSi yield of the catchments ranges from 0.0004 to 23.1 t SiO_2 km^{-2} a^{-1}, with an average of 2.68 t SiO_2 km^{-2} a^{-1}. Ten percent of the catchments show an average yield larger than 4.48 t SiO_2 km^{-2} a^{-1} (Figure 7). The total flux from the area of the 142 catchments is 974 * 10^3 t SiO_2 a^{-1} (1.76 t SiO_2 km^{-2} a^{-1}). This is less than the average yield of 2.2 t SiO_2 $km^{-2}a^{-1}$ for the whole North American continent as calculated by Dürr et al. (2009). Note the difference between area weighted flux and per catchment flux. Comparison of area weighted mean flux and per-catchment average mean flux implies a negative correlation between runoff and catchment size, which is also observed in the data (r=-0.27, p=0.001).

To highlight the influences of discharge weighting and applied runoff datasets, in a subset of 74 catchments for which both instant discharge and daily discharge data were available, discharge-weighted and unweighted DSi yields are compared. Unweighted yields are calculated as product of arithmetic mean concentrations and mean annual runoff data. In those catchments, the average weighted DSi yield is 2.43 t SiO_2 km^{-2} a^{-1}. The average unweighted DSi yields of the 74 catchments, calculated with GRDC-runoff, average measured instant discharge and average daily discharge are 2.67, 3.69 and 2.85 t SiO_2 km^{-2} a^{-1}, respectively. Discharge weighting results in a reduction of yields compared to unweighted discharge. The use of the discharge dataset, however, induces another uncertainty. Using average daily discharge results in slightly higher DSi yields than GRDC-runoff, but

DSi yields calculated from instant discharge data are significantly higher than those of both other datasets.
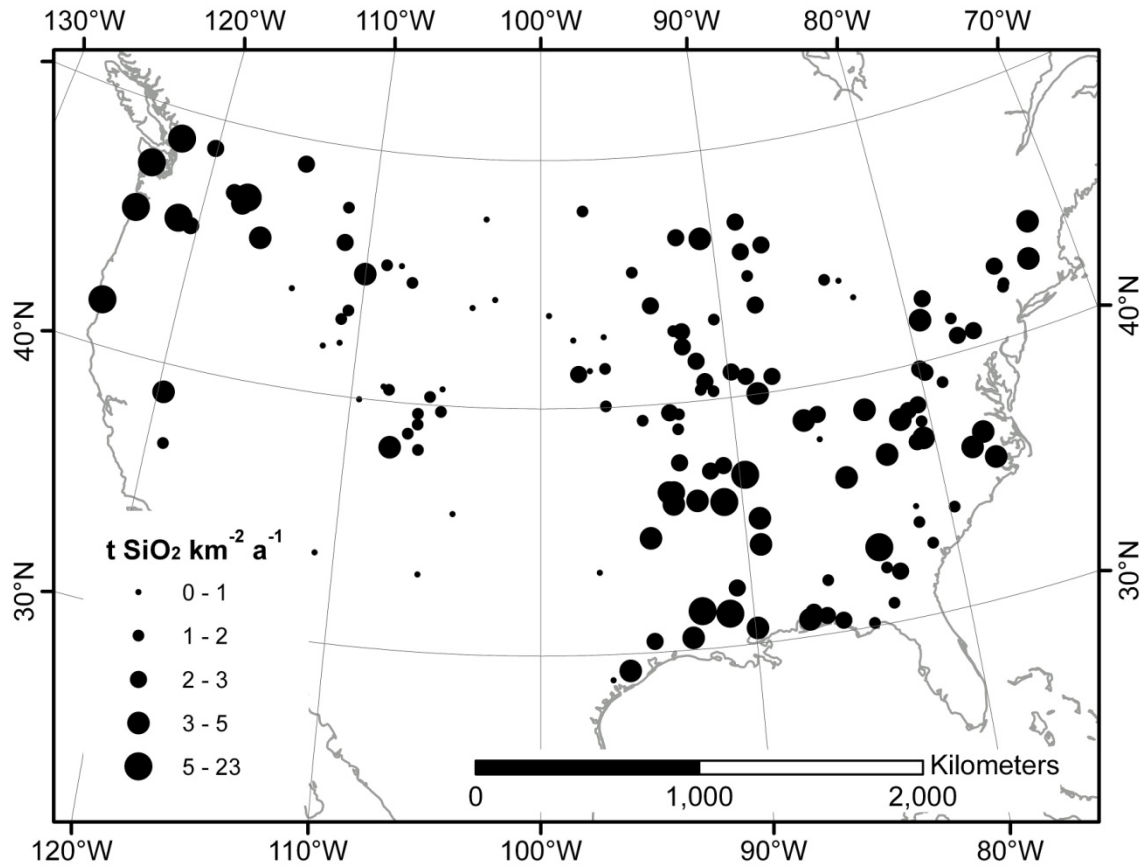
Figure 7: Observed average DSi yields of the monitoring stations assessed in this study. The average DSi yield of all catchments is 2.68 t SiO_2 km^{-2} a^{-1}.

The most important predictor for DSi yield identified in this study is runoff. This parameter results in a correlation coefficient of r=0.72 when applied as in equation 2 with b_0 and b_1 being parameters calculated by the Levenberg-Marquardt estimation method implemented in the software Statistica 8.0 (Table 10).

Equation 2) $f_{DSi} = b_0 \cdot q^{b1}$

Equation 2: Model equation for DSi yield (f_{DSi}) calculated from GRDC-runoff (q) and two parameters which are derived using least square methods (b_0, b_1).

Table 10: Nonlinear regression parameters for the DSi mobilization model that uses runoff as single predictor.

Parameter	Estimation	Standard deviation	p-Level	Confidence interval (p=95 %)
b_0	0.011	0.005	0.027	± 0.010
b_1	0.933	0.067	<0.001	± 0.132

The correlation for the model in equation 2 may be expected, as runoff is also used as parameter to calculate the yield that the model predicts. However, it also shows that other factors need to be considered to model DSi yields.

Discriminating between different lithological classes adds 0.22 to the correlation coefficient of the model using only runoff as predictor. The combination of lithology and runoff (Equation 3) results in the best relation between description of observed yields and the number of parameters needed of all tested model equations (r = 0.944, 10 parameters, p_{max}=0.001, figure 8 A).

Equation 3) $f_{DSi} = b_0 \cdot \sum_1^n L_n \cdot q^{b_n}$

Equation 3: Model equation to calculate DSi yield (f_{DSi}) using GRDC-runoff (q) and aerial proportion of each lithological class n (L_n). It uses one general (b_0) and a set of lithology-specific b-parameters (b_n)

Table 11: Nonlinear regression parameters for the model that uses runoff and lithology as predictors. Parameters from the Japan-model, calibrated using data from Japan (Hartmann, 2009)[A] are given for comparison. Details are given in the text.

Parameter	Estimation	Standard deviation	p-Level	Confidence interval (p=95 %)	b-parameter est. by the Japan-model for comparison [A]
b_0	0.028	0.009	0.001	± 0.017	0.018
b_{MT}	0.793	0.057	<0.001	± 0.113	0.834
b_{PA}	0.705	0.082	<0.001	± 0.162	0.956
b_{PB+}	1.010	0.038	<0.001	± 0.074	n.a. [B]
b_{SC}	0.776	0.054	<0.001	± 0.107	n.a. [B]
b_{SM}	0.753	0.077	<0.001	± 0.152	0.954
b_{SS}	0.717	0.045	<0.001	± 0.088	0.934
b_{SU+}	0.797	0.050	<0.001	± 0.099	SU[C]: 0.939 AD[C]: 1.056
b_{VA+}	0.819	0.070	<0.001	± 0.139	0.911
b_{VB+}	1.004	0.046	<0.001	± 0.090	VB[C]: 1.031 PY[C]: 1.166

[A] The data published with Hartmann (2009) were used to recalculate their model according to equation 5 and incorporate only runoff and lithology. All b-parameters are significant (p_{max}=0.003).

[B] This lithological class was not calibrated in Japan.

[C] Hartmann (2009) used individual lithological classes that had to be aggregated in this study.

In equation 3, f_{DSi} is DSi yield (t SiO_2 km^{-2} a^{-1}), b_0-b_n are least-square derived model parameters, shown in table 11, L_n is the relative aerial proportion of each given lithology in the catchment and q is GRDC-runoff.

The model predicts a total DSi flux of 923 * 10^3 t SiO_2 a^{-1} (1.67 t SiO_2 km^{-2} a^{-1}), 5 % less than the observed flux. The model residuals show an almost normal distribution (Figure 8 B). The model results appear robust for the observed parameter realm.
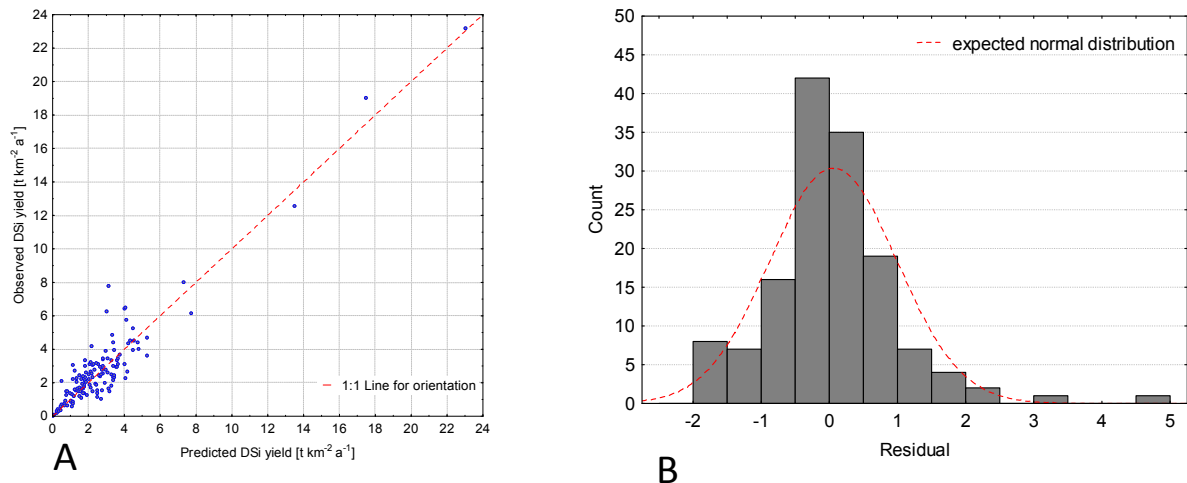
Figure 8: Details of the model: A) Observed DSi yield plotted versus model predicted DSi yields of 142 modeled catchments. The correlation coefficient between predicted and observed yields is 0.944. B) Distribution of model residuals. Although the shown residuals are not perfectly normal distributed, no significant bias of the model is expected as the distribution is close to symmetric.

The model results in varying DSi yields for the different lithological classes and a given runoff. The highest yields are obtained from the basic igneous lithological classes VB+ and PB+ (Figure 9). The rocks with the second highest yield are *acid volcanic rocks* (VA+), whose DSi yield at a given runoff of 350 mm (about the average of the analyzed catchments) amounts to 34 % of VB+. *Unconsolidated sediments* and *metamorphic rocks* (SU+, MT) follow with 30 % and 29 % of the DSi yields of VB+ at that runoff, respectively. *Carbonate sedimentary rocks* (SC) yield 26 %, more than *mixed sedimentary rocks* (SM, 23 %) and *siliciclastic sedimentary rocks* (SS, 19 %). The least yielding rock types are *acid plutonic rocks* (PA), with 17 % of the DSi yield of VB+ for 350mm runoff. As b_n is different from 1 for all but the basic igneous lithological classes, the relative differences of DSi yield increase with runoff.

Adding further parameters, e.g. slope (either HYDRO1k or SRTM derived), temperature or land cover, to the model equation does not improve the model as parameters become insignificant on the 5 % level or redundancies prevent model calculation.
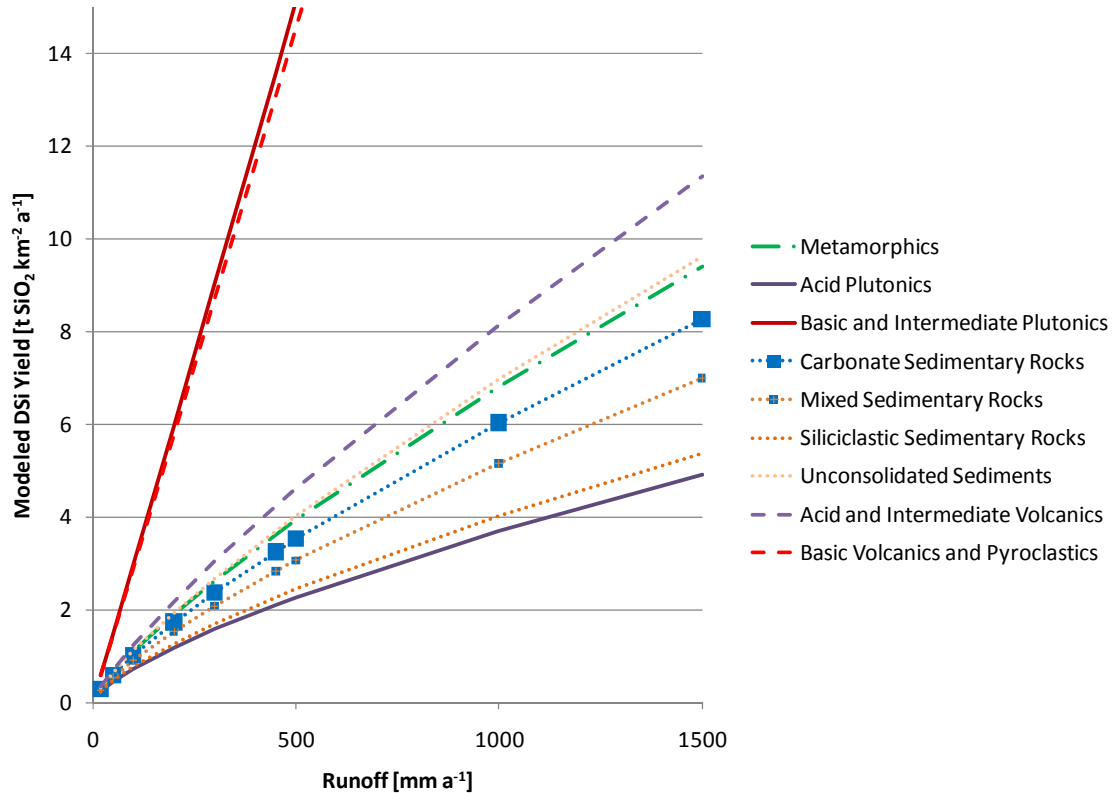
Figure 9: Modeled DSi yields per runoff for different lithological classes. Basic Igneous Rocks yield most DSi, followed by acid and intermediate volcanic rocks, unconsolidated Sediments, metamorphic rocks, sedimentary rocks in reverse order of their (designated) carbonate content and acid plutonic rocks. Note that the average runoff of the assessed catchments is 344 mm a^{-1}.

3.4 Discussion

3.4.1 Influences on DSi yield

3.4.1.1 Runoff

Interpretation of processes leading to the empirically derived predictors of the model is complex. Reducing DSi mobilization to a system of the two components appearing in the model equation (runoff and lithology), would lead to the assumption that runoff exponents of 1 (like for the basic igneous lithological classes VB+ and PB+) implied a transport limitation of DSi yields, while smaller exponents (for all other lithological classes) hint to a kinetic limitation. The first case implicates DSi concentrations to remain constant at any given runoff, while in the latter case DSi is mobilized too slowly to provide a constant concentration of dissolved ions (cf. Schnoor, 1990; Kump et al., 2000; West et al., 2005). However, such a simple relation between runoff and DSi mobilization is not to be expected (e.g. Porder et al., 2007).

The exponents of runoff in the model could also represent another process chemical weathering rates and runoff are closely linked to. Numerous studies relate chemical weathering rates to physical

erosion rates, representing the supply of fresh mineral surfaces for weathering (Gaillardet et al., 1999; Dalai et al., 2002; Millot et al., 2002; West et al., 2005). In general, suspended particulate material (SPM) in rivers is related to physical weathering, although its use as descriptor is impaired by sedimentation effects unaccounted for (e.g. Gaillardet et al., 1999) and the need for frequent measurements to represent short yet important peaks in sediment load (cf. Coynel et al., 2004). SPM has been shown to be correlated to runoff in small catchments (Collins, 1981). However, Milliman and Syvitsky (1992) report only weak positive trends for SPM with increasing runoff, while they suggest basin size and topography as major controls on SPM.

Knowing its complexity, we assess the relation of SPM to DSi yield and its predictors runoff and lithology. In our data, SPM concentrations are available for 107 monitoring stations. SPM yields (calculated as product of GRDC-runoff and discharge-weighted SPM concentration, the same way as DSi yields are calculated) do not show a significant correlation to DSi yields (r=0.09, p=0.35). Neither SPM yields nor weighted SPM concentrations show a significant correlation to GRDC-runoff (r=-0.10, p=0.30; r=-0.18, p=0.07 respectively). The average sediment yield calculated from SPM for the 107 catchments is 67.6 t km^{-2} a^{-1}. Collins (1981) stated that SPM yield per runoff would change with rock types (they found higher maximum concentrations on sandstone and clay bedrock than on chalk). However, in our study dataset a significant correlation between mean weighted SPM concentration and aerial lithology proportion is only observed for the lithological class SM (r=0.284, p=0.003). Analysis for catchments dominated by single lithological classes (aerial proportion > 50 %) did also not yield significant correlations between SPM yield and DSi yield. Although it is known that physical erosion is one of the driving forces of chemical erosion, it does not seem that the SPM parameter is correlated to DSi in this study. Possibly, the used SPM yields do not accurately describe physical denudation because they are calculated from infrequent (monthly) concentration data and sedimentation processes are not considered in their interpretation. Although the effectiveness of the predictor runoff is likely not to be simply explained by water supply effect alone, the exact processes governing the different behavior of the lithological classes with increasing runoff remain ambiguous.

3.4.1.2 Lithology

Increasing the spatial resolution of lithological data and differentiating between rock compositions is beneficial for DSi mobilization modeling because DSi mobilization changes significantly with lithology. Nevertheless, increasing data resolution also requires advancements in modeling techniques, as can be observed when comparing the map presented here to the lithological map by Bluth and Kump (1991). Applying the lithological map of Bluth and Kump (1991), 111 of the 142 catchments assessed here are composed of one single lithological class. Five of ten lithological classes of that map show ten or more monolithological catchments. Using the new lithological map, just 22 of the 142

catchments are monolithological. Only one out of nine used classes provides more than ten monolithological catchments for statistical analysis. Thus, the monolithological approach, used in past analyses of small catchments (e.g. Meybeck, 1986), should be extended to a multilithological approach (Hartmann, 2009; Hartmann et al., 2009; Hartmann et al., 2010).

The variation of DSi yields between lithological classes is foremost credited here to the rocks' different mineral compositions as well as their different textural and structural characteristics. Basic igneous rocks (VB+, PB+) yield the most DSi relative to runoff; they contain large proportions of highly weatherable silicates such as olivine and pyroxene. *Acid volcanic rocks* (VA+) are also subject to rapid chemical weathering. This is attributed to possible contents of unstable volcanic glass and high porosity. These characteristics are absent in *acid plutonic rocks* (PA), from which the least DSi is mobilized. *Metamorphic rocks* (MT) are a heterogeneous group of rock types, including gneiss, schist and amphibolite, that show highly variable erosion rates (Meybeck, 1987). The more easily weathered rock types within that lithological class may be responsible for its high modeled DSi yield. Contrary to their (per definition) low SiO_2 content, *carbonate sedimentary rocks* (SC) show the highest DSi yield of the consolidated sedimentary lithological classes, followed by *mixed sedimentary rocks* (SM) and *siliciclastic sedimentary rocks* (SS). We suggest, the reason for this is amorphous SiO_2 (ASi) that may be contained in the carbonates (e.g. DeMaster, 1981) and which exhibits a far higher solubility than crystalline silicon (Miretzky et al., 2001). SU+ is a very heterogeneous lithological class, combining carbonate-rich loess sediments with quartz-dominated dune sands and alluvial floodplains. High DSi yields for SU+ could be caused by the floodplains that, like SC, are expected to contain ASi.

Furthermore, correlations between lithology and other catchment attributes could influence modeled DSi yields of the lithological classes. Especially for SU+, there is a significant positive correlation to temperature, which is discussed below and could cause a positive bias in the SU+ DSi yield. Correlation analysis between gradient of slope (calculated from SRTM data) and the lithology proportions of the catchments was conducted to find correlations between lithology and gradient of slope. A positive correlation exists for PA (r=0.31, p<0.001), SS (r=0.22, p=0.008) and VA+ (r=0.36, p<0.001), while SC (r=-0.21, p=0.011), SM (r=-0.18, p=0.029) and SU+(r=-0.29, p<0.001) show negative correlations. These correlations might influence the b-parameters of the lithological classes by adding influences on DSi mobilization from controlling factors related to gradient of slope.

3.4.1.3 Temperature

A significant correlation between temperature and DSi mobilization has been identified exclusively in the laboratory or monolithological field settings until now (Brady and Carroll, 1994; White and Blum, 1995; Brady et al., 1999; White et al., 1999a; Dessert et al., 2003; Oliva et al., 2003; Riebe et al.,

2004; Navarre-Sitchler and Brantley, 2007). Studies assessing actual heterogeneous field situations on large scales did not find significant relations between temperature and DSi yield (Beusen et al., 2009; Hartmann et al., 2010). In this study, average annual temperature varies from -2.3°C to 20.4°C, with a mean of 9.4°C. Analyzing all 142 considered catchments, no significant correlation between relative model residuals and temperature could be observed (r=0.11, p=0.21). However, a strong correlation exists between the lithological class SU+ and temperature (r=0.52, p<0.001), which results mostly from a cluster of SU+ dominated catchments in the southeastern US, showing high temperatures (Figure 10 A). If just catchments with less than 10 % aerial proportion of SU+ are considered (n=90, the smallest dot-size in figure 10 A), a distinct correlation between relative model residuals and temperature is observable (r=0.35, p<0.001; figure 10 B). This shows an increasing underestimation of the model for higher temperatures. We suggest that this trend in relative model residuals of catchments with small SU+ proportions supports a relation between temperature and DSi mobilization.

Although temperature could not be isolated as a significant predictor in the applied model, it is nonetheless partly included in both model predictors. Apart from the discussed correlation to lithology, runoff includes temperature both in the precipitation (correlated to temperature: r=0.41, p<0.001) and evaporation components, although there is no significant direct correlation between runoff and temperature.
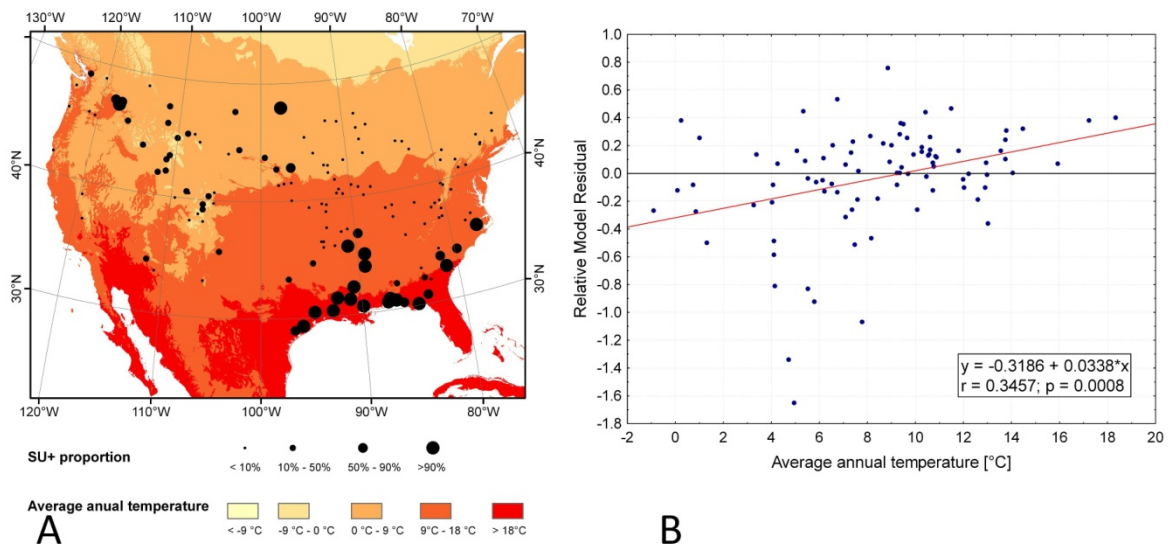
Figure 10: Correlations with temperature. A) Graduated symbols for monitoring stations according to the SU+ (Unconsolidated Sediments) aerial proportion. The background shows average annual temperature (Hijmans et al., 2005). A clustering of SU+-rich catchments can be observed in the warm regions of south-eastern U.S. This explains the correlation between SU+ and temperature. B) A positive trend (r=0.35, p=0.001) is observable for relative model residuals with increasing temperature, if only catchments with less than 10 % aerial SU+ proportion are assessed (n=90). Relative model residuals are calculated as observed minus predicted divided by observed.

3.4.1.4 Land cover / Vegetation

Land cover, representing vegetation, was suggested to influence the chemical environment of weathering (e.g. Eckhardt, 1979; Schwartzman and Volk, 1989; Drever, 1994; Brady et al., 1999; Bonneville et al., 2009). In this study, a weak but significant positive correlation between relative model residuals and the aerial coverage of land-cover classes LC1 and LC5 (LC1: "Cultivated Terrestrial Areas and Managed Lands", which includes crops; LC5: "Natural and Semi-natural Terrestrial Vegetation – Herbaceous", which includes grasslands) is identified (r=0.19, p=0.025; figure 11 A). Correspondingly, broad-leaved and needle-leaved forest land-cover classes (LC2 and LC3) show a negative correlation to model residuals (r=-0.19, p=0.024). Both groups amount to more than 90 % of the catchment area of all but 20 catchments.

Additionally, the average relative residuals of two subsamples (One including catchments with LC1+LC5 smaller than 30 % of the catchment area (n=82), the second including catchments with LC1+LC5 greater than 70 % of the catchment area (n=29)) are tested for the hypothesis that they originate from a different population. In a two-sample Kolmogorov-Smirnov Test as well as a Mann-Whitney U Test this hypothesis is not discarded and the significance-level is p<0.001 (Histograms shown in figure 11 B).

The underestimation of model results of catchments containing high proportions of land cover classes LC1 and LC5 suggests that more DSi is exported from grassy than from forested areas. The correlations could, however, also be attributed to cross-correlations with other predictors, which are discussed in the following before further elaborating on the influence of vegetation on DSi yields.

The land cover class proportions of LC1 and LC5 show no significant correlation to average catchment temperatures (r=0.04, p=0.668). Moreover, the regional distribution of LC1 and LC5 (Figure 11 A) does not reflect the distribution of temperature (Figure 10 A) in North America. However, all four dominating land cover class proportions are correlated to runoff (LC2: r=0.24, p=0.004; LC3: r=0.26, p=0.003; LC1: r=-0.33, p<0.001; LC5: r=-0.34, p<0.001) and a number of significant correlations exist between lithology and land cover. The proportion of grassland related land cover classes (LC1 and LC5) per catchment is positively correlated to the proportion of carbonate-rich sedimentary rocks in the assessed catchments (SC: r=0.32, p<0.001; SM: r=0.40, p<0.001) and negatively to that of metamorphic rocks (MT: r=-0.24, p=0.004), basic plutonic rocks (PB+: r=-0.19, p=0.023) and volcanic rocks (VA+: r=-0.18, p=0.031; VB+: r=-0.21, p=0.012). However, relative model residuals do not show a significant correlation to runoff (r=0.06, p=0.42) or any of the lithological classes, which underlines the robustness of the model. Thus, lithology, runoff and temperature are not identified to explain the observed trend of relative residuals with land cover.
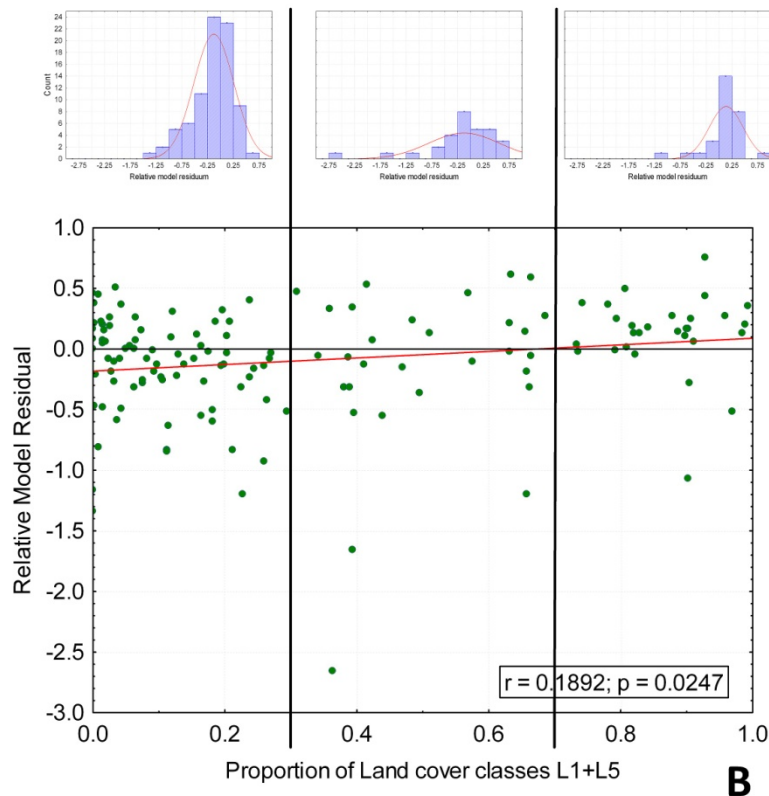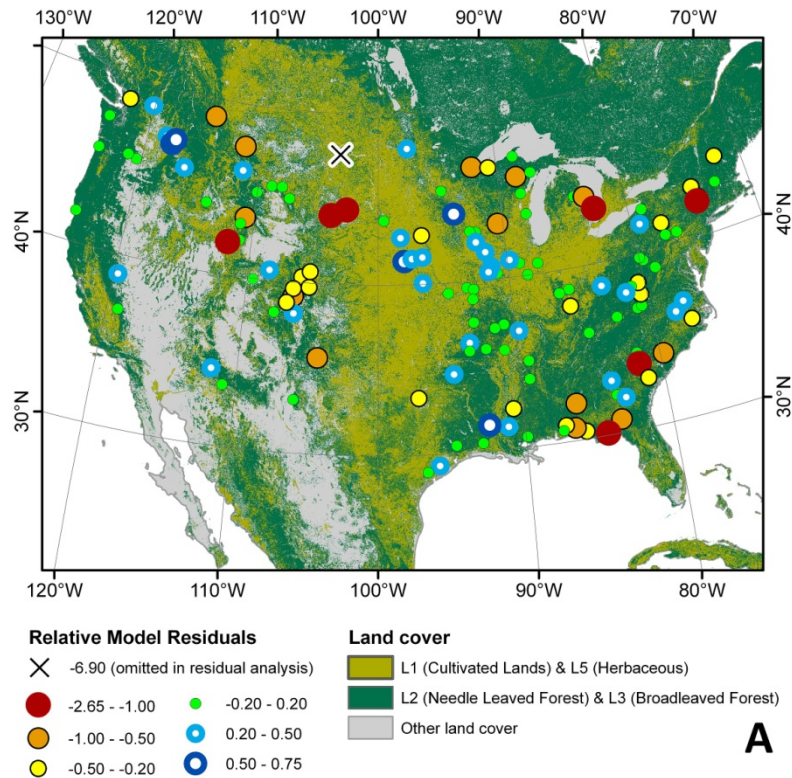
Figure 11: A) Distribution of land cover classes LC1 and LC5 (Cultivated Lands and Herbaceous) and LC2 and LC3 (Needle Leaved Forest and Broadleaved Forest) (Arino et al., 2007). Monitoring station relative residuals are shown; one monitoring station is marked that was omitted in residual analysis as an outlier. B) Trend of relative model residuals for increasing LC1+LC5 catchment proportion (r=0.19, p=0.025). Relative model residuals are calculated as observed minus predicted divided by observed. Histograms for three subsamples selected by LC1+LC5 proportion smaller 0.3, between 0.3 and 0.7 and larger 0.7 show the significantly different average relative residuals for the lowest and highest proportion.

Terrestrial ecosystems exhibit significant internal silicon cycles (cf. Epstein, 1994; Alexandre et al., 1997; Conley, 2002; Struyf et al., 2009) which may in part explain the observed trend of relative residuals. A different intensity of the internal Si cycles for different vegetation species could influence the DSi output of land cover classes. Blecker et al. (2006) demonstrate that silica turnover times are faster in grasslands of the Great Plains than in two temperate forest ecosystems in France (studied by Bartoli 1983). They hypothesize a positive impact of the faster silica cycling on mineral dissolution (Blecker et al., 2006). Different intensities in silica cycling can lead to differences in amorphous silica (ASi) pools in ecosystems (cf. Epstein, 1994; Conley, 2002). For instance, grass contains more ASi than forests (Saccone et al., 2007). Furthermore it has been shown that conifers and associated soils contain less ASi than deciduous species (Saccone et al., 2008) and between grass types ASi contents vary about threefold (Blecker et al., 2006). Even within single species, large variation of ASi content can be introduced by external factors like grazing stress (Massey et al., 2007).

The relative residual analysis suggests that land cover can be a further significant predictor to increase prediction quality of future models and represent vegetation influence on DSi fluxes.

3.4.1.5 Other factors

Relative residuals of the employed model are also related to DSi concentration itself (Figure 12). Large concentrations (> 200 μmol L^{-1}) tend to be under-predicted by the model while small concentrations show a tendency to be over-predicted. This is attributed to the model generation process. Modeled DSi yield is a product of concentration and runoff. For runoff, the variability is higher than for concentration (coefficient of variation of 89 % versus 71 %). Runoff is thus expected to dominate the statistical adjustment of the model parameters. Just about half (54 %) of the absolute flux from the calibrating catchments originates from catchments with DSi concentrations below 200 μmol L^{-1}. Furthermore, as there is no apparent correlation between concentration and yield this error does not appear to seriously bias the model output.
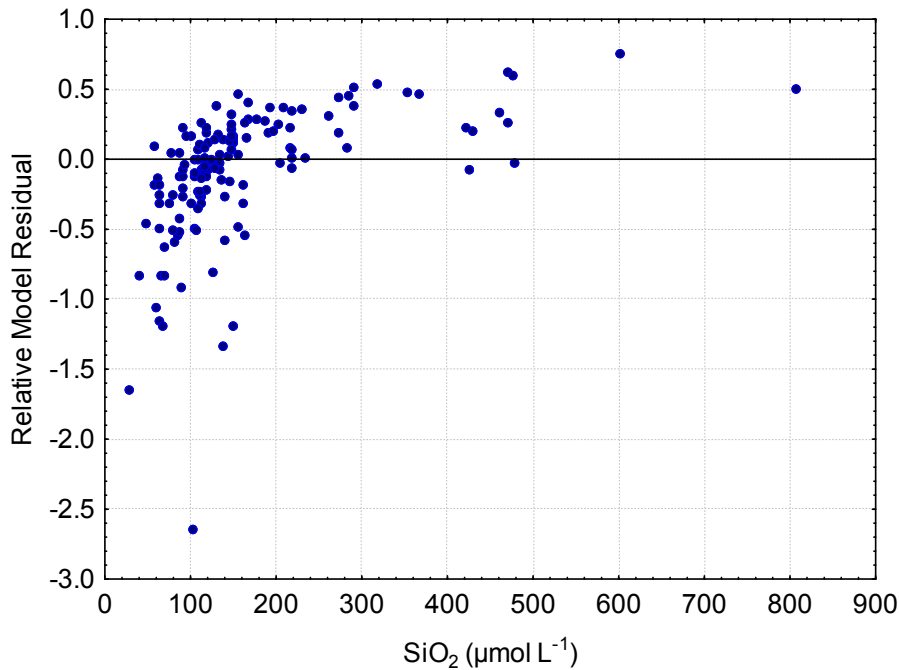
Figure 12: Relation between average weighted SiO₂ concentration and relative model residuals. Relative model residuals are calculated as observed minus predicted divided by observed. It is expected that for small DSi concentrations the absolute values of relative residuals increases. However, the scatter plot shows that above concentrations of 200 μmol L⁻¹ the model strongly tends to underestimate DSi yield.

Other meaningful correlations could not be identified. Gradient of slope was shown to be a predictor for DSi flux in Japan (Hartmann et al., 2010). However, in our study its influence could be isolated neither for gradient of slope calculated from HYDRO1k nor for that calculated from SRTM data. For each catchment, average gradient of slope calculated from SRTM is higher than that of HYDRO1k (average values for 142 catchments are 6.15° and 2.14° respectively). The correlation between both slope parameters is high (r=0.96, p<0.001). However, no significant correlations between DSi yields and gradient of slope (HYDRO1k or SRTM) could be established. The absence of slope as a prominent predictor for DSi yield, in contrast to results from Japan (Hartmann et al., 2010), could be attributed to statistical reasons. Catchment average SRTM calculated gradients of slope for calibration of the Hartmann et al. (2010) model were higher and more homogenous (mean: 13,54°, median: 13.12°) than those in this model (mean: 6.15°, median 2.93°).

With regard to weathering processes, the factor gradient of slope could have an ambivalent relation to DSi mobilization. On the one hand, increasing slope gradient is expected to increase average drainage intensity of water and to reduce the proportion of groundwater on total runoff; both effects reduce DSi yield. On the other hand, a general positive relation between gradient of slope and fresh material supply through physical denudation (cf. Ahnert, 1970) would increase DSi yield. However, the exact relation between local slope and physical denudation is complex, including hillslope processes, lithology types and river channel processes in different landscapes (Montgomery and Brandon, 2002; Montgomery, 2003; Aalto et al., 2006).

45

3.4.2 Comparison to previous studies

To our knowledge, our study is the first approach that explicitly focuses on natural dissolved silica mobilization using a multi-lithological model and minimizing retention influence as well as human influence on a large number of catchments from a large geographical setting as the conterminous USA.

A study of Hinderer (2006) highlights not DSi mobilization itself, but the total chemical denudation rate of silicate rocks. That study proposes low chemical denudation rates of granite, and larger rates for metamorphic rocks and sandstone dominated regions of southern Germany. Meybeck (1987) agrees on small chemical erosion rates of granite while siliciclastic sediments in the French streams he analyzed show a chemical denudation rate 1.3 times that of granite. Meybeck (1987) distinguishes between "gneiss and mica schist" as well as "serpentine and amphibolite" which show weathering rates of 1.0 and 5 times that of granite. Those rocks are combined within the here used lithological class MT. According to Meybeck (1987), gabbro shows a weathering rate 1.3 times, and volcanic rocks 1.5 times higher than granite. For comparison, DSi mobilization rates of the associated lithological classes calculated with our model are 1.07 (for SS), 1.68 (for MT) and 5.78 (for VB) relative to PA, for a runoff of 350mm. The significant differences to Meybeck (1987) may arise from regionally different weathering settings. Furthermore, this study assesses DSi mobilization while Meybeck (1987) focused on "chemical erosion rates", which include major elements and could include non-silicate weathering educts.

Two studies modeling DSi similar to this have been published previously by Bluth and Kump (1994) and Hartmann et al. (2010). Bluth and Kump (1994) used 98 catchments, mostly from the conterminous USA, to calibrate a model of DSi yields predicted by runoff and five lithological classes (basalt, granite, carbonate, sandstone, shale). Hartmann et al. (2010) used 516 catchments in Japan to predict DSi yields, introducing a multilithological approach with comparable lithological classes as those employed here. Their model identified lithology, runoff and gradient of slope as the most prominent predictors. To enable a direct comparison between the models, a model according to equation 5 (incorporating only runoff and lithology) has been developed for the published Japanese catchment data (Hartmann et al., 2010). The DSi yields per runoff for the model applied by Hartmann et al. (2010), including slope, and the newly calculated one, with just runoff and lithology as predictors, are similar. The newly calculated model will be called "Japan-DSi model". Values of b-parameters are given in table 11. A direct comparison between the results of Bluth and Kump (1994), the Japan-DSi model and our study is shown in figure 13 A to F.
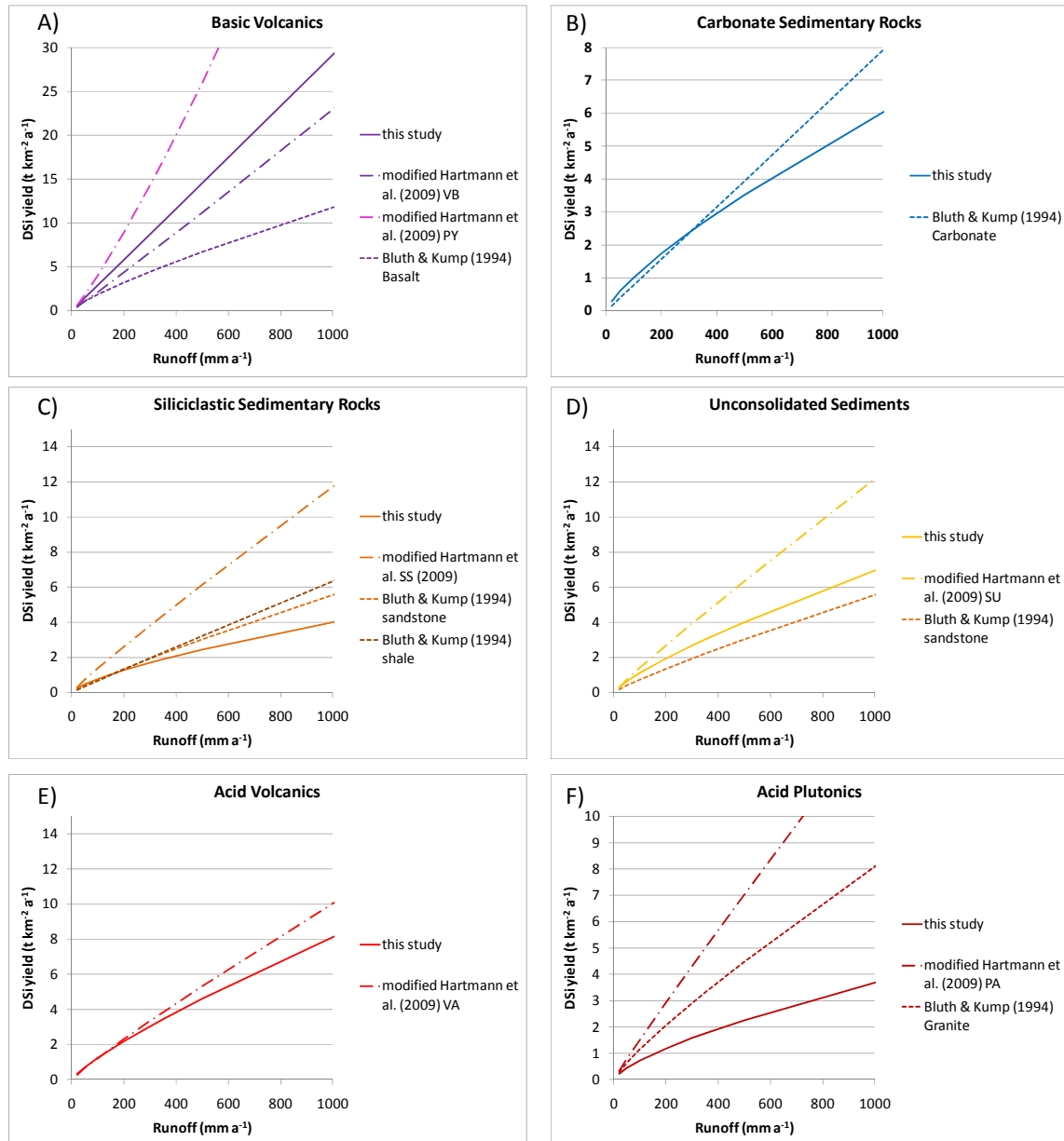
Figure 13: Comparison between results of Bluth and Kump (1994, mostly USA), a modified model from Hartmann et al. (2010, Japan - see text for description) and this study for comparable lithological classes. Figure parts A) - F) compare one lithological class of this study to corresponding lithological classes. For Carbonate Sedimentary Rocks (SC) and Acid Volcanic rocks (VA+), resulting DSi yields per runoff are similar, for the other lithological classes, the observed differences are discussed in the text.

For *basic volcanic rocks* (VB+), our study results in the highest DSi yields of all three studies (Figure 13 A). The difference to the results of the Japan-DSi model is attributed to classification. Hartmann et al. (2010) were able to distinguish between *pyroclastics* (PY) and VB, which in this study are combined as VB+. As shown in figure 13 A, PY shows a higher yield than VB in the Japan-DSi model and higher than VB+ in this study. A mix of PY and VB would result in DSi yields in the same order as those of this study. The reason why *basalt* in the study of Bluth and Kump (1994) results in a far lower DSi yield than VB+ in this study is not quite clear. One likely explanation is that of the 33 basaltic catchments analyzed by Bluth and Kump (1994), 14 were situated on the Hawaiian archipelago. Studies for

Hawaii report that the initially high weathering rates of the basalts decline significantly with time (Stewart et al., 2001; Porder et al., 2007). Kennedy et al. (1998) report that in soils older than 20 000 years, less than 15 % of the calcium in soils originate from source rock weathering, the rest being added by aeolian dust deposition. Chadwick et al. (1999) report that in soils older than 100 000 years, dust becomes the dominant source of major nutrients (except phosphorous) for ecosystems. On the island of Hawaii, inspection of lava from the Mauna Kea produced Hamauka Series in the erosive Kukaiau Cave showed that vesicles of the lava and fractures in the lava have been sealed by allophane, preventing surface water to reach large volumes of bedrock and thus reducing available rock surfaces for weathering (Kempe and Werner, 2003). Weathering restraints by soils have also been reported for the Amazon region (Stallard and Edmond, 1983). Even if DSi should be more resistant to leaching than other nutrients (like phosphorous: Chadwick et al., 1999), at least in the 11 catchments of Bluth and Kump (1994), situated in the lower, flatter regions on islands other than the island of Hawaii (the youngest of the Hawaiian archipelago), soil could shield bedrock from weathering.

Carbonate sedimentary rocks (SC) were not assessed by Hartmann et al. (2010) because they cover only 0.3 % of the Japanese archipelago. The modeled yields for SC by Bluth and Kump (1994) and this study are similar (Figure 13 B). For low runoff values, this study predicts higher DSi yields, while for runoffs higher than approximately 300 mm a^{-1}, Bluth and Kump (1994) predict higher yields.

For *siliciclastic sedimentary rocks* (SS), the Japan-DSi model results in the highest DSi yields relative to runoff (Figure 13 C). Consolidated sediments in Japan, which are mostly of marine origin, can contain biogenic opal and have gone through fewer sedimentation cycles compared to those assessed in the two American studies. However, contamination with fresh pyroclastic ashes could increase DSi mobilization. The results of Bluth and Kump (1994) for their classes *sandstone* and *shale*, the closest to SS, are again similar to this study. For runoff values above 150 mm a^{-1} the equation of Bluth and Kump (1994) results in higher DSi yields. However, while Bluth and Kump (1994) differentiate between *carbonates* and *sandstone/shale* only, this study additionally uses the classes *mixed sedimentary* rocks (SM) and *unconsolidated sediments* (SU). Both show higher DSi yields than SS. We thus attribute the DSi yield difference for SS to the increased detail of the classes used here.

Similar to SS, *unconsolidated sediments* (SU+) in the Japan DSi model result in the highest DSi yields per runoff of the compared studies (Figure 13 D). Possible explanations for this include a blending with pyroclastics and easily weatherable young volcanic rocks or a generally younger age with less weathering cycles of Japanese unconsolidated sediments. Additionally, Hartmann et al. (2010) report areas dominated by *unconsolidated sediments* to be covered by high percentages of rice and crops, which could also influence the silicon cycle, as rice contains high percentages of ASi in its biomass (cf.

Ma and Takahashi, 1989). As Bluth and Kump (1994), did not distinguish unconsolidated sediments, here the class *sandstone* is given for comparison. DSi yield for *unconsolidated sediments* in this study is higher than *sandstone* and *shale* in the study of Bluth and Kump (1994), which again hints to that the main difference is the classification of lithology.

DSi yields for *acid volcanic rocks* (VA+) from this study show values corresponding to those from VA of the Japan-DSi model (Figure 13 E). Bluth and Kump (1994) did not distinguish *acid volcanic rocks* as single lithological class in their study.

For *acid plutonic rocks* (PA), our study shows by far the smallest DSi yields of the compared studies (Figure 13 F). The Japan-DSi model once more results in the highest DSi yields of the three. As with SS, small pyroclastic ash layers would enhance DSi mobilization significantly without being incorporated in the lithological map. Besides, tectonic activity in Japan could increase the availability of fresh mineral surfaces and thus also increase the weathering rates of Japanese PA. The high DSi yields of granite proposed by Bluth and Kump (1994) could be caused by their combination of *granite* and gneiss catchments in the lithological class *granite*. If the gneiss was contaminated with other metamorphic rocks, which are shown to potentially yield far more DSi than granite, this would explain the difference between their results and ours.

That the results of this study fall in the same range as those of previous studies underscores the general applicability of our approach. Strong similarities exist for some lithological classes of the different studies, especially for VA+ and SC. However, DSi yields from other lithological classes vary widely, depending on what model is applied. This comparison underscores the importance of employing detailed lithology data and considering regional differences for DSi mobilization modeling.

3.4.3   Model limitations

Direct human impact on DSi fluxes, which could be caused by industrial sites or sewage waters (Clark et al., 1992; Sferratore et al., 2006), is ignored here but still might affect observed DSi fluxes. Sferratore et al. (2006) suggested a direct DSi input of 1 g per capita and day for the Seine basin. The area assessed here exhibits an average population of 131 capita per km^2. Using 1 g DSi per capita and day as an approximation, an average of 0.048 t SiO_2 km^{-2} a^{-1} would be added from direct human impacts. This amounts to 2.7 % of the average total DSi flux in the assessed area and shows that direct anthropogenic influence on observed DSi flux is small compared to natural sources. However, indirect anthropogenic effects on DSi fluxes (e.g. land cover, land form and riverbed alterations) are difficult to quantify, but can be expected to be nearly ubiquitous. Crop harvesting and grazing potentially reduce DSi fluxes into the fluvial system. It leads to an export of DSi from the catchment

area, as certain crops contain significant amounts of silicon (e.g. Epstein, 1994; Street-Perrott and Barker, 2008).

Another possible error source is the neglect of atmospheric DSi input in this study. Few studies on atmospheric DSi in the conterminous USA are known to the authors, which suggest that atmospheric DSi inputs are very small (Miller and Drever, 1977; Dahlgren et al., 1999; Blecker et al., 2006). However, it is still possible that regionally and seasonally atmospheric DSi inputs are significant (Hartmann et al., 2008; Neff et al., 2008). Additionally, significant amounts of particulate silicon could be introduced by dust deposition that might blur the DSi mobilization results of single lithological classes, as chemical weathering of dust could increase fluvial DSi exports from the catchments (Chadwick et al., 1999; Porder et al., 2007).

Blurring of the model predictors can also originate from dissolution of biogenic ASi from terrestrial systems that has been shown in the laboratory by Fraysse et al. (2009). However, much of this DSi can be expected to be recycled within the ecosystem (Alexandre et al., 1997). Furthermore, significant amounts of ASi are exported from the terrestrial system (Up to 20% of total silica river load: Triplett et al., 2008). For larger catchments and lakes with long residence times, dissolution of ASi in the fluvial system can be important for DSi availability (Schelske and Stoermer, 1971; Schelske, 1985; Bootsma et al., 2003; Heinen and McManus, 2004). However, Triplett et al. (2008) show that for two small catchments in the Mississippi basin comparable to those used in this study, dissolution of ASi from terrestrial phytolites in the fluvial system is minor.

The damming of rivers increases Si retention in the fluvial system (Humborg et al., 1997; Sferratore et al., 2008), while river channel straightening increases flow velocity and thus decreases retention. Eutrophication also greatly affects the biogeochemical Si cycle (cf. Conley, 2002). Although the assessed catchments have been selected for minimal water-body influence, retention will probably affect the results. The average aerial proportion of water bodies (a land-cover class from GLOBCOVER; includes glaciers) per catchment is 0.26 %. The 90th percentile is 0.76 % and the maximum is 5 % – one large lake at a remote position of the catchment.

Our model uses a steady-state point of view, assuming the catchment attributes to be constant with time (Stallard, 1995). For the timeframe observed, this is reliably true for physical parameters like gradient of slope and catchment size. However, other parameters like runoff, observed DSi yield itself, and land cover can be affected by temporal variations. Although GRDC-runoff represents long-term averages, actual runoff affects observed DSi yield via concentration effects. Most monitoring stations cover only one or two years of data (with a maximum of nine years). Although a long-term trend in the observed timeframe is neither observed in our data nor in other studies (Goolsby et al.,

50

1999), interannual fluctuations in DSi yields are high. These fluctuations are buffered by 313 annual datasets (contained in the 142 catchment mean values) for the model as a whole, but can increase residuals of single monitoring stations. Changes in land cover could also add noise to the model because the internal cycling of Si within terrestrial ecosystems is significant compared to the export of DSi to continental aquatic systems and ecosystem disturbances can lead to strong variations in DSi export (Epstein, 1999; Conley, 2002; Balogh-Brunstad et al., 2008; Conley et al., 2008; Saccone et al., 2008; Street-Perrott and Barker, 2008; Struyf and Conley, 2009). Future models using data with higher resolution, both spatial and temporal, may help to further improve the model approach presented here.

3.5   Conclusions from the DSi-model

Our results emphasize the benefit from applying detailed lithological maps and a multilithological approach for modeling DSi mobilization by chemical weathering. The here presented model uses runoff and lithology as major predictors for DSi mobilization in the conterminous USA. The developed model could be applied spatially explicit as one part of a future integrated fluvial DSi flux model, including in-stream processes like retention.

Analysis of lithology effects on DSi mobilization shows that the highest DSi yield per runoff is mobilized from basic igneous lithological classes, followed by *acid volcanic rocks*, *unconsolidated sediments*, *metamorphic rocks*, consolidated sediments (In order of decreasing carbonate content), and *acid plutonic rocks*. Thus, carbonate-rich lithological classes should be considered an important contributor to DSi fluxes. Comparison to other studies (Bluth and Kump, 1994; Hartmann et al., 2010) demonstrates large regional variations in model predictor characteristics. To adequately represent global DSi fluxes, future models need to take those variations into account and be calibrated on different world regions.

Evaluating the model, evidence for temperature and vegetation influence on DSi mobilization is provided. Models using a larger catchment database for calibration and improved soil or land cover data are required to integrate lithology as ultimate source for bioavailable DSi and the complex terrestrial biological silicon cycle. Thus, robust quantitative DSi mobilization models for significant predictions of future DSi supply into aqueous systems could be achieved.

4 CO_2 consumption by chemical weathering in North America

4.1 Introduction

Atmospheric CO_2 concentration has long been hypothesized to be among the key factors controlling Earth's climate (Arrhenius, 1896; Broecker, 1982; Pisias and Shackleton, 1984). This hypothesis was supported by ice core data (Genthon et al., 1987; Raynaud et al., 1993) and is by now widely accepted (cf. IPCC, 2007). On geological timescales, chemical weathering of silicate minerals is one of the major controls on atmospheric/soil CO_2 concentration (pCO_2) (Kempe, 1979; Zeebe and Caldeira, 2008; Pagani et al., 2009). Cations resulting from chemical weathering of silicate and carbonate minerals can be counterbalanced by bicarbonate (HCO_3^-) or carbonate (CO_3^{2-}), both originating from atmospheric CO_2, in aqueous solution (e.g. Garrels and Mackenzie, 1967; Holland, 1978). However, the weathering educt, i.e., silicate or carbonate minerals, is relevant for the proportion of atmospheric/soil CO_2 on HCO_3^- fluxes. Detailed knowledge of large scale chemical weathering parameters is important to accurately model past atmospheric pCO_2 as well as the longer term impact of anthropogenic CO_2 emissions on atmospheric pCO_2 (Lenton and Britton, 2006; Uchikawa and Zeebe, 2008).

Two methods are generally applied to model global CO_2 consumption by chemical weathering (CO_2 consumption is used here as: the transformation of atmospheric/soil CO_2 into dissolved HCO_3^- counterbalanced by cations released from chemical weathering). Models using the "reverse method" identify rock weathering products in river chemistry using assumed chemical end-members (cf. Garrels and Mackenzie, 1967; Gaillardet et al., 1999; Roy et al., 1999; Velbel and Price, 2007). Forward models for CO_2-consumption rates identify significant relations between measured HCO_3^- fluxes induced by rock weathering and predictors representing assumed controlling factors of HCO_3^- flux and associated CO_2 consumption (Amiotte-Suchet and Probst, 1995; Hartmann, 2009). The latter models statistically relate catchment attributes of numerous monitoring stations to model HCO_3^- flux in their water chemistry data. Runoff and lithology are the main attributes ("predictors") they use (Amiotte-Suchet and Probst, 1995; Hartmann, 2009). Hartmann (2009) additionally used the equivalent ratio of HCO_3^- to the sum of Cl^- and SO_4^{2-} as predictor. Temperature has been identified as factor on HCO_3^- fluxes for basaltic catchments (Dessert et al., 2003). The GEMS-CO2 model (Amiotte-Suchet and Probst, 1995) results in an average annual CO_2-consumption of 258 10^6 t C a^{-1}, Hartmann et al. (2009) report 237 10^6 t C a^{-1}, and the reverse model of Gaillardet et al. (1999) results in 288 10^6 t C a^{-1} consumed by chemical weathering.

However, studies assessing in detail a smaller number of catchments additionally suggest, e.g., land cover (Moulton et al., 2000 for forest on basalt; Barnes and Raymond, 2009 for urban and

agricultural on mixed lithologies) and temperature (Dessert et al., 2003 for basalt; Riebe et al., 2004 for granite; Gislason et al., 2009 for basalt) as potential controlling factors of chemical weathering rates and thus CO_2 consumption. From laboratory studies additionally a pH-dependence of mineral dissolution is known (e.g. Schnoor, 1990) which also could influence CO_2 consumption on larger scales. Although these controlling factors may be represented by the predictors of existing CO_2-consumption models, they were not yet explicitly included. Both existing global forward models are calibrated on regional datasets from France (Meybeck, 1986; Amiotte-Suchet and Probst, 1995) or Japan (Hartmann, 2009), and extrapolated worldwide. However, it was not tested whether those datasets also represent worldwide fluxes appropriately. Furthermore, both models are calibrated in areas dominated by forests (Meybeck, 1986; Hartmann, 2009) which might lead to a model bias, assuming an effect of different land cover types on CO_2 consumption by chemical weathering. Moreover, considering the importance of high yielding areas for global CO_2 consumption by chemical weathering it is important to resolve those areas spatially (Hartmann et al., 2009). The newly available lithological map of North America allows an improved resolution compared to the existing CO_2 consumption models.

In the presented study, two "forward method" CO_2 consumption models calibrated on 338 catchments from North America are presented. The catchments are selected for data quality and small anthropogenic impact. One presented model uses runoff and lithology as predictors, the second additionally uses land cover. High resolution geodata and a multilithological modeling approach (cf. Hartmann et al., 2010) are applied for calibration of the models. Data are corrected for atmospheric input, non-weathering terrestrial inputs (e.g. road salt) and carbonate contribution to calculate CO_2 consumption. Potential errors of these corrections are discussed. A detailed assessment of the contribution of carbonate adds detail to the knowledge of the soil/atmospheric CO_2 contribution to HCO_3^- flux in rivers. The developed models are compared to two previous global models of CO_2 consumption (Amiotte-Suchet and Probst, 1995; Hartmann et al., 2009) to identify differences and assess their representativeness for the calibration catchments of this study. Finally, the developed models are extrapolated to North America for spatially explicit calculation of the amount of CO_2 consumed by chemical weathering on that continent.

4.2 Methods and data

The methodology applied for modeling HCO_3^- yields (i.e. HCO_3^- flux per area induced by chemical weathering) is similar to that of the DSi model presented in chapter 3. River chemistry monitoring stations are selected, their catchments delineated, the catchment attributes calculated, and multilithological model equations calibrated.

However, determining the proportion of CO_2 on HCO_3^- fluxes requires several additional corrections and modeling steps (cf. Hartmann, 2009). While HCO_3^- in rivers resulting from silicate mineral weathering is entirely of atmospheric/soil origin, at least half of the HCO_3^- from carbonate mineral weathering originates from the mineral itself. Thus, to consider the proportion of atmospheric/soil CO_2 on fluvial HCO_3^-, it is necessary to quantify the relation between carbonate and silicate mineral weathering induced HCO_3^- flux in the catchments. Even in catchments draining silicate dominated lithological classes, carbonate can contribute significantly to cation flux (e.g. Mast et al., 1990) or HCO_3^- flux (cf. White et al., 1999b; Hartmann, 2009). The proportion of carbonate weathering needs to be identified and corrected also in the HCO_3^- fluxes from non-carbonate lithologies.

Following the description of the data generation process (in chapter 4.2.1), the models for HCO_3^- yield will be described (Chapter 4.2.2). Furthermore, the calculation of CO_2 proportion on HCO_3^- fluxes will be described, which is done per lithology by comparing source rock Ca/Na ratios with mobilized Ca/Na ratios (Chapter 4.2.3). The therefore necessary calculation of source rock Ca/Na ratios is described in chapter 4.2.3.1. The models to determine the mobilization of sodium and calcium per lithology, as well as a comparable HCO_3^- model only employed for calculation of CO_2/HCO_3^- ratios, are described in chapter 4.2.3.2. Only terrigenous, bicarbonate balanced calcium (Ca_{hco3}) and silicate weathering derived sodium (Na_{sil}) should be considered in calculations for CO_2/HCO_3^- ratios. Thus, atmospheric input (Described in chapter 4.2.3.2.1), non HCO_3^- balanced Ca^{2+} (Chapter 4.2.3.2.1), and non silicate weathering derived Na^+ (Chapter 4.2.3.2.2) are corrected for.

4.2.1 Data treatment and catchment definition

Calibration of the here presented model demands an extensive dataset of river chemistry monitoring stations and their catchment attributes. Selection of monitoring stations, calculation of their catchment properties and treatment of the applied data are described in this chapter.

4.2.1.1 Catchment definition

Hydrochemical data were selected from monitoring stations of the U.S. networks NAWQA and WQN and the Canadian ENVIRODAT database (Alexander et al., 1996; Environment Canada Pacific and Yukon Water Quality Monitoring and Surveillance Division, 2008; USGS, 2008b; Government of Alberta, 2009). From the >4500 stations in the combined database, 824 provide measurements for all major elements for at least 12 consecutive months. Those were included in the study database. The positions of the stations were adapted to the stream network derived from the applied digital elevation model (HydroSheds: Lehner et al., 2008). 41 stations could not distinctly be positioned on the HydroSheds-derived river network. For the remaining stations, catchments were delineated using ArcGIS functionality. If the catchment extend was obscured by artificial waterways (33 catchments) or anthropogenic impact was too dominant (e.g. station within a city, 47 catchments), those

monitoring stations, too, were discarded. Of the remaining monitoring stations covering one river basin, only those closest to the headwaters were considered (n=348), thus omitting overlapping catchments and further reducing influence of in-river processes. In 10 of those stations, HCO_3^- exceeds the amount of cations; they were omitted for methodical reasons (cf. Hartmann, 2009). The remaining 338 catchments were used for modeling and analyses in this study. Although the applied criteria do not fulfill the strict requirements stated by Velbel and Price (2007) they are nonetheless stricter than those of most comparable datasets (e.g. Meybeck, 1986) and the large number of assessed catchments is expected to add significance compared to single-catchment mass balances.
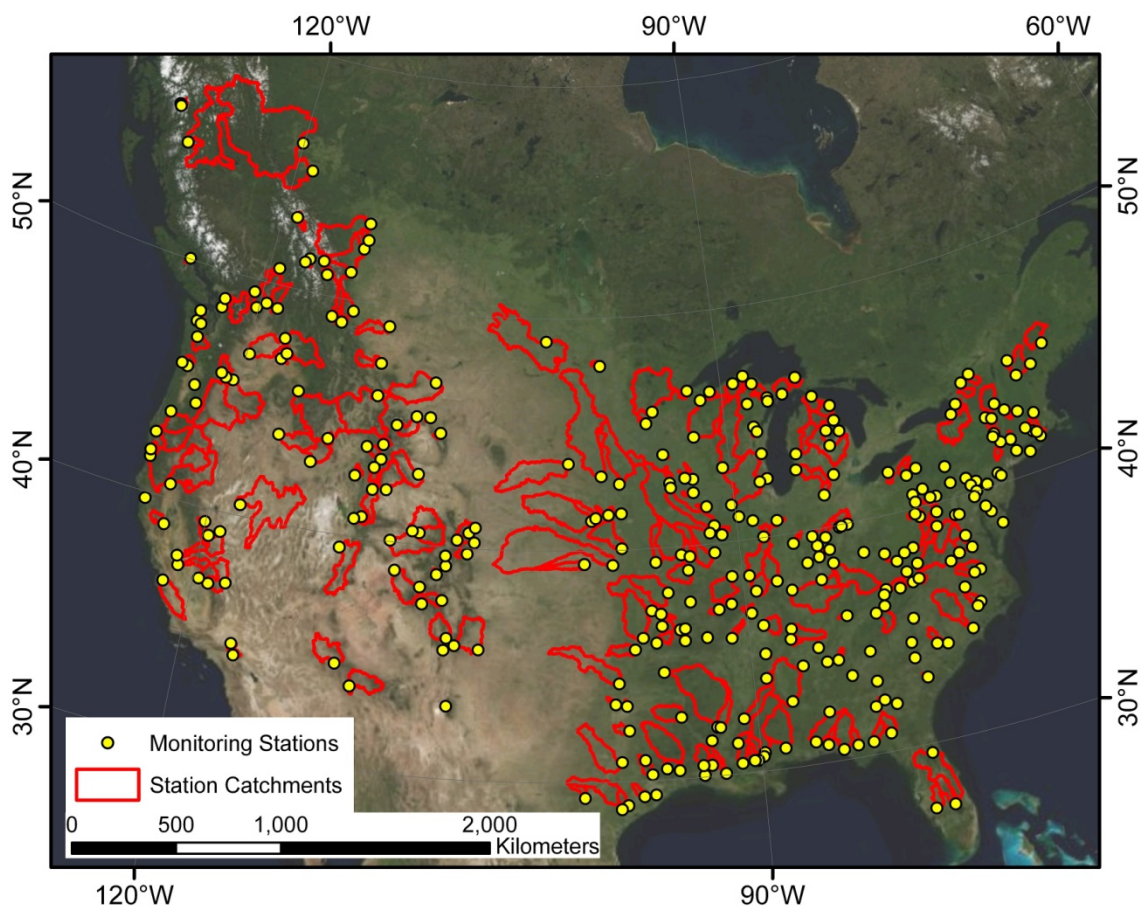
Figure 14: Monitoring stations and their catchments on a satellite image of North America (©2009 Microsoft Corporation). Small catchments may be completely covered by the dot representing the monitoring station.

4.2.1.2 Hydrochemical and spatial data treatment

Monthly HCO_3^- yield is calculated from monthly GRDC-runoff (Fekete et al., 2000) and the corresponding monthly alkalinity value in the measured hydrochemical dataset. Long-term GRDC-data are employed because interannual runoff fluctuations are high and on large scales only a small number of rivers show long-term runoff trends in the U.S. (Dai et al., 2009). Alkalinity is assumed to represent HCO_3^- adequately, because only little influence of other buffering ions is expected. Annual

HCO₃- yield, which is used for further calculations, is calculated as the sum of monthly yields (Equation 4).

Equation 4) $f_{X,j} = \sum_{1}^{n=12} c_{j,x,n} \cdot q_{j,n}$

Equation 4: The annual yield (f) of each element (x) per catchment (j) is calculated by summing up the product of concentration (c) of that element and runoff (q) for each month (n).

Contrary to multiplying annual runoff with annual average concentration, summing up monthly yields introduces discharge weighting, representing real fluxes better than annual averages as e.g. suggested for dissolved DSi by Fulweiler and Nixon (2005). Up to three different datasets for runoff were available for some monitoring stations. GRDC-runoff is a spatial dataset calibrated on long-term data (Fekete et al., 2002), instant discharge was measured when taking the sample for chemical analysis and daily discharge is measured continuously. Discharges ($m^3 s^{-1}$) are recalculated to runoff ($L m^{-2} a^{-1}$) by dividing by catchment area and multiplying by a correction factor for unit adjustment. A comparison of GRDC-runoff, instant runoff and monthly averaged daily runoff (which is considered the most trustworthy of the three but not available for all monitoring stations) was done for 87 stations, where all three datasets are available. In that dataset, average GRDC-runoff underestimates daily runoff by 15 % while instant discharge overestimates it by 25 %. Another reason to use GRDC-runoff is that, as a spatial dataset, it can later be applied for extrapolation of the model results.

Table 12: Spatial datasets that are applied as source data for catchment attributes in the presented study (and their references).

Catchment attribute	Reference dataset
Runoff	GRDC-runoff (Fekete et al., 2000)
Lithology	Lithological map of North America (Jansen et al., 2010)
Topographic data	Hydrosheds 15" (Lehner et al., 2008)
Climate data other than runoff	WorldClim (Hijmans et al., 2005)
Land Cover	GlobCover (Arino et al., 2007)
Soil-pH, C_{org} and bulk density	SOTER (Batjes, 2006)
Irrigated areas	Global map of irrigated areas (Siebert et al., 2005)
Population density	Gridded population of the world v3 (CIESIN and CIAT, 2005)

To model the weighted yields from the 338 calibration catchments, catchment attributes are calculated applying different spatial datasets (Table 12, appendix A). Some of the lithological classes from the lithological map of North America (Chapter 2; Jansen et al., 2010) were aggregated because they were not adequately represented in the calibration catchments. The lithological classes applied in this study as well as their proportions of the calibration area and North America are given in table 13. The GlobCover data were reclassified for the use in this study, emphasizing the expected weathering influence of land cover classes. Original GlobCover classes and land cover classes considered herein are described in table 14. The original classification of soil parameters from SOTER (Table 15) is left unchanged for calculations in the model presented here.

Table 13: Lithological classes applied in this study, their abbreviations and aerial proportion in North America and in the calibration area of the HCO$_3^-$ models.

Herein used abbreviation	Lithological classes from the Map	Proportion of North America	Proportion of calibration area
SU+	Unconsolidated sediments (SU)	13.43 %	21.40 %
	Dune sands (DS)	0.35 %	0.51 %
	Loess (LO)	0.17 %	0.39 %
	Alluvial deposits (AD)	0.30 %	0.90 %
SS	Siliciclastic sedimentary rocks (SS)	23.64 %	32.41 %
SM	Mixed sedimentary rocks (SM)	14.07 %	11.42 %
SC	Carbonate sedimentary rocks (SC)	10.28 %	11.08 %
MT	Metamorphic rocks (MT)	12.79 %	6.62 %
PB+	Basic plutonic rocks (PB)	0.56 %	0.36 %
	Intermediate plutonic rocks (PI)	1.25 %	0.71 %
PA	Acid plutonic rocks (PA)	12.44 %	4.26 %
VB+	Basic volcanic rocks (VB)	4.00 %	4.98 %
	Pyroclastics (PY)	0.26 %	0.55 %
VA+	Acid volcanic rocks (VA)	1.00 %	1.30 %
	Intermediate volcanic rocks (VI)	1.71 %	3.08 %
WB	Water bodies (WB)	2.46 %	0.37 %
--	Evaporites (EV, not analyzed in this study)	0.26 %	0.02 %
--	Ice and glaciers (IG, not analyzed in this study)	0.40 %	0.00 %

Table 14: The land cover classes used in this study, the corresponding classes of Arino et al. (2007) and their aerial abundance in the area of the here assessed catchments.

Class Number	Class used in this study	Original class name	Proportion of calibration area
LC1	Cultivated land	A11 - cultivated terrestrial areas and managed lands	18.74 %
LC2	Broadleaved forest	A12 - natural and semi-natural terrestrial vegetation - woody / trees / broadleaved	28.88 %
LC3	Needle leaved forest	A12 - natural and semi-natural terrestrial vegetation - woody/ trees / needle-leaved	26.14 %
LC4	Shrubs	A12 - natural and semi-natural terrestrial vegetation - shrubs	5.68 %
LC5	Grasslands	A12 - natural and semi-natural terrestrial vegetation - herbaceous	18.52 %
LC6	Sparse	A12 - natural and semi-natural terrestrial vegetation	0.00 %
LC7	Aquatic vegetation	A24 - natural and semi-natural aquatic vegetation	0.18 %
LC8	Artificial surfaces	B15 - artificial surfaces and associated areas - urban > 50 %	0.11 %
LC9	Bare areas	B15 - artificial surfaces and associated areas - bare areas	0.02 %
LC10	Water and ice	B28 - inland water bodies	1.46 %

Table 15: SOTER soil data classification (Batjes, 2006)

Class	pH	C_{org} [g C kg^{-1}]	Bulk density [kg dm^{-3}]
1	< 4.5	< 5	0.1 - 0.4
2	4.5 - 5.5	5 – 10	0.4 - 0.9
3	5.5 - 6.5	10 – 20	0.9 - 1.2
4	6.5 - 7.3	20 - 100	1.2 - 1.4
5	7.3 - 8.5	> 100	1.4 - 1.6
6	n.a.	n.a.	> 1.6

4.2.2 HCO$_3^-$ yield modeling

The first step of modeling CO_2 consumption by chemical weathering is to model HCO$_3^-$ yield in the assessed catchments. In later steps, the proportion of CO_2 consumption per mol of the modeled HCO$_3^-$ will be determined. Multilithological nonlinear model equations were set up, extended from those introduced for HCO$_3^-$ modeling by Hartmann (2009). The models predict HCO$_3^-$ yields using catchment attributes as predictors and statistically derived b-parameters. The Levenberg-Marquardt least square algorithm (implemented in the software Statistica 8) was applied to fit b-parameters of the model equations. Model predictors were chosen to represent controlling factors of chemical weathering rates and HCO$_3^-$ mobilization known from literature. In an iterative process, residuals for individual model realizations were analyzed for trends with potential controlling factors in scatter plot-analysis. It was tried to implement those showing significant trends into new models, using ad-hoc process assumptions based on a review of existing literature.

The resulting model was compared to existing global flux models covering the North American continent but calibrated on datasets from other regions (Amiotte-Suchet et al., 2003; Hartmann et al., 2009). Furthermore, it was extrapolated to the area of North America using the spatial input datasets and ArcGIS 9.3 functionality. ArcGIS was also employed for all other spatial related calculations in this study. The extrapolated model was checked for plausibility using available measured data.

4.2.3 Calculation of atmospheric/soil CO$_2$ contribution to fluvial HCO$_3^-$ fluxes

To determine the contribution of atmospheric/soil CO_2 on fluvial HCO$_3^-$ fluxes it is necessary to distinguish between carbonate and silicate weathering. For carbonate weathering counterbalanced by atmospheric/soil CO_2 that contribution is 50 %, while silicate weathering derived dissolved HCO$_3^-$ stems entirely from atmosphere/soil CO_2. Modeled contributions from carbonate-rich lithological classes (SM, SC) to fluvial HCO$_3^-$ flux are treated as completely carbonate weathering derived. The associated CO_2/HCO$_3^-$ ratio was manually set to 50 %. However, distinguishing lithological classes is not sufficient to differentiate between carbonate and silicate weathering, because in silicate rock

dominated classes carbonates may also contribute significantly to HCO_3^- fluxes (cf. White et al., 1999b; Hartmann, 2009).

For silicate dominated lithological classes the CO_2/HCO_3^- ratio was calculated following the method of Hartmann (2009). HCO_3^- counterbalanced terrigenous dissolved calcium (Ca_{hco3}) exceeding the source rock Ca/Na elemental ratio was called "excess calcium". Excess-calcium does not have a strictly defined source. It may origin from primary or secondary trace calcite in plutonic rocks, carbonate cement in sediments or even contributions of an unmapped carbonate rock unit within a non-carbonate lithological class. However, all excess-calcium is attributed to carbonate weathering. It is reasonable to assume a higher Ca-mobilization as reason for the excess rather than a decrease of sodium. The existence of a sodium sink in catchments other than evaporite precipitation is unlikely (Bowser and Jones, 2002), and evaporite precipitation is not expected in the calibrating area. Ca/Na ratios are given in mol/mol unless otherwise stated.

The ratio of silicate-calcium to total calcium (Ca_{sil}/Ca_{hco3}) was determined per lithological class by dividing the Ca/Na average elemental ratio in source rocks by the Ca/Na ratios in the water (Equation 5). Excess-calcium was calculated as the proportion of HCO_3^- counterbalanced terrigenous calcium (Ca_{hoc3}) that exceeds the Ca_{sil} proportion (Equation 6). Atmospheric/soil CO_2 proportion per mol HCO_3^- was calculated by subtracting the average excess-calcium per lithological class from average HCO_3^- flux per lithological class and dividing by HCO_3^--flux of that class (Equation 7). Thus, for each mol excess-calcium one mol HCO_3^-, which is expected to originate from the lithosphere, was subtracted.

$$\text{Equation 5)} \quad \frac{Ca_{sil,L}}{Ca_{hco3,L}} = \frac{\frac{Ca_{sil,rock,L}}{Na_{sil,Rock,L}}}{\frac{Ca_{hco3,L}}{Na_{sil,L}}}$$

Equation 5: The ratio of silicate weathering derived calcium (Ca_{sil}) to the total HCO_3-counterbalanced terrigenous calcium (Ca_{hco3}) is calculated from the division of Ca/Na ratios in source rock ($Ca_{sil, rock}/Na_{sil, rock}$, compare chapter 4.2.3.1) and the ratio of Ca_{hco3} on silicate weathering derived sodium mobilization from each lithological class L (Ca_{hco3}/Na_{sil}, compare chapter 4.2.3.2). Because sodium is assumed to be conservative in the catchment, $Na_{sil,Rock}$ per lithological class (L) and Na_{sil} per lithological class are considered the same. All units are mol.

Equation 6) $f_{Ca_{Ex,L}} = f_{Ca_{hco3,L}} \cdot (1 - \frac{Ca_{sil,L}}{Ca_{hco3,L}})$

Equation 6: The "excess calcium"-yield ($f_{Ca, Ex}$, attributed to weathering of carbonate) is calculated by multiplying the HCO_3^- counterbalanced terrigenous calcium yield ($f_{Ca, hco3}$) with 1 minus the proportion of Ca_{sil} per Ca_{hco3} for each lithological class (L). All units are mol.

Equation 7) $\frac{F_{CO_2,L}}{F_{hco3,L}} = \frac{F_{hco3,L} - F_{Ca_{Ex,L}}}{F_{hco3,L}}$

Equation 7: CO_2 consumption per lithological class (F_{CO2}) is calculated per lithology (L) by subtracting excess-calcium ($F_{Ca, Ex}$) from modeled HCO_3^- flux (F_{hco3}). The equation is then divided by modeled HCO_3^- flux ($F_{hco3, L}$). All units are mol.

Contributions of individual lithological classes to the fluxes of Ca_{hco3} and Na_{sil} were calculated using models (Chapter 4.2.3.2). The corrections necessary to calculate HCO_3^- counterbalanced terrigenous calcium (Ca_{hco3}) and silicate weathering derived sodium (Na_{sil}) will be described in the chapters 4.2.3.2.1, 4.2.3.2.2 and 4.2.3.2.3. The applied rock Ca/Na ratios will be described in chapter 4.2.3.1. To calculate the CO_2/HCO_3^- ratio a HCO_3^- flux model of similar structure as the models for Na_{sil} and Ca_{hco3} is used for consistency (Chapter 4.2.3.2).

4.2.3.1 Ca/Na elemental ratios in source rocks

Ca/Na elemental ratios in the weathering source rocks were derived from geochemical databases. The here applied dataset consists of data from the U.S. National Geochemical Database (USGS, 2008a) and the unconsolidated sediment part of the PLUTO database (USGS, 2001). It contains chemical analyses of 414 321 rock samples. Based on the given rock type, a lithological unit (corresponding to the lithological map, chapter 2) was assigned to each sample. To minimize influence of single, extreme values, only the 10th to 90th percentile Ca/Na elemental ratios of the samples of each lithological class were considered for interpolation to North America. The considered sample point Ca/Na elemental ratios of each lithological class were interpolated to the area of North America using inverse distance weighting with a power of 2 (ArcGIS "Spatial Analyst"-functionality). From the interpolated data, areas of the respective lithological classes were clipped. From the values of those areas, the average Ca/Na elemental ratio per catchment and lithological class were calculated.

Not for all lithological classes an adequate number of samples were available. Therefore, the interpolations for *alluvial deposits* (AD) and *dune sands* (DS) were done using the samples classified as *unconsolidated sediments* (SU). The interpolation of elemental ratios for *loess* (LO) was done using the 10723 samples classified as SU plus 23 samples classified as LO (compare also table 13 for lithologic units). Similarly, the interpolation for *mixed sedimentary rocks* (SM), a class defined as assembled of carbonate and siliciclastic sediments, was done using samples classified as *carbonate*

sedimentary rocks (SC) or *siliciclastic sedimentary rocks* (SS) plus 14 samples classified as SM. Some igneous samples were not differentiated as plutonic rocks or volcanic rocks. Those, only classified as acid, intermediate or basic, were considered for interpolation of both the respective volcanic and plutonic lithological classes.

4.2.3.2 Models to calculate carbonate contribution to HCO$_3^-$ fluxes per lithological class

To determine the ratio of mobilized Na$_{sil}$/Ca$_{hco3}$ per lithological class, fluxes of both elements were modeled as sum of inputs from different lithological classes (Equation 8 A and B). The model setups are similar to other multilithological models applied here and in previous studies (Hartmann, 2009; Hartmann et al., 2010; Jansen et al., 2010).

$$\text{Equation 8 A) } F_{Na_{sil},j,L} = q_j \cdot c_{Na,j} \cdot \sum_1^L (A_{L,j} \cdot \frac{b_{Na,L}}{1000}) \frac{Observed_{Na_{sil},j}}{Predicted_{Na_{sil},j}}$$

$$\text{Equation 8 B) } F_{Ca_{hco3},j,L} = q_j \cdot c_{Ca,j} \cdot \sum_1^L (A_{L,j} \cdot \frac{b_{Ca,L}}{1000}) \frac{Observed_{Ca_{hco3},j}}{Predicted_{Ca_{hco3},j}}$$

Equation 8: The model equations calculate fluxes of A) Na$_{sil}$ and B) Ca$_{hco3}$ for each catchment (j) and considered lithological class (L), using GRDC-runoff (q) and measured concentration (c) of the respective ion (Ca or Na) in the catchments, the aerial proportion of each considered lithological class (A) of the entire catchment and a factor (b) per lithological class. The division by 1000 adjusts the magnitude of the b-parameters to reduce round-off errors. The correction factor (observed/predicted) is not part of the model but is applied afterwards to counteract model errors.

The correction factor (observed/predicted) was used to reduce errors of the model (cf. Hartmann, 2009); it ensured that the result of the sum of the Ca$_{hco3}$ or Na$_{sil}$ contributions from all lithological classes was equal to the observed values. The factor was applied, because the goal of these models was only to attribute fluxes of Ca$_{hco3}$ and Na$_{sil}$ to individual lithological classes, not to extrapolate or predict these fluxes. Use of the correction factor, of course, led to an equal share of all lithological classes on the model error.

However, prior to modeling corrections were needed to transform discharge-weighted total fluxes in the catchments to silicate weathering derived sodium (Na$_{sil}$) and carbonate counterbalanced terrigenous calcium (Ca$_{hco3}$). The dissolved elements in the water were corrected for atmospheric inputs (Chapter 4.2.3.2.1), for non-silicate terrigenous sodium inputs (Chapter 4.2.3.2.2), and for non-HCO$_3^-$ counterbalanced calcium (Chapter 4.2.3.2.3). Fluxes of all considered ions (Ca^{2+}, Na$^+$, HCO$_3^-$, Cl$^-$, and SO4^{2-}) needed to be positive in a catchment after the corrections for that catchment to be included into the Ca$_{hco3}$ and Na$_{sil}$ models. In order to yield significant b-parameters for each lithological class, *acid plutonic rocks* (PA) and *metamorphic rocks* (MT) as well as basic igneous rocks (VB+ and PB+) had to be combined for calculation of Ca/Na elemental ratios. Those classes are in further called MTPA and VBPB, respectively. Of the model results, only the average modeled

Ca$_{hco3}$/Na$_{sil}$ elemental ratios between the 10th and 90th percentile of values were considered for calculation of excess-calcium to reduce the influence of outliers.

To keep input data for calculation of the CO$_2$/HCO$_3^-$ ratio comparable, a model for HCO$_3^-$ flux similar to the models for Na$_{sil}$ and Ca$_{hco3}$ (Equation 8 A and B) was introduced (Equation 9). This model was used for calculation of the proportion of excess-calcium on HCO$_3^-$ flux (Equations 6 and 7). It also uses the combined lithological class MTPA. The b-parameters of all models described in this chapter are given in appendix C

$$\text{Equation 9) } F_{HCO3,j} = b_0 \cdot \sum_1^L A_{L,j} \cdot q_j{}^{b_L} \cdot \frac{Observed_{HCO3,j}}{Predicted_{HCO3,j}}$$

Equation 9: HCO$_3^-$ flux model using only runoff (q) and aerial proportion of lithology classes (A$_L$) as predictors and thus comparable to the models for Na$_{sil}$ and Ca$_{hco3}$ (Equation 8). The correction factor (observed/predicted), which is not part of the model but applied afterward to counterbalance the model error, is explained in the text.

4.2.3.2.1 Correction of atmospheric inputs

As only elementary ratios from chemical weathering should be used for excess-calcium calculation, dissolved major elements in rivers were corrected for atmospheric inputs. Other studies used chloride normalization to calibrate atmospheric inputs for concentration and evaporation effects, using a catchment that is representative for the study area and not affected by other Cl$^-$ sources than atmosphere (e.g. Han and Huh, 2009). For the presented study it was not possible to identify catchments that lack Cl$^-$ sources other than the atmosphere and that could be interpreted as being representative for all other catchments' regional settings. Thus, similar to Roy et al. (1999), non-chloride normalized elementary fluxes from precipitation were used to quantify atmospheric fluxes. Atmospheric inputs for the ions Na$^+$, K$^+$, Ca^{2+}, Mg^{2+}, Cl$^-$, NO$_3^-$ and SO$_4^{2-}$ were calculated using maps generated from precipitation chemistry data from 129 monitoring stations in Canada (Meteorological Service of Canada, 2008), 8 stations in non-conterminous U.S. territories (NADP, 2008a) and existing precipitation chemistry maps for the conterminous U.S. (NADP, 2008b). Atmospheric input per element was calculated as product of concentration maps and annual precipitation (Hijmans et al., 2005). Atmospheric inputs are subtracted from river elementary fluxes (Equation 10). A detailed description of the atmospheric input maps is given in appendix B.

$$\text{Equation 10) } F_{terr,x,j} = F_{riv,x,j} - F_{atm,x,j}$$

Equation 10: Correction of atmospheric inputs: Terrestrial Flux (F$_{terr}$) is discharge-weighted measured river flux (F$_{riv}$) minus atmospheric inputs (F$_{atm}$) for each considered element (x) in each catchment (j).

In 8 catchments, GRDC-runoff exceeded average annual precipitation from the worldclim data. To correct for the effects of this unlikely case all atmospheric inputs in those catchments were reduced

with a correction factor annual precipitation/GRDC-runoff. In 9 catchments, chloride inputs from precipitation exceeded the calculated fluvial outputs from the catchments. This could be explained with active evaporite formation in arid catchments, which is not assumed within our study area. Thus, in the cases were Cl^- input exceeds Cl^- output, all precipitation inputs were reduced by a factor Cl_{output}/Cl_{input}.

Significant temporal trends of precipitation dissolved ion concentrations or precipitation quantity might lead to a biased atmospheric input correction. For different stations in eastern North America a decrease in base cations was shown on data from 1979-90 (Hedin et al., 1994). Furthermore, a 20 % decrease of calcium deposition was reported for a catchment in Ontario in the time from 1983 to 1998 (Watmough and Dillon, 2004). However, no general trends were observed in the here applied precipitation chemistry maps (NADP, 2008b), which provide data for the period between 1994 and 2006.

4.2.3.2.2 Correction of non-silicate sodium

Following atmospheric correction, sodium is assumed to enter a catchment by weathering of silicates and evaporite rocks as well as from anthropogenic sources. The silicate weathering derived proportion is assumed to be counterbalanced dominantly by bicarbonate while the evaporite and anthropogenic fractions would be counterbalanced by chloride. Correction for non-silicate derived sodium is done using Na/Cl elemental ratios in the water.

However, defining the Na/Cl elemental ratios for correction is difficult due to their large variability. Halite weathering would leave a Na/Cl elemental ratio of 1:1; while the sea-salt derived Na/Cl elemental ratio (although sea salt should already be corrected for) is between 0.862 and 0.855 (Keene et al., 1986). Moreover, the most variable Na/Cl inputs are expected from anthropogenic sources. For urban sewage, Na/Cl elemental ratios of ~1.25 (Roy et al., 1999), 1.08 or 0.68 (Grosbois et al., 2001) were published. Road salting is defined by a Na/Cl elemental ratio 1, assuming a theoretical halite composition. However, because of up to 20 mass-% applied $CaCl_2$ for salting (e.g. Bowser and Jones, 2002; Szramek and Walter, 2004; Rosfjord et al., 2007) and cation exchange in soils, which can release calcium and magnesium at the expense of sodium in treated areas (Lofgren, 2001; Rosfjord et al., 2007), the actual fluvial Na/Cl signature from road salting is supposedly below 1. Road salting is especially important in the northeastern US, and even influences Cl-concentrations in small, rural streams (Transportation Research Board, 1991; Kaushal et al., 2005). Na/Cl elemental ratios from agriculture vary largely, depending on fertilizer use (Pierson-Wickmann et al., 2009). Roy et al. (1999) report Na/Cl elemental ratios of 0.2 and 0.33 for agricultural inputs in their study areas, while Grosbois et al. (2001) provide elemental ratios of 2.4 and 1.36 for different areas. To extract

the silicate weathering derived sodium, in this study the original terrestrial Na-yields (on average $0.132 \cdot 10^6$ mol Na km^{-2} a^{-1} per catchment) are corrected for terrestrial chloride (Equation 11).

Equation 11) $Na_{sil} = Na_{terr} - Cl_{terr} \cdot R_{Na/Cl}$

Equation 11: Chloride correction: Silicate weathering derived sodium (Na$_{sil}$) is terrestrial sodium (Na$_{terr}$) minus terrestrial chloride (Cl$_{terr}$) times a defined Na/Cl elemental ratio (R$_{Na/Cl}$).

Regarding the likely sources for Na$_{terr}$ or Cl$_{terr}$, three different elemental ratios are used for R$_{Na/Cl}$, creating three "scenarios" of possible chloride or non-silicate sodium sources:

-   R$_{Na/Cl}$ = 1, which is the theoretical mobilization ratio of halite weathering. To correct Na$^+$ for Cl$^-$ using this ratio results in negative Na$_{sil}$ yields for 121 catchments. The 217 catchments with positive Na$_{sil}$ yields, which are considered in further calculations, hold an average yield of $0.0606 \cdot 10^6$ mol Na km^{-2} a^{-1} per catchment.
-   R$_{Na/Cl}$ = 0.858, which is the average value of the Cl/Na elemental ratios for seawater given by Keene et al. (1986) and references therein. This correction ratio leaves 84 catchments with negative Na$_{sil}$ yields. The remaining 254 catchments yield $0.0623 \cdot 10^6$ mol Na km^{-2} a^{-1} on average.
-   R$_{Na/Cl}$ = 0.731, which is the average atmospheric corrected Na$_{terr}$/Cl$_{terr}$ elemental ratio of the here assessed catchments. Correction with this ratio results in 58 catchments with negative Na$_{sil}$ yields and an average Na-yield of $0.685 \cdot 10^6$ mol Na km^{-2} a^{-1} for the remaining catchments (n= 280) with positive Na$_{sil}$ yields.

The three correction scenarios will be named Na$_{Sil1}$, Na$_{Sil0858}$ and Na$_{Sil0731}$ in the following. Catchments yielding negative amounts of Na$_{sil}$ after correction are omitted, because negative Na$_{sil}$ fluxes are interpreted as obviously wrong result of the correction. Thus, the three scenarios have different sample sizes of 217, 254 and 280, respectively.

4.2.3.2.3 Correction of non-bicarbonate counterbalanced calcium

Calcium remaining in rivers after correction for atmospheric inputs was assumed to be counterbalanced by bicarbonate, but also by nitrate and lithogenic sulfate or chloride. A nitrate counterbalanced Ca^{2+} fraction was not considered here, as the nitrate accounts for less than 1 % of the total anions in 78 % of the assessed catchments (mean: 1.6 %; note that in 219 cases, atmospheric inputs were larger than catchment outputs for NO$_3^-$. For those cases, terrestrial NO$_3^-$ was manually set to 0). Thus, although NO$_3^-$ may have large influence on the CO$_2$/HCO$_3^-$ ratio in some regions with large agricultural impact (Perrin et al., 2008), it does not in the assessed catchments. This underscores the small anthropogenic influence on the catchments.

As only the fraction counterbalanced by HCO_3^- consumes atmospheric/soil CO_2, the proportion on Ca^{2+} counterbalanced by SO_4^{2-} and Cl^- were corrected. However, to exactly quantify the extent to which Ca^{2+} is counterbalanced by HCO_3^-, SO_4^{2-} or Cl^- is not feasible. For simplicity, it is assumed that Ca_{terr} is counterbalanced equally by each of those anions according to their equivalent ratios. The HCO_3^- counterbalanced fraction is calculated in two ways, either attributing calcium only to bicarbonate and sulfate or to bicarbonate, non-sodium-counterbalancing chloride and sulfate in equal equivalent-proportions (Equation A and B).

$$\text{Equation 12 A) } F_{Ca,hco3} = F_{Ca,alkso4} = Ca_{terr} \frac{F_{HCO3}}{F_{HCO3} + 2 \cdot F_{SO4}}$$

$$\text{Equation 12 B) } F_{Ca,hco3} = F_{Ca,alkclso4} = Ca_{terr} \frac{F_{HCO3}}{F_{HCO3} + (1-R_{Na/Cl}) \cdot F_{Cl} + 2 \cdot F_{SO4}}$$

Equation 12: Correction for non- HCO_3^- counterbalanced calcium assuming A) that Ca is only counterbalanced by HCO_3^- and SO_4^{2-} and B) that Ca is counterbalanced by HCO_3^-, SO_4^{2-} and the remainder of Cl^- that does not balance sodium (1-$R_{Na/Cl}$). Calculations are done in mol.

The atmospheric input corrected Ca^{2+} yield (Ca_{terr}) is 0.212 10^6 mol Ca km^{-2} a^{-1} per catchment. The correction according to equation 12 A (in the following named Ca_{alkso4}) results into a lower average Ca_{hco3} yield of 0.166 10^6 mol Ca km^{-2} a^{-1} per catchment. Correcting Ca_{terr} according to equation 12 B (in the following named $Ca_{alkclso4}$) results in 0.145 10^6 and 0.155 10^6 mol Ca km^{-2} a^{-1} for the 254 and 280 catchments of the $Na_{sil0858}$ and $Na_{sil0731}$ scenarios, respectively. For the Na_{sil1} scenario, the $Ca_{alkclso4}$ correction was not performed, because all chloride is per definition counterbalanced by sodium in that scenario.

4.3 Results

4.3.1 Bicarbonate yields

The first step towards modeling CO_2 consumption is to establish a model on HCO_3^- yields from chemical weathering. For this model, the 338 stations fulfilling the criteria named in chapter 4.2.1.1 are used. In a second step, the amount of CO_2 consumed per mol HCO_3^- will be calculated. The average HCO_3^- yield from the 338 stations is 0.50 10^6 mol km^{-2} a^{-1}; the minimum yield is 4.16 10^3 mol km^{-2} a^{-1} and the maximum is 2.15 10^6 mol km^{-2} a^{-1} (Figure 15). The entire monitored area of 1.89 10^6 km² yields 0.36 10^6 mol HCO_3^- km^{-2} a^{-1} on average. Larger yields can be observed in general in catchments positioned further north, especially in the northeast, but no clear geographic correlation is identified apart from that.
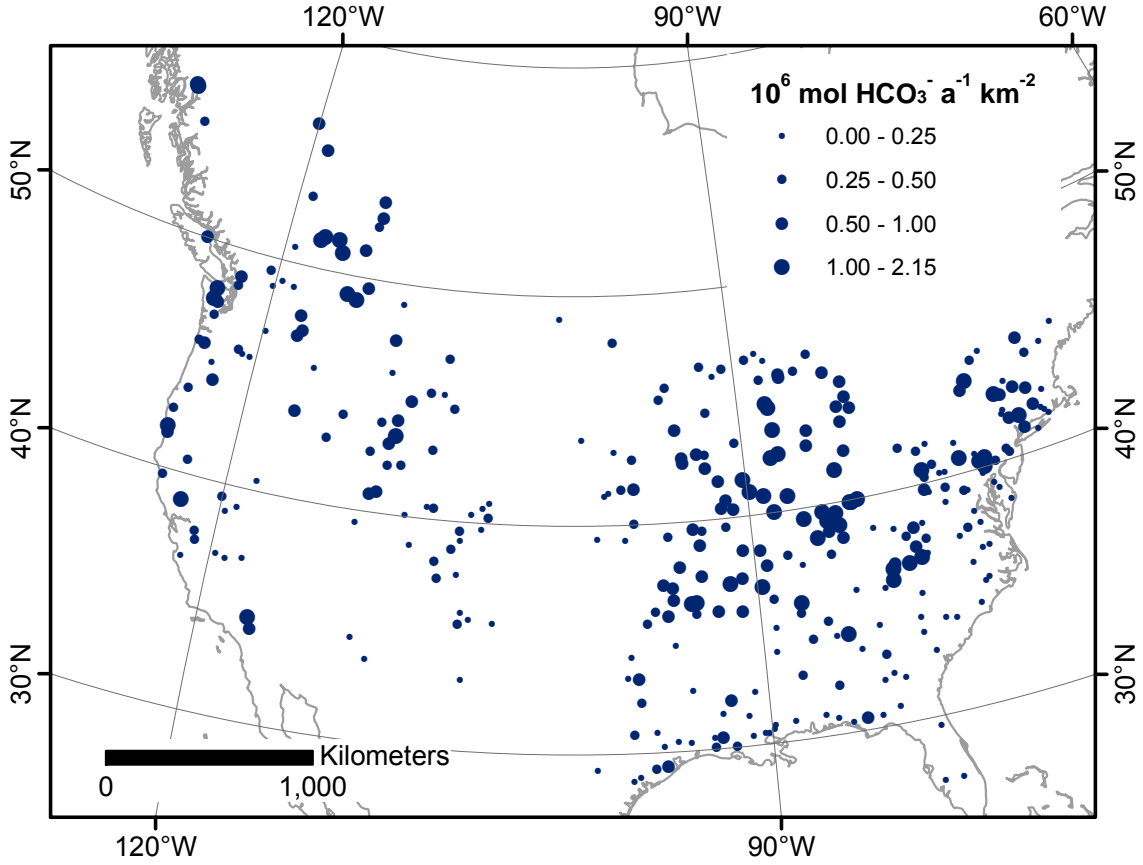
Figure 15: HCO₃- yields of observed monitoring stations. Apart for some tendency for larger HCO$_3$-yields to cluster in the north east could be interpreted, no clear spatial correlation is visible.

Equation 13) $f_{HCO_3^-{}_j} = b_0 \cdot q_j{}^{b_1}$

Equation 13: Bicarbonate yield (10^6 mol HCO$_3^-$ km^{-2} a^{-1}), modeled by runoff only (Ro-model). The parameter q represents the average GRDC-runoff (mm a^{-1}) per catchment j. All b-parameters are estimated model parameters. Values for b-parameters are given in table 16.

Equation 14) $f_{HCO_3^-{}_j} = b_0 \cdot \sum_1^L (A_{L,j} \cdot q_j{}^{b_L})$

Equation 14: Bicarbonate yield (10^6 mol HCO$_3^-$ km^{-2} a^{-1}), modeled by combining runoff and lithology (RoLi-model). The parameter, A$_{L,j}$ represents the aerial proportion of each lithological class (L) in each individual catchment (j).

Equation 15) $f_{HCO_3^-{}_j} = b_0 \cdot \sum_1^L (10^{\left(\frac{b_{pH}}{pH_{SOT,j}}\right)} \cdot (A_{L,j} \cdot q_j{}^{b_L}))$

Equation 15: Bicarbonate yield (10^6 mol HCO$_3^-$ km^{-2} a^{-1}), modeled by combining runoff, lithology and SOTER pH (RoLiPh-model). The factor pH$_{SOT,j}$ represents the average pH class (Compare table 15) of each individual catchment (j).

Equation 16) $F_{HCO_3^-{}_j} = b_0 \cdot \sum_1^L (A_{L,j} \cdot q_j{}^{b_n}) \cdot \left(1 + \sum_n^{1,4,5,8} A_{LC_n,j} \cdot b_{LC_n}\right)$

Equation 16: Bicarbonate yield, modeled by combining runoff, lithology and land cover (RoLiLc-model). The parameter n represents the applied land cover classes LC1 (managed lands), LC4 (shrubs), LC5 (grasslands) and LC8 (urban area); compare table 14 and the accompanying text for details. A$_{LCn,j}$ represents the aerial proportion of each land cover class (n) in the catchment (j).

Table 16: Values for the b-parameters in the equations 13 to 16. All parameters are significant on a 1 % level (pmax=0.006 for b_0 in the Ro-Model). In the three columns on the right side, lithology-related b-parameters are given normalized to the b_{PA} value. Note: The lithology parameters are applied exponentially in the models, thus relative b-parameters should only be used for qualitative interpretations.

	Parameter values				b-Parameter values relative to b_{Pa}		
Parameter	Ro-Model	RoLi-Model	RoLiPh-Model	RoLiLc-Model	RoLi-Model	RoLiPh-Model	RoLiLc-Model
Correlation coefficient	r=0.37	r= 0.80	r=0.83	r= 0.84			
b_0	0.057988	0.01581	0.018619	0.00459			
b_1	0.375899						
b_{SU+}		0.447053	0.522544	0.61178	99.52 %	97.61 %	108.32 %
b_{MT}		0.324101	0.459133	0.52117	72.15 %	85.76 %	92.27 %
b_{PA}		0.449188	0.535364	0.56481	100.00 %	100.00 %	100.00 %
b_{PB+}		0.723692	0.789795	0.86847	161.11 %	147.52 %	153.76 %
b_{SC}		0.745784	0.815543	0.87562	166.03 %	152.33 %	155.03 %
b_{SM}		0.733553	0.790367	0.88747	163.31 %	147.63 %	157.13 %
b_{SS}		0.536626	0.60873	0.70368	119.47 %	113.70 %	124.59 %
b_{VA+}		0.519572	0.576837	0.66095	115.67 %	107.75 %	117.02 %
b_{VB+}		0.483038	0.5486	0.63041	107.54 %	102.47 %	111.61 %
b_{pH}			-0.606014				
b_{LC1} [A]				0.76649			
b_{LC4} [A]				4.91321			
b_{LC5} [A]				1.07698			
b_{LC8} [A]				35.58525			

[A] Land cover classes in the b-parameters are coded as: LC1: *managed lands*, LC4: *shrublands*, LC5: *grasslands* and LC8: *urban areas*.

Using only runoff to model bicarbonate yields (Ro-model) according to equation 13 results in an average yield of 0.41 10^6 mol HCO_3^- km^{-2} a^{-1} for the calibration area. However, the correlation coefficient of the model using this single factor is only r=0.37. Model b-parameters are listed in table 16.

Adding lithology as a predictor improves prediction quality largely (RoLi-model; equation 14). The correlation coefficient of the RoLi-model is r=0.80 (Figure 16 A), its average predicted HCO_3^- yield is 0.38 10^6 mol km^{-2} a^{-1}. The order of HCO_3^- mobilization of individual lithological classes is (from high to low): *carbonate sedimentary rocks* (SC), *mixed sedimentary rocks* (SM), *basic plutonic rocks* (PB+), *siliciclastic sedimentary rocks* (SS), *acid volcanic rocks* (VA+), *basic volcanic rocks* (VB+), *acid plutonic rocks* (PA), *unconsolidated sediments* (SU+), and *metamorphic rocks* (MT). Compare table 13 for lithological classifications.

As representation for pH in rivers, which cannot be extrapolated and is not available for all monitoring stations, pH information from SOTER data is added to the model (Equation 15, Table 15).

This leads to a correlation coefficient of r=0.83 (RoLiPh-model; figure 16 B), with an average predicted yield of 0.39 10^6 mol HCO_3^- km^{-2} a^{-1}. Applying this model, the 10th percentile of all catchments with the pH-class value of 2 yields 71 % of the HCO_3^- compared to the 90th percentile with a pH-class of 4.

Adding instead land cover classes as predictor to the model (Equation 16) improves the correlation coefficient to r=0.84 (RoLiLc-model; figure 16 C). Furthermore, a shift in b-parameters is observable (Table 16). The parameter b_0 is reduced by more than factor three compared to the RoLi-model and RoLiPh-model. Some of this decrease can be attributed to the land cover part of the model, which is a linear factor of at least 1, thus reducing b_0. However, lithology related b-parameters are also the highest in the RoLiLc-model, indicating a predicted steeper increase of HCO_3^- yields with runoff. The average modeled HCO_3^- yield is 0.37 10^6 mol km^{-2} a^{-1}. According to the b-parameters, the used land cover classes generally increase HCO_3^- yield. Of the vegetated land cover classes, *shrubs* (LC4), which are scarce in the assessed catchments (average aerial proportion per catchment: 3.3 %; median 0.1 %) increase yield most, followed by *herbaceous lands* (LC5; average aerial proportion 16 %; median 13 %) and *managed lands* (LC1; average aerial proportion 17 %, median 8 %). The b-parameter of *urban area* (b_{LC8}) is high compared to the other land cover b-parameters (Table 16). Although hardly an average of 0.1 % per catchment are *urban areas* (median 0.01 %), the parameter is significant with p=0.008.

4.3.2 Modeled Ca/Na elemental ratios resulting from chemical rock weathering

Sodium mobilization per lithological class is modeled using equation 8 A. Modeling using the applied parameters is reasonable, because although the product of q (runoff) and c (concentration) directly equals terrestrial mobilized sodium (Na_{terr}) it does of course not equal the Cl-corrected Na_{sil}. The sum-term of the different lithological units with a model parameter each, assigns a silicate-derived Na^+ flux (Na_{sil}) to each considered lithological class. For statistical reasons, the lithological classes PA and MT had to be combined as well as the classes VB+ and PB+ (called PAMT and VBPB, respectively). The lithological classes used by the sodium (and calcium) models are thus PAMT, VA+, VBPB, SC, SM, SS and SU+. The model set up for sodium is run once for each correction "scenario", all b-parameters are significant on a level of 5 % (p_{max}=0.017). The correlation coefficient is 0.83, 0.82 and 0.84 for the Na_{sil1}, $Na_{sil0858}$ and $Na_{sil0731}$ models, respectively.
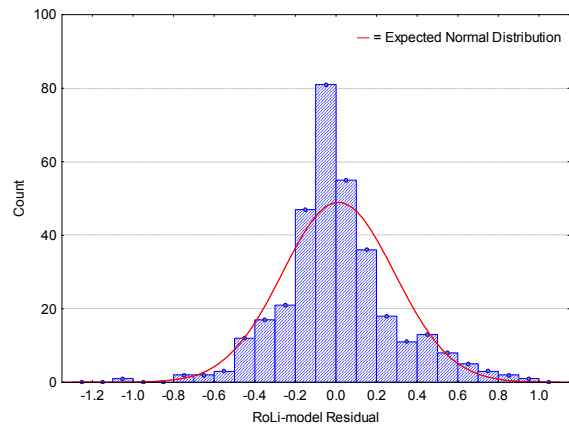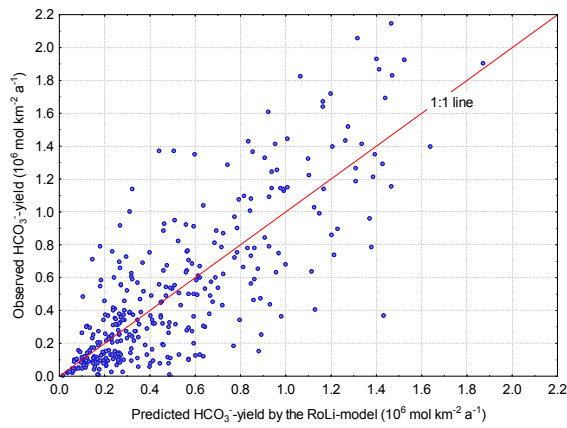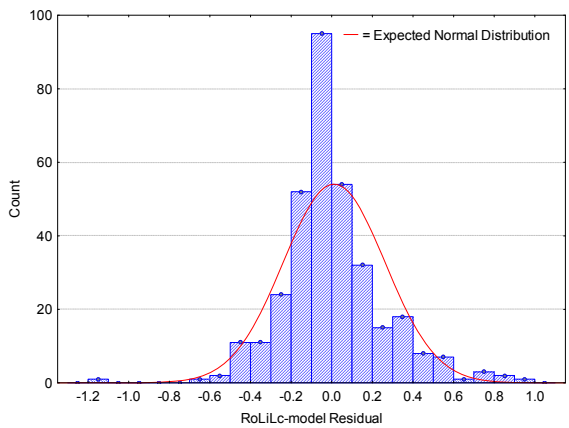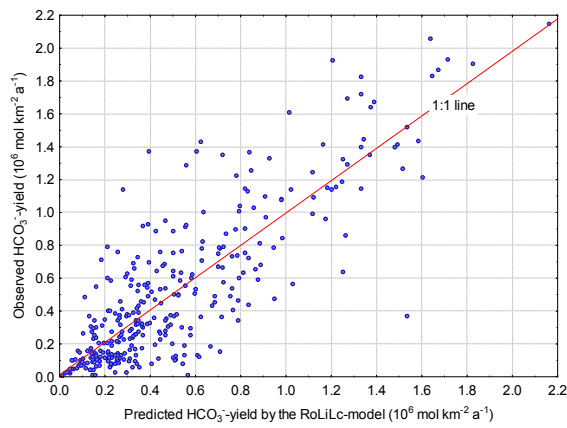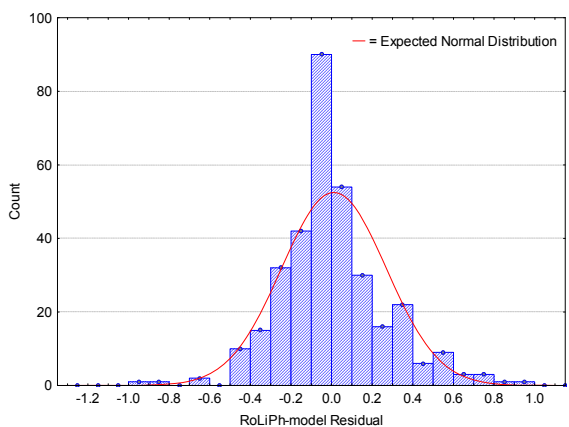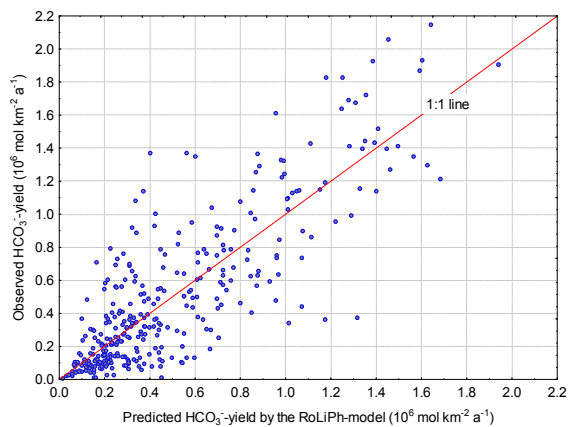
Figure 16: Model analysis for A) the RoLi-model B) the RoLiPh-model and C) the RoLiLc-model. On the left sides, observed versus predicted HCO$_3^-$-yields are plotted, on the right sides histograms of model residuals.

Equation 8 B describes HCO_3^- counterbalanced calcium mobilized by chemical weathering per lithological class and thus the theoretical maximum carbonate contribution to HCO_3^- fluxes, assuming that all Ca^{2+} is derived from carbonates. Ca^{2+} mobilization is calculated for calcium counterbalanced by alkalinity and sulfate (Ca_{alkso4}) as well as calcium counterbalanced by alkalinity, chloride and sulfate ($Ca_{alkclso4}$) for each of the three chloride correction scenarios (Na_{sil1}, $Na_{sil0858}$, $Na_{sil0731}$). The models have the same structure and use the same lithological classes as the sodium models. All b-parameters are significant on the 5 % level (p_{max}=0.018). The correlation coefficients of the Ca_{alkso4} models are 0.931 (for the 217 Na_{sil1} catchments), 0.936 (for the 254 Na_{sil858} catchments) and 0.944 (for the 280 Na_{sil731} catchments); the correlation coefficients of the $Ca_{alkclso4}$ models are 0.930 (Na_{sil1}), 0.936 (Na_{sil858}) and 0.941 (Na_{sil731}). Compare appendix C for b-parameters of the Na_{sil} and Ca_{hco3} models.

Table 17 lists results of the five different correction "scenarios". The highest Ca_{hco3}/Na_{sil} elemental ratios from chemical weathering are observable for the carbonate lithological classes SC (8.62-10.52) and SM (5.25-7.67), followed by the combined class of MT and PA (5.19-6.39). Then follow the sedimentary classes SU+ (2.42-8.18) and SS (2.82-4.89). The lithological classes PB+ (1.56-2.19), VB+ (1.59-2.80) and VA+ (0.70-0.90) show the smallest Ca_{hco3}/Na_{sil} elemental ratios of the modeled mobilizations from lithological classes.

Table 17: Results of the comparison between lithology source rock Ca/Na elemental ratios (Ca$_{sil}$/Na$_{sil}$) with modeled mobilized Ca/Na elemental ratios (Ca$_{hco3}$/Na$_{sil}$) per lithological class for three different non-silicate derived sodium corrections (1, 0.858 and 0.731 times Cl) and two non-bicarbonate calcium corrections (counterbalanced to equal portions by alkalinity and sulfate or alkalinity, non-sodium counterbalancing chloride and sulfate). Averages are derived from all 5 values for each lithological class.

	Cl-correction scenario	n	Rock Ca$_{sil}$/Na$_{sil}$	Water Ca$_{hco3}$/Na$_{sil}$		CA$_{sil}$/CA$_{hco3}$		CO$_2$/HCO$_3^-$	
				Ca$_{alkso4}$	Ca$_{alkclso4}$	Ca$_{alkSO4}$	Ca$_{alkclso4}$ [B]	Ca$_{alkso4}$	Ca$_{alkclso4}$
MTPA	Na$_{sil1}$	217	1.10	5.69	[B]	0.19	[B]	0.64	[B]
	Na$_{sil0858}$	254	1.09	6.39	6.24	0.17	0.18	0.60	0.61
	Na$_{sil0731}$	280	1.07	5.52	5.19	0.19	0.21	0.64	0.67
	Average			**5.81**		**0.19**		**0.63**	
SC	Na$_{sil1}$	217	324.88 [E]	8.62	[B]	0 [A]	[B]	0.5 [A]	[B]
	Na$_{sil0858}$	254	324.65 [E]	10.30	10.16	0 [A]	0 [A]	0.5 [A]	0.5 [A]
	Na$_{sil0731}$	280	323.75 [E]	10.52	10.21	0 [A]	0 [A]	0.5 [A]	0.5 [A]
	Average			**9.96**		**0.00** [A]		**0.50** [A]	
SM	Na$_{sil1}$	217	21.07 [D] [E]	6.43	[B]	0 [A]	[B]	0.5 [A]	[B]
	Na$_{sil0858}$	254	21.25 [D] [E]	7.67	7.66	0 [A]	0 [A]	0.5 [A]	0.5 [A]
	Na$_{sil0731}$	280	21.84 [D] [E]	5.28	5.25	0 [A]	0 [A]	0.5 [A]	0.5 [A]
	Average			**6.46**		**0.00** [A]		**0.50** [A]	
SS	Na$_{sil1}$	217	2.41	4.89	[B]	0.49	[B]	0.88	[B]
	Na$_{sil0858}$	254	2.32	3.56	3.51	0.65	0.66	0.92	0.93
	Na$_{sil0731}$	280	2.28	2.90	2.82	0.79	0.81	0.95	0.95
	Average			**3.53**		**0.68**		**0.93**	
SU+	Na$_{sil1}$	217	0.91	8.18	[B]	0.11	[B]	0.82	[B]
	Na$_{sil0858}$	254	0.93	4.20	3.94	0.22	0.24	0.80	0.82
	Na$_{sil0731}$	280	0.92	2.69	2.42	0.34	0.38	0.84	0.87
	Average			**4.29**		**0.26**		**0.83**	
PB+	Na$_{sil1}$	217	2.30	2.96	[B]	0.78	[B]	0.99	[B]
	Na$_{sil0858}$	254	2.33	2.18	2.19	1.06	1.06	1.00	1.00
	Na$_{sil0731}$	280	2.40	1.56	1.58	1.54	1.51	1.02	1.00
	Average			**2.10**		**1.19**		**1.01 (1.00)** [C]	
VA+	Na$_{sil1}$	217	0.57	0.98	[B]	0.58	[B]	0.97	[B]
	Na$_{sil0858}$	254	0.57	0.90	0.89	0.64	0.64	0.97	0.97
	Na$_{sil0731}$	280	0.57	0.70	0.71	0.83	0.80	0.99	0.98
	Average			**0.83**		**0.70**		**0.97**	
VB+	Na$_{sil1}$	217	1.70	2.80	[B]	0.61	[B]	0.92	[B]
	Na$_{sil0858}$	254	1.72	2.10	2.11	0.82	0.82	0.96	0.96
	Na$_{sil0731}$	280	1.75	1.59	1.63	1.10	1.00	1.02	1.00
	Average			**2.05**		**0.88**		**0.98 (0.97)** [C]	

[A] For the carbonate-rich lithological classes it is assumed that all mobilized calcium stems from carbonate weathering, neglecting the probably smaller amount released by silicate weathering.

[B] The Ca$_{alkclso4}$ models were not calculated for the Na$_{sil1}$ corrections because all chloride counterbalances sodium, thus the results would equal the Ca$_{alkso4}$ models.

[C] As results above 1 are not reasonable for the CO$_2$/HCO$_3^-$ ratio, those values have been replaced by 1 and the average has been recalculated (recalc. values given in brackets). This value will be used in further calculations.

[D] Source rock Na$_{sil}$/Ca$_{sil}$ elemental ratio for the lithological class SM is calculated using samples from the classes SS and SC, as only 14 rock samples could be classified "SM" (compare chapter 4.2.3.1).

[E] For carbonate source rocks, the rock Ca/Na ratio is not interpreted as Ca$_{sil}$/Na$_{sil}$ (compare chapter 4.4.2).

4.3.3 Calculated Ca/Na elemental ratios in source rocks

From the individual rock samples given in the source data, Ca/Na elemental ratios were calculated for each lithological class of which those between the 10th and 90th percentile in that class were considered for further calculations (Table 18). The average Ca/Na elemental ratio of the considered samples is smaller than that ratio for all samples for all lithological classes. This hints to some contributions of carbonate of which the largest are removed by using only data up to the 90th percentile.

Table 18: Ca / Na elemental ratios per lithological class. Data for SU and LO are from (USGS, 2001), data for all other lithological classes are taken from USGS (2008a). The statistics for LO were conducted using samples from SU (n=10723) and LO (n=23). Due to the lack of data, elemental ratios for the not listed lithological classes AD and DS are calculated using SU classified source data and are thus the same. Elemental ratios for acid, intermediate and basic volcanic as well as plutonic rocks are calculated including rocks only classified as igneous basic, intermediate or plutonic to increase sample size. Elemental ratios for PY were calculated using the same samples as VB due to unavailability of PY analysis. Elemental ratios for SM were calculated using the samples of SC and SS, plus 14 samples that were classified SM.

| Litho-logical class	All samples				Considered samples [c]		Literature values (for comparison)
	Number	Molar Ca/Na ratio			Number	Average molar Ca/Na ratio	
		Average	10th percentile	90th percentile			
SU	10723	3.90	0.14	4.02	8569	0.89	2.52[A]
LO	10746	3.89	0.15	4.02	8610	0.90	2.61[B]
MT	12706	6.99	0.12	6.08	10165	1.28	1.15[B]
PA	18110	0.82	0.09	0.99	14491	0.40	0.94[B]
PI	2924	1.37	0.33	2.32	2339	1.03	
PB	7185	9.58	0.93	15.05	5746	3.97	5.59[B]
SC	2734	454.05	20.05	1583.15	2188	237.01	605.95[B]
SM	14414	100.35	0.17	184.13	11511	16.73	13.78[B]
SS	11666	17.58	0.14	21.05	9329	3.15	5.28[B]
VA	10514	1.72	0.05	0.92	8412	0.26	0.36[B]
VI	17377	1.01	0.28	1.58	13900	0.84	
VB	24017	2.93	0.78	3.18	19213	1.92	3.19[B]
PY	24017	2.93	0.78	3.18	19213	1.92	

[A] River suspended sediments in rivers for North America (Viers et al., 2009).
[B] Data from the global geochemical composition of surface lithological classes after Hartmann et al. (submitted); in that study, lithological classes of Dürr et al. (2005) were applied.
[C] Samples with Ca/Na ratios between the 10th and 90th percentile of each lithological class.

Calculated Ca/Na elemental ratios from literature (Viers et al., 2009; Hartmann et al., submitted) are situated between the average Ca/Na ratios of the considered samples and the average ratios of all samples in the source database for each lithological class (Table 18). Exceptions are *basic volcanic rocks* (VB) and *carbonate sedimentary rocks* (SC), for which the value given by Hartmann et al. (submitted), who reviewed data from other studies, is higher than the average of all samples from the source database of the presented study. This indicates that our approach yields reasonable

results while it is highly regionalized, compared to the global studies referenced as literature values (Viers et al., 2009; Hartmann et al., submitted). Ca / Na elemental ratios of *carbonate sedimentary rocks* (SC) differ in literature and in this study. However, for SC it is difficult to give a ratio because while being dominated by limestone with extraordinary high Ca/Na elemental ratios, SC still contains siliciclastic units as shales with far lower Ca/Na elemental ratios. Furthermore, the Ca/Na ratio is used here to determine the proportion of silicate-calcium on total calcium. In SC this is zero per definition, thus the Ca/Na elemental ratios of those lithological classes are not explored further, here. A map of the sample localities and the source rock Ca/Na elemental ratio is given in figure 17.
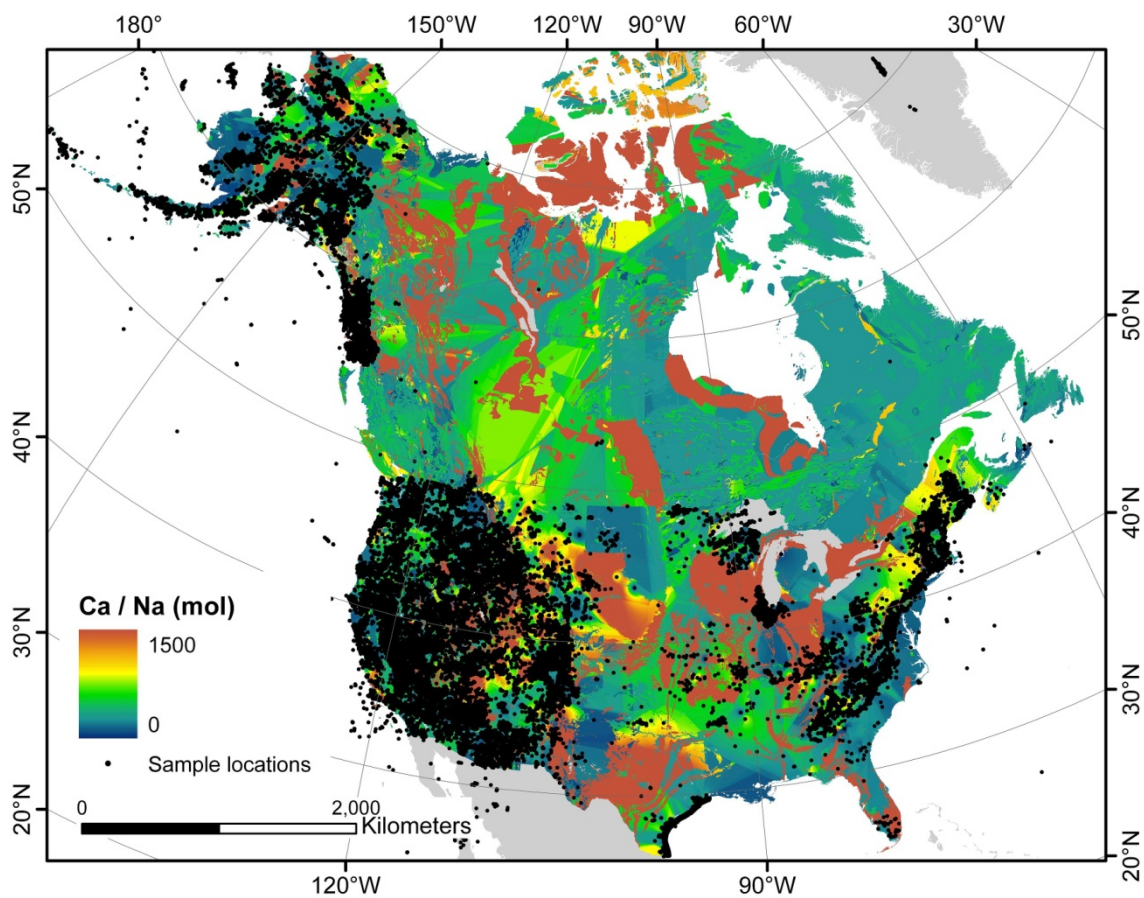
Figure 17: Source rock Na/Ca ratios and locations of the ~117 000 samples used for calculation of the ratios (each dot represents one sample, regardless of its assigned lithological class). Some lithological classes are clearly distinguishable, e.g. the carbonate sedimentary rocks (SC) south of Hudson Bay. Large areas in Canada are only covered by few sampling sites. However, only very few assessed catchments are located in those areas (Figure 14).

As the source rocks (except for the lithological classes SM and SC) are considered silicate rocks, their Ca/Na elemental ratios are used as Ca_{sil}/Na_{sil} for calculation of excess calcium.

Table 17 gives average values of Ca_{sil}/Na_{sil} calculated per lithological class for the considered catchments for each Na_{sil} correction scenario. Siliciclastic sediments (SU+ and SS) show Ca_{sil}/Na_{sil} elemental ratios of 0.91-0.93 and 2.32-2.41 (Table 17). The Ca_{sil}/Na_{sil} elemental ratios of igneous and metamorphic rocks indicate a difference between basic (PB+: 2.30-2.40 and VB+: 1.70-1.75: table 17)

and acid igneous rocks (VA+: 0.57-0.57 and PAMT: 1.07-1.10: table 17). Of course PAMT is a combination of *acid plutonic* and *metamorphic rocks*. However, table 18 suggests that the Ca/Na ratio of PA is lower than that of MT.

4.3.4 Results of modeled atmospheric/soil CO_2 proportion on HCO_3^- fluxes

To determine the proportion of excess calcium, the Ca_{hco3}/Na_{sil} elemental ratio has been calculated for each lithological class in all catchments with positive Na^+, Ca^{2+}, Cl^- and SO_4^{2-} elemental ratios for the respective corrections (n=217, 254 and 280 respectively). In table 17, the Ca_{sil}/Na_{sil} elemental ratios in the source rock, the Ca_{hco3}/Na_{sil} elemental ratios mobilized from the source rock and the resulting silicate-calcium versus mobilized calcium ratios are listed for the described five different correction scenarios for Ca_{hco3} and Na_{sil}.

Correction for Ca_{hco3} including non-sodium-counterbalancing Cl^- ($Ca_{alksclso4}$) yields only slightly smaller ratios of Ca_{sil}/Ca_{hco3} than Ca_{hco3} corrected for SO_4^{2-} only (Ca_{alkso4}). The maximum difference is 11 % for the small ratios of SU+. Larger differences can be observed for the three different elemental ratios which were used to correct sodium for chloride. The smaller the Cl_{terr}/Na_{terr} correction ratio becomes (Na_{sil1}> $Na_{sil0858}$ > $Na_{sil0731}$), the smaller ratios of Ca_{hco3}/Na_{sil} are expected. A smaller Cl_{terr}/Na_{terr} correction ratio means higher Na_{sil} while Ca_{hco3} remains the same. This pattern cannot be observed for all lithological classes due to a different sample size for the different correction ratios. With smaller Cl_{terr}/Na_{terr} correction ratio, corrections for fewer catchments result in negative sodium fluxes and more are included into the analysis (217, 254 and 280 respectively). Because a "correct" Cl_{terr}/Na_{terr} correction ratio cannot be determined for the catchments assessed in this study, and because the differences between both Ca_{hco3} corrections are minor, no preference was given to any single Ca_{sil}/Ca_{hco3} ratio per lithological class. For all five ratios, CO_2/HCO_3^- ratios were calculated.

The proportion of silicate-calcium is with 88 % for VB+ and 119 % for PB+ the highest in basic igneous rocks (Table 17). The unexpectedly high proportion of silicate-calcium in PB+ (>100%) could originate from the combination of *basic volcanic* and *plutonic rocks* (VB+ and PB+) in one class for mobilization modeling, while in the source rocks it could be distinguished and PB+ source rocks hold a higher Ca/Na elemental ratio than VB+ source rocks. Furthermore, the high Ca_{sil} proportion could hint to that sodium minerals were weathered preferentially, which is not likely as the literature suggests the opposite (e.g. Goldich, 1938; Blum, 1994). *Acid volcanic rocks* and *siliciclastic sedimentary rocks* (VA+ and SS) show both a contribution of about 70 % silicate-calcium in the mobilized fraction. Especially for SS this could be an overestimation if the sample rocks had a carbonate containing matrix unaccounted for in the rock classification of the analysis. Silicate-calcium contributes less than 30 % to total calcium fluxes from *unconsolidated sediments* (SU+). However, SU+ can contain loess or other carbonate containing clasts which would add to the excess-calcium contribution. For

metamorphic and *acid plutonic rocks* (MTPA), which had to be combined to model the Ca_{sil}/Ca_{hco3} ratio, only 20 % of the total mobilized Ca^{2+} is silicate-calcium. For PA it is expected that secondary carbonate or disseminated trace calcite could yield significant amounts of calcium (cf. Oliva et al., 2004; Hartmann, 2009). The lithological class MT can even include small marble units which of course yield a lot of dissolved calcium and could explain the high excess-calcium contribution. Furthermore, for all lithological units, thin loess layers, unaccounted for by the lithological map, could add to the modeled excess-calcium.

For calculation of CO_2/HCO_3^- a model of HCO_3^- fluxes is used that is designed to be comparable to the Na_{sil} and Ca_{hco3} models (Equation 9). The lithological classes MT and PA have been combined in this model to the class MTPA. This model shows correlation coefficients of r=0.74, r=0.76 and r=0.78 for the 217, 254 and 280 catchments resulting from the Na_{sil1}, $Na_{sil0858}$ and $Na_{sil0731}$ correction scenarios, respectively. Model b-parameters are given in appendix C.

The calculation of the ratio of consumed CO_2 per mol HCO_3^- is done according to equation 7. The CO_2/HCO_3^- ratio of the lithological classes SC and SM is manually set to 0.5. The lowest ratio of the non carbonate-rich lithological classes is 0.63 for *acid plutonic* and *metamorphic rocks* (PA and MT). They are followed by the siliciclastic sediments (SU+ and SS), which show calculated CO_2/HCO_3^- ratios of 0.83 and 0.93 respectively. Modeled CO_2/HCO_3^- ratios of *basic plutonic rocks* (PB+) and the volcanic lithological classes (VA+, VB+) are very close to 1 (1.00 and 0.97, respectively). From those lithological classes nearly all HCO_3^- represents consumed CO_2 according to the models.

4.3.5 Extrapolation of model results to North America

The models using runoff and lithology (RoLi-model) as well as runoff, lithology and land cover (RoLiLc-model) are extrapolated to the area of North America by applying them on the source data of the catchment attributes the models were calibrated on. The resulting raster datasets are calculated on a grid size of 200x200 m. Some describing statistics of the extrapolation results are listed in table 19.

Table 19: HCO_3^- yields and CO_2 consumption resulting from extrapolation of the models using runoff and lithology (RoLi-model) and runoff, lithology and land cover (RoLiLc-model) as predictors. [A]

|	HCO_3^-				CO_2			
	Average	Max. [B]	Sum	Sum	Average	Max. [B]	Sum	Sum
	10^6 mol km^{-2} a^{-1}	10^{12} mol a^{-1}	10^6 t C a^{-1}		10^6 mol km^{-2} a^{-1}	10^{12} mol a^{-1}	10^6 t C a^{-1}	
RoLi-model	0.32	7.46	6.32	75.93	0.21	7.22	4.16	50.00
RoLiLc-model	0.33	107.2	6.45	77.46	0.22	86.72	4.28	51.39

[A] The extrapolation does not distinguish between endorheic and exorheic areas.
[B] i.e. the value of the grid cell with the highest HCO_3^- or CO_2 yield of the extrapolated raster datasets.

The highest yields of the RoLi-model are situated in the northern Rocky Mountains (Figure 18). Furthermore, several areas in the North East show high HCO_3^- yields. Corrections of the RoLi-model using the calculated CO_2/HCO_3^- ratio (According to table 17) are especially visible in the eastern high HCO_3^- yielding areas which are predominantly underlain by carbonate containing lithological classes (SC and SM; figure 19). However, the northern Rocky Mountains remain a high yielding area for CO_2 consumption. The total CO_2 consumption of the North American continent resulting from the RoLi-model is 50.0 10^6 t C a^{-1}.

The RoLiLc-model reflects the general pattern of the RoLi-model. High HCO_3^- yields are situated in the northern Rocky Mountains, with still elevated yields from the carbonate-rich sediments in the east (Figure 20). However, urban centers are responsible for the highest HCO_3^- yields in the RoLiLc-model due to their very high b-parameter (i.e. 35.6; compare table 16). Some visible urban centers with very high modeled HCO_3^- yields are situated around the great lakes (Figure 20). Correction for carbonate contributions to HCO_3^- fluxes again impacts the eastern regions, underlain by carbonate-rich lithological classes, while the northern Rocky Mountains remain an area of high CO_2 consumption (Figure 21). The RoLiLc-model extrapolation calculates a total CO_2 consumption of 51.4 10^6 t C a^{-1}.

The calculated CO_2 consumption for North America of 50.0 or 51.4 10^6 t C a^{-1} for the RoLi-model and the RoLiLc-model, respectively, amounts to about 20 % of the world CO_2 consumption of chemical weathering, calculated by global models (Amiotte-Suchet et al., 2003; Hartmann et al., 2009).
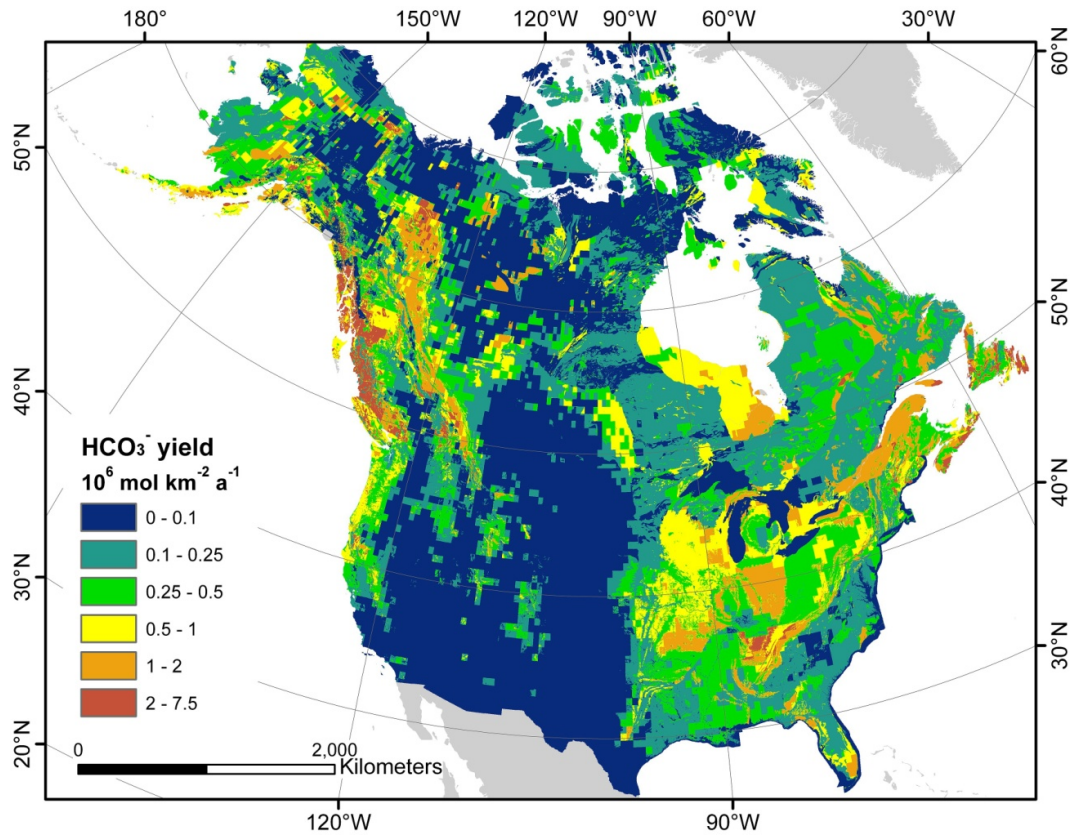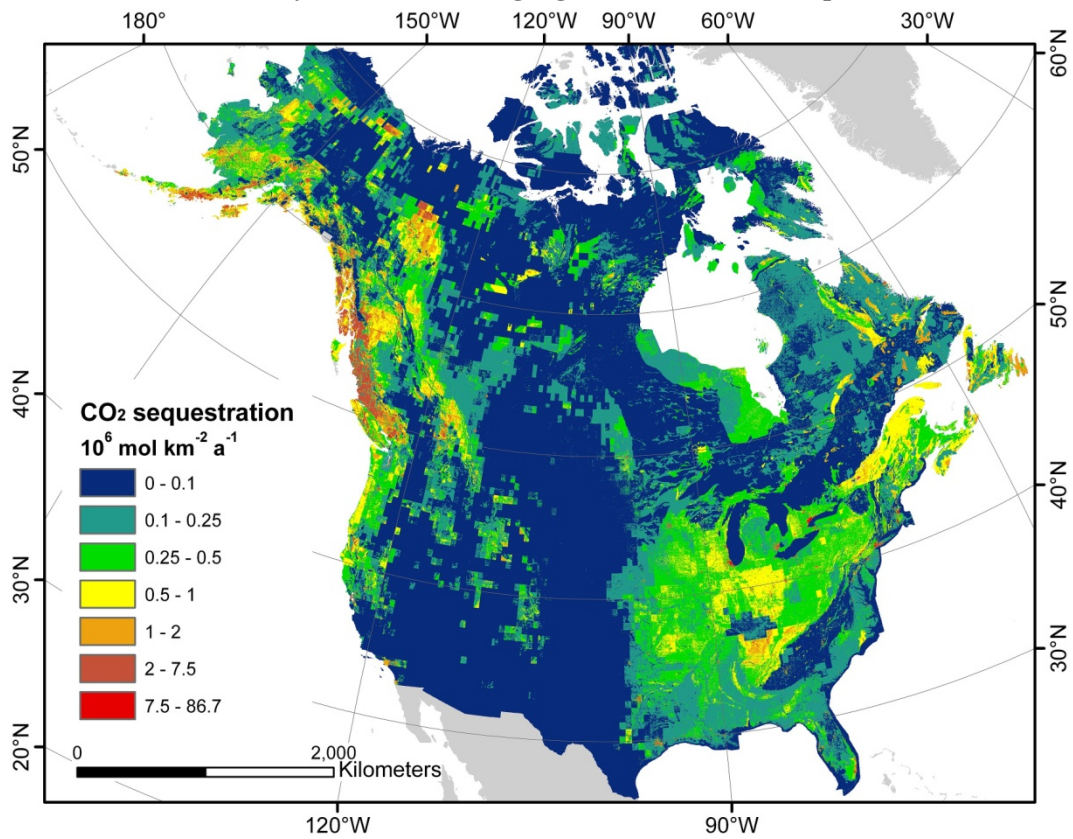
Figure 18: Extrapolation of the HCO_3^- yield calculated with the model using runoff and lithology as predictors (RoLi-model) to North America.
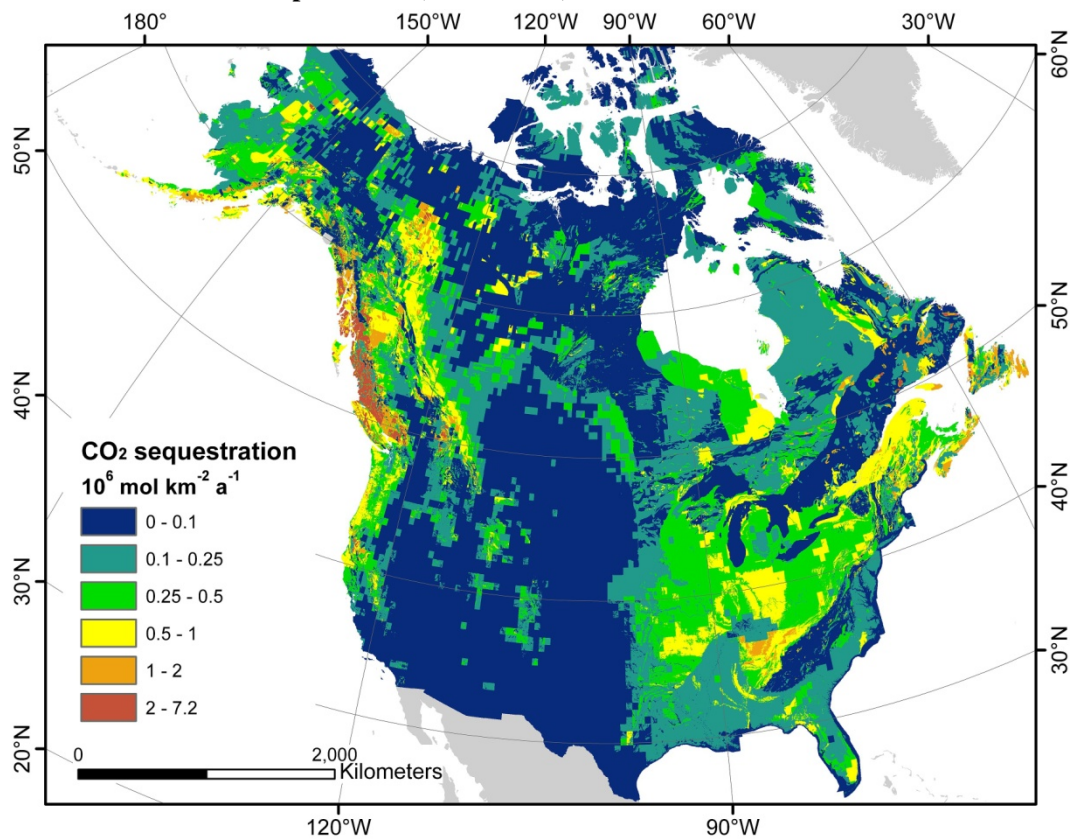
Figure 19: Extrapolation of the CO_2 yield calculated with the model using runoff and lithology as predictors (RoLi-model) to North America.
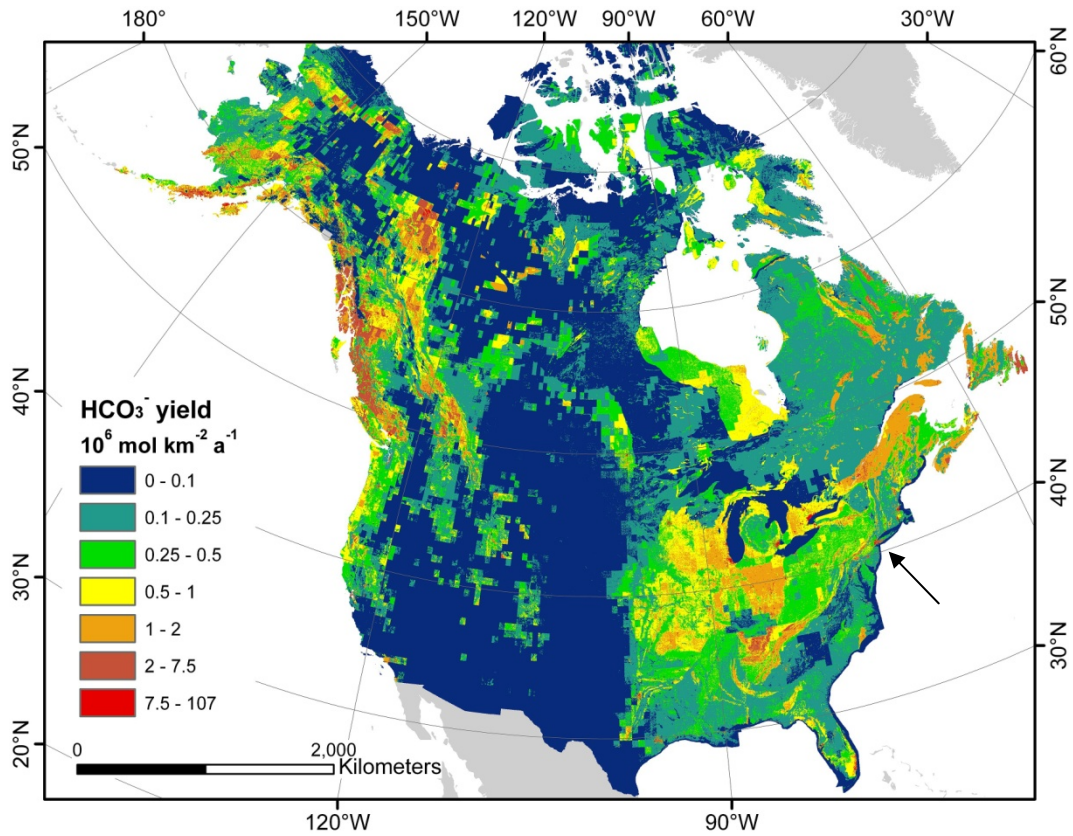
**Figure 20: Extrapolation of the HCO$_3^-$ yield calculated with the model using runoff, lithology and land cover as predictors (RoLiLc-model) to North America. Urban areas are distinguishable due to their high HCO$_3^-$ yields. An arrow highlights New York as example.**

Figure 21: Extrapolation of the CO$_2$ yield calculated with the model using runoff, lithology and land cover as predictors (RoLiLc-model) to North America.

4.4 Discussion

4.4.1 Factors affecting bicarbonate mobilization

4.4.1.1 Runoff and Lithology

Supporting results of previous works (e.g. Amiotte-Suchet et al., 2003; Hartmann, 2009), this study identifies runoff and lithology as major controlling factors of HCO_3^- yields from catchments. The correlation coefficient of r=0.80 of the RoLi-model and the close to symmetrical distribution of residuals suggest that those two factors alone in general already predict the observed HCO_3^- yield well (Figure 16 A).

The b-parameters of all lithological classes are smaller than 1, which means that increasing runoff is accompanied by a decrease of HCO_3^- concentration for all lithological classes. This hints at a kinetic limitation of weathering derived fluvial HCO_3^-. The order of lithological classes regarding HCO_3^- yield per runoff remains fairly constant for the three developed models incorporating lithology (Table 16). The lithological classes SC, SM and PB+ yield most HCO_3^-, followed by SS and VA+, then by VB+, PA and SU+, while the least HCO_3^- per runoff yielding lithological class is MT (Figure 22).
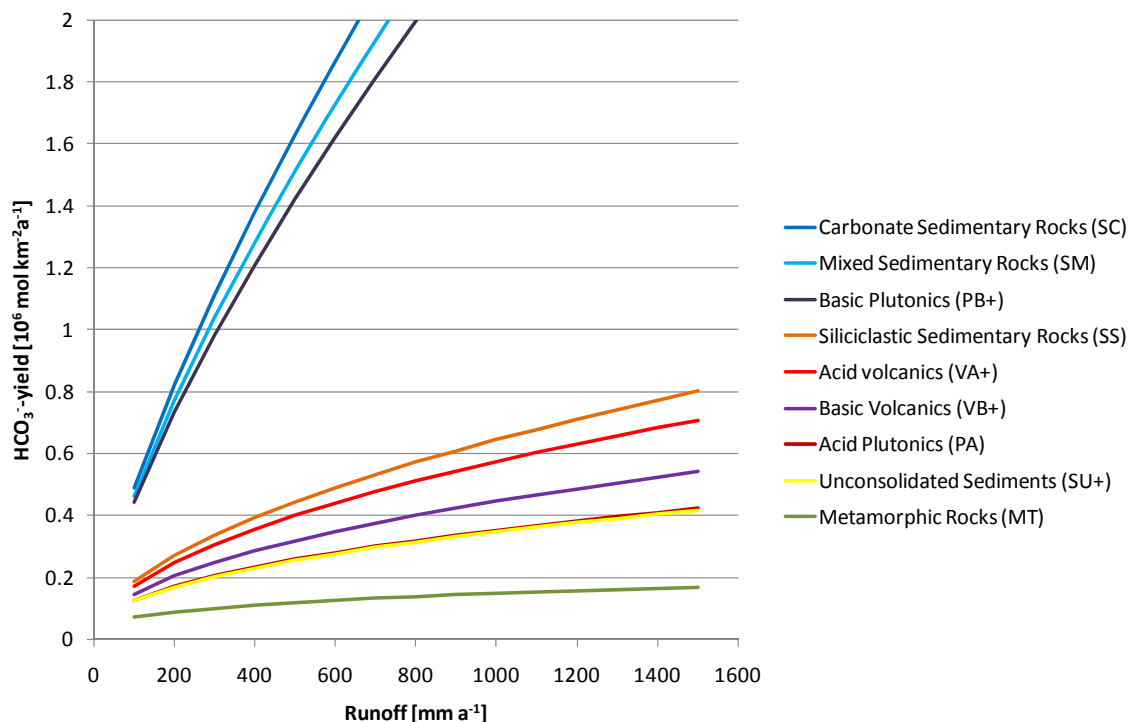
Figure 22: Modeled HCO_3^- yields for applied lithological classes by the RoLi-model. Note that the lines representing modeled yields for acid plutonic rocks (PA) and unconsolidated sediments (SU+) overlap.

It is surprising to see VB+ in the lower yielding group close to SU+ and PA, as *basic volcanic rocks* were attributed high HCO_3^- yields in previous studies (Amiotte-Suchet et al., 2003; Hartmann, 2009). In a study using comparable source data, VB+ was found to yield the second most DSi of all

lithological classes (About the same as PB+, compare chapter 3.3). However, comparably small HCO_3^- yields of VB+ is observed in the results of all three models incorporating lithology in this study.

Unfortunately, there are only three catchments with more than 60 % aerial proportion of VB+. On the six catchments covered to more than 50 % by VB+, a runoff only model (Ro-Model, equation 13) was calibrated (r=0.93). The parameter b_0 was insignificant (p=0.27), but with an estimation of 0.016 close to the b_0 of the RoLi-model for all catchments. Nevertheless, the b_1-parameter was significant (p=0.014) and with an estimate of 0.477 close to the b_{VB} parameter in the RoLi-model (i.e. 0.483, table 16). This suggests that the b_{VB} parameter in the RoLi-model is robust. However, HCO_3^- yield from *basic volcanic rocks* in North America should be examined closer if data for catchments covered by VB+ can be obtained.

4.4.1.2   pH value

The RoLi-model residuals show a significant positive trend for increasing river-pH (Figure 23 A). For river-pH values below 7, the RoLi-model hardly underestimates observed HCO_3^- yields, while for larger pH values the majority of HCO_3^- yields are underestimated by the RoLi-model. However, river-pH is only available for 324 monitoring stations and does not qualify as model predictor because it cannot be used for extrapolation of the model to North America. Another significant positive trend of RoLi-model residuals exists for increasing soil-pH (Figure 23 B). Soil-pH could represent conditions at the site where rock weathering takes place. Adding soil-pH as additional model predictor slightly increases model prediction quality (Equation 15, figure 16 B).

Brady and Walther (1989) reviewed literature data to show that in laboratory experiments silicate dissolution rates for anorthite, nepheline, low albite, bytownite, forsterite and enstatite positively correlate both with decreasing pH values smaller than about 6 but also increasing pH-values greater than about 8. Rozalen et al. (2009) found a similar U-shaped curve for pH-dependency of montmorrillonite weathering rates with a minimum at about pH 6 in laboratory experiments. However, chemical weathering rates in natural environments were shown to differ in the order of one to three magnitudes from laboratory experiments (e.g. Paces, 1983; Schnoor, 1990). These differences can be caused e.g. by organic controls (cf. Rosling, 2009), which in turn show complex relations to pH (cf. Kalbitz et al., 2000).

Moreover, the trend of RoLi model residuals with soil-pH (Figure 23 B) is based mainly on the difference of the two SOTER classes 2 and 3 (pH value 4.5 – 6.5). The very coarsely classified values with a low spatial resolution do not seem to qualify for model extrapolation. Furthermore, the soil-pH data from SOTER are extrapolated worldwide per soil unit, based on 10089 soil profiles of which

only 450 originate from North America (Batjes, 2006). Considering these shortcomings, soil-pH is not used for further modeling.
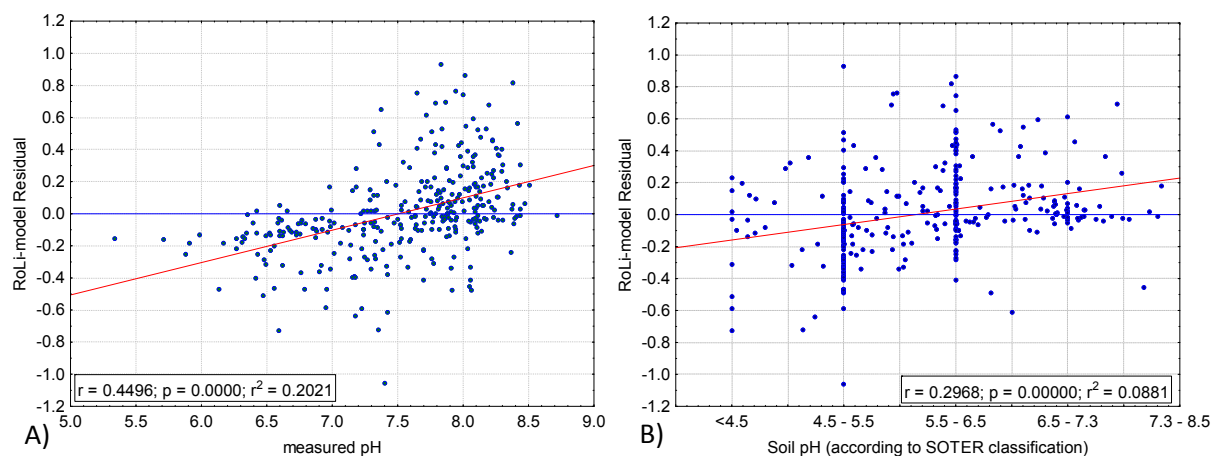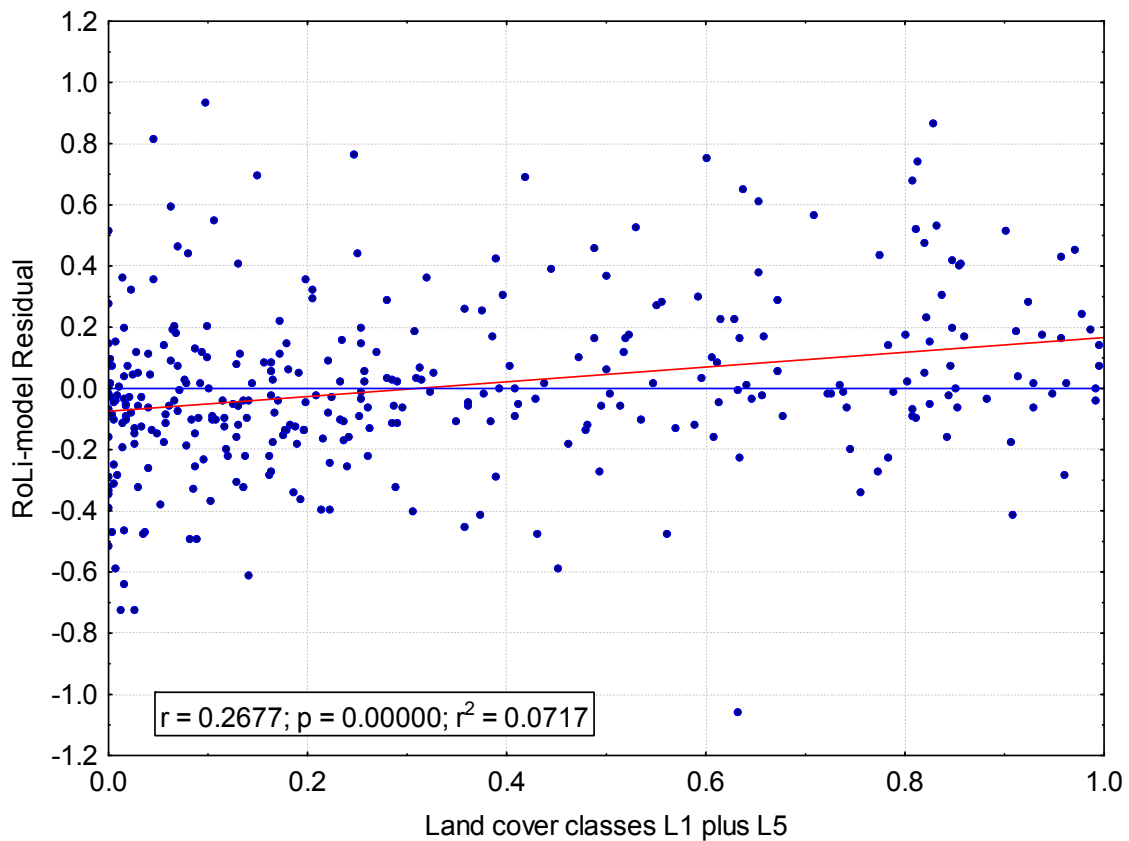

Figure 23: Graph of RoLi-model residuals versus A) measured pH values and B) soil-pH (from Batjes, 2006). The horizontal axis of B) is not on a metric scale due to the classification of pH values in the SOTER dataset that has been translated into pH-value ranges in this figure (compare Table 15). Measured pH values are discharge-weighted, similar to Equation 4. The p and r values of the red trend lines in both figures, are given in the figures. The blue lines indicate a residual of 0, which would be an exact prediction. Residuals are calculated as observed minus predicted.

4.4.1.3   Land cover

Land cover is applied in the RoLiLc-model as additional predictor to model HCO_3^- yield. Residuals of the RoLi-model show a significant positive trend with abundance of the sum of *managed lands* and *grasslands* (LC1+LC5, Figure 24). Although it does only slightly improve model quality of the RoLi-model, the RoLiLc-model adds explanation in detail and shows smaller, more symmetrical residuals (Figure 16 C). Land cover integrates a number of potential controlling factors of chemical weathering rates. Apart from the apparent connection to biological activity, there is a close connection, highlighted by several correlations, between land cover and soil-pH, as mapped by SOTER (Table 20). Thus, it can be assumed that using land cover as predictor includes a proportion of soil-pH information. Furthermore, soil bulk density and carbon content, according to SOTER data, are correlated to various land cover classes (Table 20).

The b-parameters for land cover (Table 16) suggest that areas covered by *managed lands* (LC1), *shrubs* (LC4), *grasslands* (LC5) and *urban areas* (LC8) positively influence HCO_3^- yield compared to areas with other land cover. The sum of the aerial proportions of the four land cover classes used for the RoLiLc-model (LC1, LC4, LC5 and LC8) plus the two forested classes (L2 and L3) cover more than 90 % of all but 6 catchments. Thus, also including the forested land cover classes (which would show negative b-parameters) would result in a loss of significance. By using LC1, LC4, LC5 and LC8 for modeling, the other land cover classes (mostly LC2 and L3) become the reference value. For those areas, the land cover part of equation 16 equals 1.

81

Figure 24: Graph of residuals of the HCO$_3^-$ yield model using only runoff and lithology as predictors (RoLi-model) versus the sum of the aerial proportions of land cover classes "managed lands" and "grasslands" (LC1 and LC5). Compare table 14 for a description of the land cover class classification. Residuals are calculated as observed minus predicted.

The influence of land cover on HCO$_3^-$ fluxes in rivers suggested by the RoLiLc-model was also reported by other studies. Moulton et al. (2000) suggested that increased HCO$_3^-$ flux from forested areas compared to bare rock areas in Iceland may be an effect of enhanced weathering by trees. However, bare rock areas are not well represented in the calibrating catchments of this study; only two catchments are covered by more than 0.1 % of LC9 (*Bare Areas*). Raymond and Cole (2003) suggested that differences in alkalinity export of subcatchments from the Mississippi are caused by land cover; agricultural land cover (similar to the here used LC1) would increase alkalinity export by a factor of more than two compared to forest land cover. In the RoLiLc model, *managed lands* (LC1), *shrublands* (LC4), *grasslands* (LC5), and especially *urban areas* (LC8) increase HCO$_3^-$ fluxes. The b-parameter for urban areas is 6-36 times higher compared to other land cover classes. Its significance despite of the small proportion of urban area on the calibrating catchments (0.1 % on average) underscores the large potential anthropogenic influence on fluvial HCO$_3^-$ fluxes (cf. Blume, 1996; Baker et al., 2008; Barnes and Raymond, 2009).

One hypothesis to explain the observed influence of grass-and shrub-related land cover classes (LC1, LC4 and LC5) is that they would shield soils from climate impacts less than forests (LC2 and LC3) do.

Forest canopies shield soils from rain, wind and temperature extremes. The lack of a canopy shield may increase physical weathering rates and thus increase supply of fresh mineral surfaces for chemical weathering. However, especially interesting is the high b-parameter for *urban area* (LC8). The large increase in HCO_3^- fluxes could be due to a shift of the river water composition by groundwater used for domestic or industrial applications. Groundwater is likely to contain more dissolved solids, including HCO_3^-, compared to surface runoff due to its long contact with potentially soluble mineral components (e.g. Livingstone, 1963). Furthermore, cities are built mostly of concrete, which is basically a porous, carbonate-containing artificial rock and subject to weathering. Additionally, weathering of building material debris in urban and suburban soils, although more common in Europe than North America, may influence river chemistry (Blume, 1996). Moreover, waste water treatment plant effluents and landfill leachates, both likely to be associated with urban areas, have been reported to exhibit high DIC concentrations (Barnes and Raymond, 2009). Regional studies comparing different catchments in the northeastern U.S. (Barnes and Raymond, 2009) and Britain (Baker et al., 2008) also found urban areas to largely increase riverine DIC yields. Additionally, Williams et al. (2005) found cation yields, necessary to counterbalance the proposed increased urban HCO_3^- yields, to strongly increase with urban area in a river in Massachusetts. However, understanding the exact processes underlying the modeled relations of land cover and HCO_3^- yield as well as the sources of that HCO_3^- still needs further investigation.

Apart from possible processes, correlations between proportions of land cover classes and other potential controlling factors of HCO_3^- yield may be responsible for at least part of the modeled influence. However, although proportions of land cover classes are correlated to a number of other potential controlling factors (Table 20), no clear pattern is observable that would explain the higher HCO_3^- yields from LC1, LC4, LC5 and LC8 compared to LC2 and LC3.

Table 20: Correlation coefficients for aerial proportion of different land cover classes and selected catchment attributes. Correlation coefficients printed in bold red are significant on the p<0.05 level.

	LC1	LC4	LC5	LC8	LC2	LC3
	Managed land	Shrubland	Grassland	Urban area	Broadleaved forest	Needleleaved forest
MT	**-0.26**	-0.04	**-0.27**	0.04	**0.17**	**0.15**
PA	**-0.19**	**0.22**	-0.08	-0.02	-0.1	**0.2**
SC	**0.4**	**-0.15**	**0.26**	0.07	-0.03	**-0.31**
SM	**0.18**	-0.08	**0.25**	-0.03	**-0.14**	-0.1
SS	**-0.11**	-0.08	-0.08	-0.05	**0.22**	-0.06
SU+	0.08	0.04	0.1	0.05	-0.03	-0.08
PB+	**-0.19**	-0.03	**-0.16**	-0.02	**-0.13**	**0.3**
VA+	**-0.17**	**0.32**	**-0.19**	-0.06	**-0.28**	**0.36**
VB+	**-0.19**	**0.16**	**-0.22**	-0.11	**-0.21**	**0.36**
Soil blk.dens.	0.13	0.08	-0.05	0.1	**0.18**	**-0.26**
Soil C_{org}	**-0.21**	**-0.16**	**-0.14**	-0.06	-0.05	**0.29**
Soil-pH	**0.27**	**0.45**	**0.42**	-0.08	**-0.51**	-0.03
Elevation	**-0.29**	**0.52**	**-0.15**	**-0.18**	**-0.42**	**0.51**
Temperature	**0.21**	**-0.24**	0.11	**0.2**	**0.28**	**-0.36**

Equation 17) $F_{HCO_3^-\,j} = Lithology - Part \cdot \left(1 + \sum_n^{1,4,5,8} A_{LC_n,j} \cdot b_{LC_n}\right)$

Equation 17: The RoLiLc-model land cover part is calculated by adding the sum of the aerial proportions of each land cover class (n) per catchment (j) multiplied by a b-parameter (b_{LC_n}) to 1. The numbered land cover classes are LC1 (managed lands), LC4 (shrublands), LC5 (grasslands) and LC8 (Urban areas). The lithology-part of the RoLiLc-model is left out here for simplicity; it is described in equation 16.

The RoLiLc-model (Equation 16) is split in two parts: one part modeling the influence of lithology, the other part modeling the influence of land cover. The land cover part of equation 16 is extracted in equation 17. The impact of land cover on the model results of each individual catchment can be calculated inserting the land cover proportions of that catchment and the b-parameters for the respective land cover classes (Table 16) in equation 17. The thus calculated impact factor quantifies the impact of land cover on model results relative to a catchment lacking coverage by the land cover classes included in the model (LC1: *managed lands*; LC4: *shrubs*; LC5: *grasslands* and LC8: *urban areas*); the land cover impact factor of a catchment lacking these land cover classes would be 1. The maximum impact of land cover on HCO_3^- flux for an individual catchment that is realized in the calibrating catchments is a factor of 4.82. However, the land cover impact factor is smaller than 1.77 in 75 % of the calibrating catchments and smaller than 1.14 in 25 % of them. The modeled impact of land cover on HCO_3^- yield per lithological class is visualized in figure 25.

To assess the impact of each single land cover class its aerial proportion on each individual catchment is inserted into equation 17 combined with its associated b-parameter (Table 16), without inserting the other land cover classes. This results in the impact factor of this single land cover class on HCO_3^- fluxes relative to a catchment lacking the land cover classes LC1, LC4, LC5 and LC8. Impact factors of a single land cover class on the HCO_3^- flux that are realized in the calibrating catchments are: LC4 (max.: 4.79, 80th percentile of catchments: 1.09), LC5 (max.: 1.87, 80th percentile: 1.30), LC1 (max.: 1.72, 80th percentile: 1.27) and LC8 (max.: 1.67, 80th percentile: 1.05).
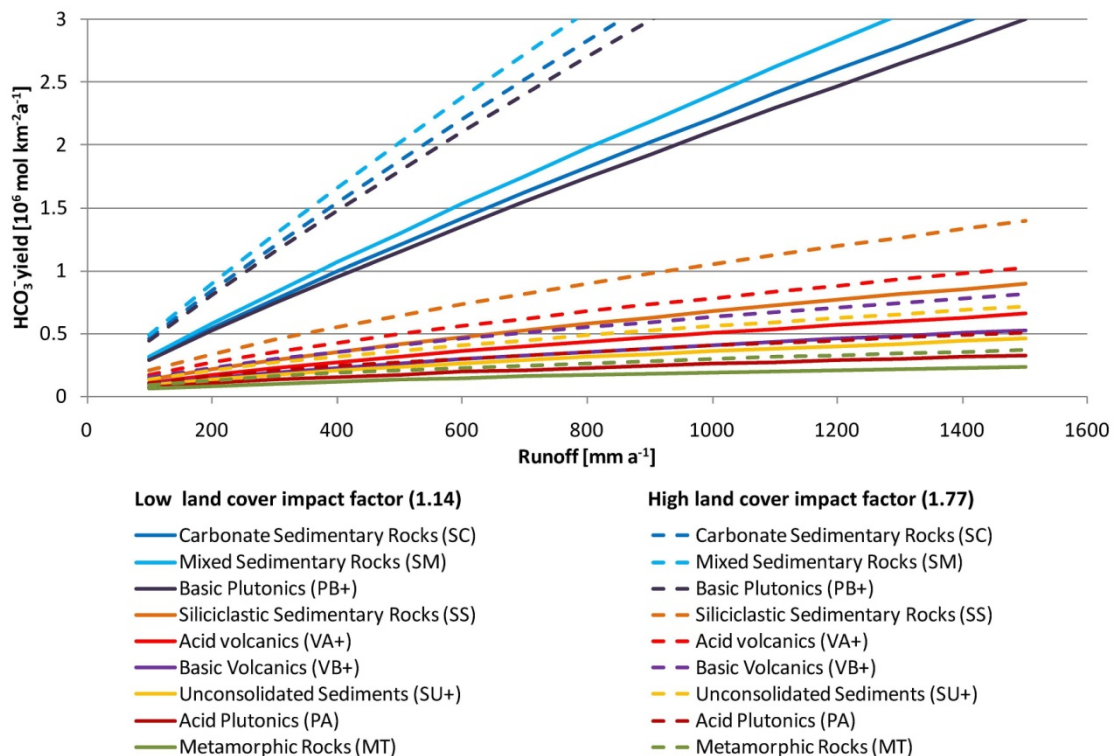
Figure 25: The RoLiLc-model has been calculated for the land cover impact factors 1.14 and 1.77. Those factors represent the 25th and 75th percentile of realized land cover impact factors in the calibrating catchments. Land cover impact factor means the increase of modeled HCO_3^- yields due to the land cover part of the RoLiLc-model (Equation 17). Compare the text for further explanation of the land cover impact factor.

4.4.1.4   Other factors

The model residuals are only weakly correlated to other parameters (Table 21). Some negative correlations exist to the climatic parameters annual precipitation and annual average temperature. While the RoLi-model and the RoLiPh-model show some correlations to land cover classes, for the RoLiLc-model no significant correlations of residuals to land cover classes can be observed. The latter is of course expected and suggests robustness of the model. Still, all three models underestimate catchments with irrigation. However, although it is not unexpected, this weak correlation is based on only few catchments with large irrigated areas and does not seem numerically meaningful. Nonetheless, irrigation will impact HCO_3^- fluxes, especially when groundwater is used.

Table 21: Correlation coefficients of the presented models residuals with selected catchment attributes. Coefficients printed in bold red are significant on the p<0.05 level.

Catchment attribute	RoLi Residual	RoLiPh Residual	RoLiLc Residual
Annual precipitation [mm a^{-1}]	**-0.22**	**-0.21**	**-0.21**
Ann. avg. temperature [°C]	**-0.14**	**-0.12**	**-0.14**
Managed lands (LC1) [aerial %]	**0.27**	**0.21**	0.07
Broadleaved forest (LC2) [aerial %]	**-0.27**	**-0.14**	-0.08
Needleleaved forest (LC3) [aerial %]	-0.05	-0.08	0.02
Shrubland (LC4) [aerial %]	0.07	0.04	-0.05
Grassland (LC5) [aerial %]	**0.2**	0.1	0.03
Aquatic vegetation (LC7) [aerial %]	0.01	0.06	-0.01
Urban area (LC8) [aerial %]	**0.14**	**0.12**	-0.01
Bare area (LC9) [aerial %]	-0.01	-0.06	-0.08
Water and ice (LC10) [aerial %]	0.07	0.07	0.01
Irrigated lands [ha cell^{-1}]	**0.18**	**0.16**	**0.13**
Loess (lithological class LO) [aerial %]	**0.13**	**0.13**	**0.13**
Population density [capita km^{-2}]	**0.2**	**0.18**	0.08
Annual GRDC-runoff [mm a^{-1}]	-0.01	-0.04	-0.04
Soil-pH [SOTER classes]	**0.3**	0.07	**0.18**
Elevation [m]	**0.11**	0.03	0.09
Slope [°]	-0.09	-0.08	-0.09
HCO$_3^-$ [10^{-3} mol L^{-1}] [A]	**0.50**	**0.48**	**0.45**
AER [eq eq^{-1}] [B]	**0.18**	**0.19**	**0.27**

[A] i.e. runoff weighted concentrations (Compare chapter 4.2.1.2)
[B] i.e. the anionic equivalent ratio HCO$_3^-$ / (HCO$_3^-$ + SO$_4^{2-}$ + Cl$^-$) in equivalent km^{-2} a^{-1}, similar to Hartmann (2009).

Loess is the only lithological class whose aerial proportion shows a significant correlation to the model residuals (Table 22). It is likely that loess contains more carbonate than the other unconsolidated sediments it is grouped with. Thus its HCO$_3^-$ yield would be underestimated by the model. But this influence cannot be further assessed with our data, as only 5 catchments are covered to more than 1 % by the lithological class loess (LO). Nonetheless, the impact of loess on HCO$_3^-$ yield should be considered when developing possible advanced versions of the lithological map of North America. In the current version, loess is underrepresented in the map when compared to other sources (Bettis et al., 2003; Dürr et al., 2005).

The correlation of model residuals to population density is significant for the RoLi-model and RoLiPh-model, but smaller and insignificant for the RoLiLc-model. This is attributed to including the land cover class LC8 (*urban area*), which is correlated to population density (r=0.68, p<0.01).

It is important to note that residuals from all models are correlated to HCO$_3^-$ concentrations (Table 21, figure 26 A) and the ratio of HCO$_3^-$ / (HCO$_3^-$ + SO$_4^{2-}$ + Cl$^-$) in equivalents measured in the river (AER,

table 21, figure 26 B). Correlations to concentration are also observable for DSi concentration in the model for DSi yield (Chapter 3; Jansen et al., 2010) and in HCO_3^- models calibrated on Japanese catchments (Hartmann, 2009). Hartmann (2009) also reports that including the ratio of HCO_3^- divided by the sum of SO_4^{2-} and Cl^- into his models improves prediction quality. However, no predictor based on spatial datasets was found here to reduce these correlations. Such a predictor might further improve the models. Nevertheless, because the distribution of model residuals of the RoLiLc-model is close to normal (Figure 16 C), no significant bias from potential controlling factors not represented in the model is expected.
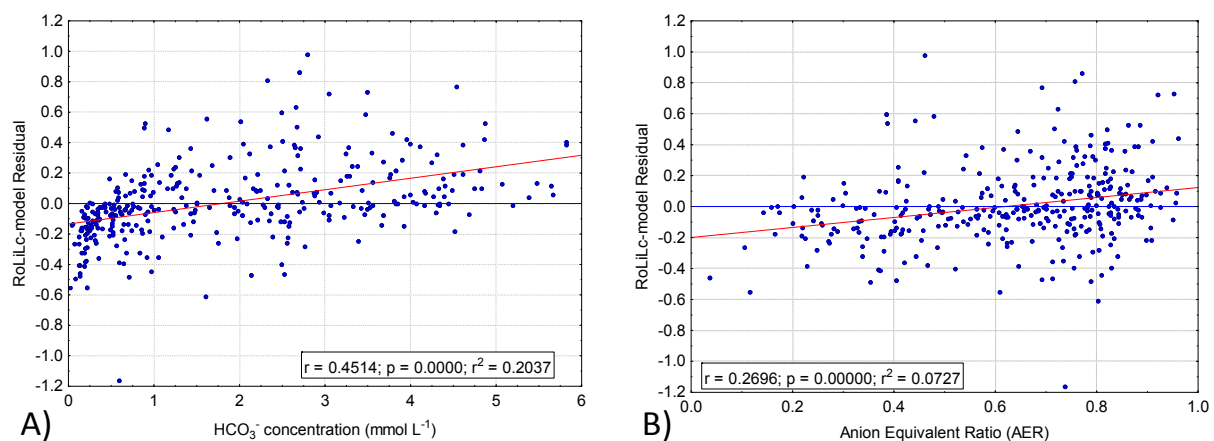
Figure 26: RoLiLc-model residuals plotted against A) weighted HCO_3^- concentration and B) anion equivalent ratio (AER; i.e. $HCO_3^- / (HCO_3^- + SO_4^{2-} + Cl^-)$). Significant trends to underpredict higher HCO_3^- concentrations and higher AER are shown by the red lines. Residuals are calculated as observed minus predicted.

4.4.2 Modeled atmospheric/soil CO_2 proportion on HCO_3^- fluxes

The molar ratios of consumed atmospheric/soil CO_2 per HCO_3^- flux (in short: CO_2/HCO_3^- ratio) calculated in this study are smaller compared to Hartmann (2009) for SU+ (here: 0.83, Japan: 1 (not calculated)), MT (here: 0.63, Japan: 0.68), PA (here: 0.63; Japan 0.88), VA+ and VB+ (here both: 0.97; Japan both: 1 (not calculated)) and SM (here: 0.5 (per definition); Japan: 0.65). Only the lithological class SS shows a larger CO_2/HCO_3^- ratio than calculated for Japan by Hartmann (2009) (here: 0.93; Japan: 0.88). However, differences are expected and attributed to the different geological evolution of Japan and North America as well as the scarcity of carbonate rocks in Japan. Moreover, areas possibly affected by loess are missing in Japan. The average CO_2/HCO_3^- ratio of 0.7 calculated for North America is virtually identical to the ratio of 0.73, given by Lerman et al. (2007) as world average.

In contrast to the study of Hartman (2009) in Japan, the lithological classes SC and SM (*carbonate* and *mixed sedimentary rocks*) are considered to yield only carbonate derived HCO_3^-. This dominance of carbonate contributions to HCO_3^- flux is assumed because carbonate weathering rates exceed

those of shale and sandstone by far (Factors 5 and 9, respectively: Meybeck, 1987). Furthermore, the method of comparing a silicate source rock Ca/Na elemental ratio with the observed ratio of mobilized Ca/Na (Chapter 4.2.3) is not applicable for *carbonate sedimentary rocks* (SC) and *mixed sedimentary rocks* (SM), because they are not silicates. Most of the rock samples used for SC source rock Ca/Na elemental ratios are limestone, with high measured Ca/Na elemental ratios of up to 1538 (The highest value of considered source rock Ca/Na ratios, cf. chapter 4.2.3.1). The combination of those high ratios with layers of siliciclastic sediments, too fine to be mapped within SC and included in SM, could result in higher Ca/Na elemental ratios in the source rock than in the water (Table 17). For the other lithological classes, with exception of PB+ for some Na_{sil} corrections and VB+ for $Na_{sil0731}$, mobilized Ca/Na elemental ratios in the water are higher than those in source rock.

An explanation for the low CO_2/HCO_3^- ratios for PA and MT (*acid plutonic* and *metamorphic rocks*) may be the contribution of trace calcite that e.g. Mast et al. (1990) suggest to contribute nearly 40 % of the cations in rivers draining granite and gneiss in Colorado. However, the excess-calcium leading to the low CO_2/HCO_3^- ratios calculated for PA and MT could also originate from calcic silicates (e.g. April et al., 1986; Drever and Hurcomb, 1986; 2004), or apatite (e.g. Blum et al., 2002). Contribution of those minerals to Ca^{2+} fluxes would lead to an overestimation of carbonate contribution and thus an underestimation of CO_2/HCO_3^- ratios for PA and MT. For the siliciclastic sediments (SU+, SS) carbonate phases in the matrix of sediments are not unexpected and would explain the modeled excess-calcium and CO_2/HCO_3^- ratios (Table 17). However, the rock samples used as silicate source rock for excess-calcium contribution could also be contaminated with carbonate. This would lead to an underestimation of the carbonate contributions of those lithological classes. The CO_2/HCO_3^- ratios for VA+ and VB+ are very close to 1, the ratio for PB+ is 1. The small deviations from 1 could be due to small carbonate contributions from vein calcite or thin loess layers. However, a difference of 0.03 is also well within the potential error of the CO_2/HCO_3^- ratio calculations. Furthermore, attribution of excess-calcium to carbonate dissolution assumes equal weathering rates of calcium or sodium from silicate rocks. This simplification is necessary here because quantitatively differentiating weathering rates of Na^+ and Ca^{2+} from silicate rock is too complex for the scale of this study. However, the approach may lead to underestimation of silicate calcium, as it is assumed that e.g. calcium containing plagioclase is more susceptible to weathering than sodium plagioclase species (e.g. Goldich, 1938; Blum, 1994).

Apart from chemical rock weathering, Ca^{2+} observed in the water chemical analyses can also originate from anthropogenic sources. Positive correlations of terrestrial calcium yield in rivers (Ca_{terr}) to the catchments aerial proportion of *managed lands* (LC1, table 22) hint to an influence by agricultural liming, as suggested by Raymond and Cole (2003) from analyses of subbasins in the

upper Mississippi basin. However, Ca_{terr} yield is also positively correlated to the proportion of *grasslands* (LC5), which are not expected to be subject to liming. Further, aerial proportions of carbonate-rich lithological classes (SC and SM) are also positively correlated to the proportions of LC1 and LC5. Atmospheric input corrected sodium yields (Na_{terr}) show a positive correlation to *urban area* (LC8) proportion of the catchments. This suggests a contribution of road salt, especially when combined with the correlation of atmospheric input corrected chloride (Cl_{terr}) yields to LC8. Correction of Na_{terr} by Cl_{terr}, as done before calculating Ca/Na ratios for excess calcium, reduces the correlation of Na^{2+} with LC8 (Table 22). Cl_{terr} yields, as well as atmospheric corrected potassium yields are positively correlated to the proportion of *managed lands* (LC1). This could hint to an influence of KCl-fertilizer as source for chloride in some regions.

However, although the observed correlations between cation flux and land cover class proportion hint to anthropogenic influence, the resoluteness of these hints is not strong regarding the correlations of lithological class proportion with land cover class proportion. Further, the type of influence determines the direction of bias in the modeled CO_2/HCO_3^- ratio. The artificial input of KCl would cause chloride yield to rise, thus reduce calculated Na_{sil}, via the correction for chloride (Using a Na_{terr}/Cl_{terr} ratio; compare chapter 4.2.3.2.2) and increase the amount of HCO_3^- yield that is attributed to carbonate contribution (because of excess-calcium calculation from Ca_{hco3}/Na_{sil} ratios). Application of halite as street salt, on the other hand, would add sodium and chloride in a ratio of 1:1, higher than the average correction (Table 17). Thus, it adds more sodium than is corrected for, and lowers the excess calcium. The exact correction factors of non-silicate sodium and bicarbonate counterbalanced calcium are highly unclear. Table 17 shows the resulting changes in the CO_2/HCO_3^- ratio for different correction scenarios. The highest difference between the correction of Na_{sil1}/Ca_{alkso4} (highest expected excess-calcium – lowest CO_2/HCO_3^- ratio of the five calculated scenarios) and $Na_{sil0731}/Ca_{alkclso4}$ (highest expected CO_2/HCO_3^- ratio) is 0.10 for the lithological class VB+. Additionally, a bias may be introduced into the CO_2/HCO_3^- correction by not distinguishing the HCO_3^- counterbalanced fraction of Na_{sil}. A comparison of CO_2/HCO_3^- ratios calculated using the HCO_3^- counterbalanced fraction of $Na_{sil0731}$ with the results of table 17 shows that the CO_2/HCO_3^- ratio for SS drops by 7 % for calculation with the HCO_3^- counterbalanced fraction of $Na_{sil0731}$. However, the ratios for VB+, VA+, PB+ and MTPA remain virtually constant (Δ_{max} =2 %). This stability suggests that even without knowing the very exact correction factors, a robust model result can be expected. Nevertheless, knowledge of correction factors of calculation of CO_2/HCO_3^- ratios should be improved in the future.

Table 22: Correlations of atmospheric corrected cation yields with land cover class proportions. For comparison correlations of lithological class proportions and land cover class proportions are given. Red coefficients are significant on the p<0.05 level.

	LC1	LC2	LC3	LC4	LC5	LC8
	Managed land	Broadleaved forest	Needle-leaved forest	Shrub-land	Grass-land	Urban area
Ca_{terr} 10^6 mol km^{-2} a^{-1}	**0.28**	-0.06	**-0.2**	**-0.19**	**0.17**	**0.13**
Cl_{terr} 10^6 mol km^{-2} a^{-1}	**0.24**	0.09	**-0.27**	**-0.13**	0.09	**0.4**
K_{terr} 10^6 mol km^{-2} a^{-1}	**0.28**	**0.15**	**-0.33**	**-0.21**	0.11	**0.24**
Na_{terr} 10^6 mol km^{-2} a^{-1}	**0.12**	0.09	**-0.17**	-0.03	0.03	**0.31** [A]
SC	**0.4**	-0.03	**-0.31**	**-0.15**	**0.26**	0.07
SM	**0.18**	**-0.14**	-0.1	-0.08	**0.25**	-0.03
SS	**-0.11**	**0.22**	-0.06	-0.08	-0.08	-0.05
SU+	0.08	-0.03	-0.08	0.04	0.1	0.05
MT	**-0.26**	**0.17**	**0.15**	-0.04	**-0.27**	0.04
PA	**-0.19**	-0.1	**0.2**	**0.22**	-0.08	-0.02
PB+	**-0.19**	**-0.13**	**0.3**	-0.03	**-0.16**	-0.02
VA+	**-0.17**	**-0.28**	**0.36**	**0.32**	**-0.19**	-0.06
VB+	**-0.19**	**-0.21**	**0.36**	**0.16**	**-0.22**	-0.11

[A] For comparison, correlation coefficients to LC8 for chloride-corrected Na_{sil} are r=-0.13 (p=0.017) for Na_{sil1}, r=-0.18 (p=0.7: insignificant) for $Na_{sil0858}$ and r=0.06 (p=0.24: insignificant) for $Na_{sil0731}$.

The approach to attribute all HCO_3^- flux from carbonate-rich lithological classes (SM and SC) and the excess-calcium from other lithological classes entirely to carbonate contribution is a conservative estimate. The similarities between the different sources of carbonate contribution (Lerman et al., 2007; Hartmann, 2009) and the small sensitivity of the CO_2/HCO_3^- in reaction to changing Na_{sil} and Ca_{hco3} corrections underscore the robustness of the approach to calculate the effects of carbonate on HCO_3^- fluxes. However, the uncertainty of exact correction factors should be considered when interpreting the model results.
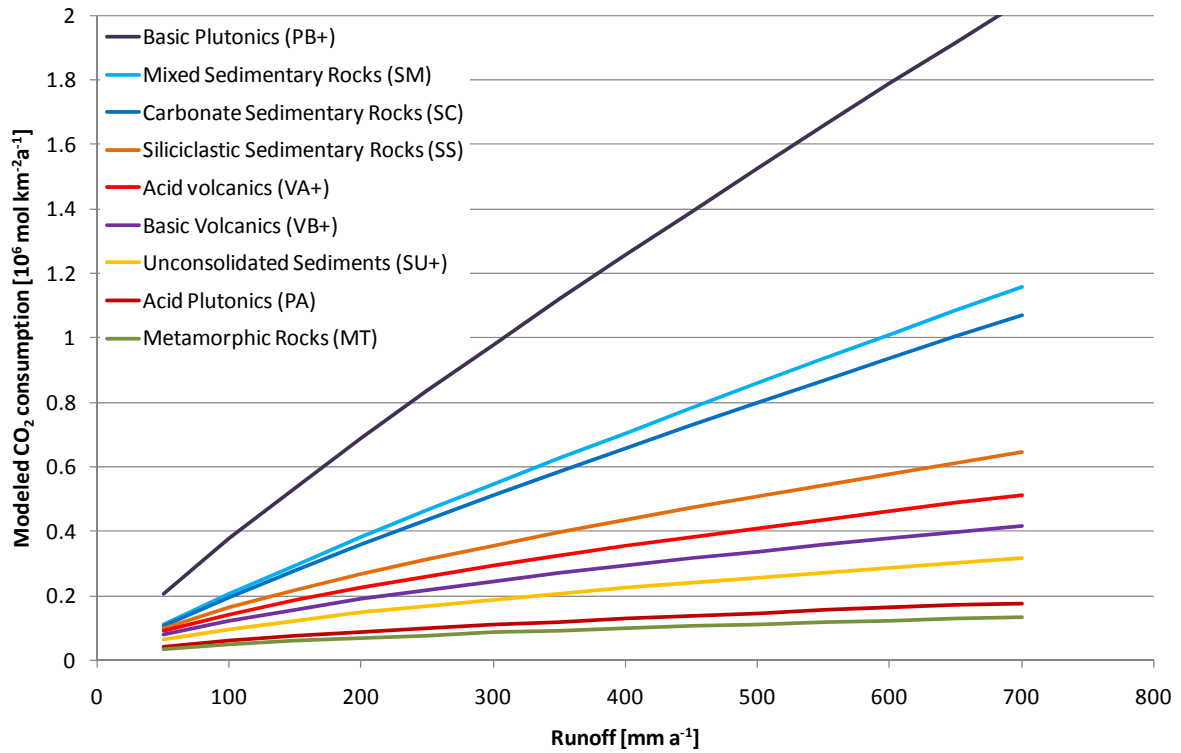
4.4.3 Comparison to previous CO₂ consumption models

Figure 27: Modeled CO₂ consumption per lithological class in dependence of runoff for the RoLiLc-model. As land cover impact factor, the average for the assessed catchments (1.51) has been assumed. Values for runoff smaller than 50 have not been plotted for visibility reasons.
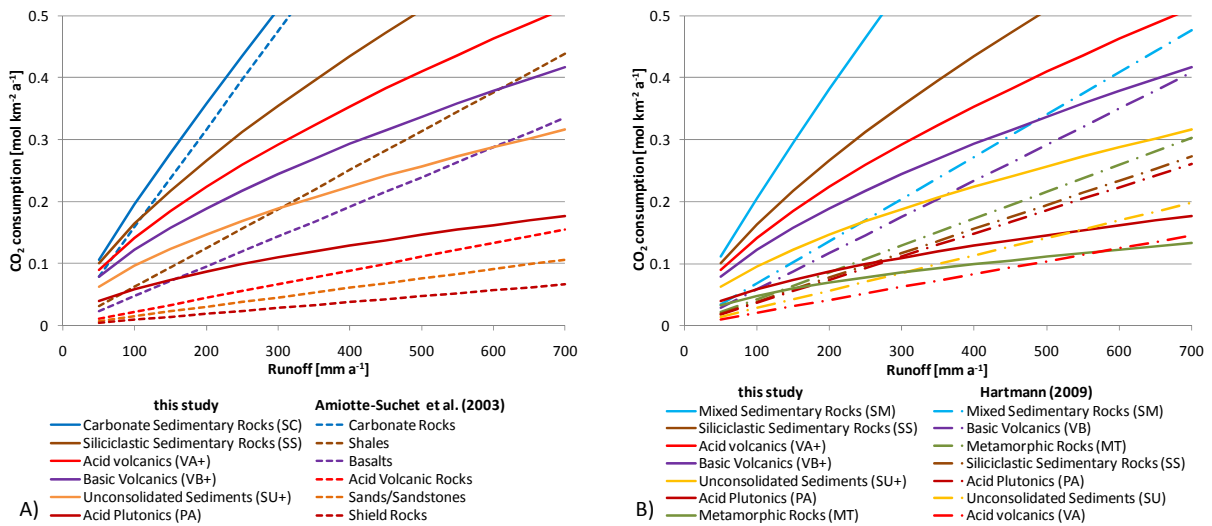

Figure 28: Comparison of the CO₂ consumption of corresponding lithological classes calculated using the RoLiLc-model and the equations by A) Amiotte-Suchet et al. (2003) and B) Hartmann et al. (2009, linear model). As land cover impact factor, the average of the assessed catchments (1.51) has been assumed. The order in the legend corresponds to the succession the lithological classes of each model with respect to their CO₂ consumption per runoff. Values for runoff smaller than 50 have not been plotted for visibility reasons.

The major change following the correction of CO_2/HCO_3^- ratios is that the CO_2 yield of carbonate-rich lithological classes (SM and SC) decreased relative to other lithological classes (Figure 27). The position of VB+ in the group of medium yielding lithology classes has not significantly changed. Still, SS and VA+ consume more CO_2 per runoff than VB+.

Figure 28 compares calculated CO_2 consumption of the here presented RoLiLc-model for different runoff values, lithological classes with yields calculated using the model equations of GEMS-CO2 (Amiotte-Suchet and Probst, 1993; Amiotte-Suchet et al., 2003) and a model calibrated on Japanese catchments by Hartmann (2009). The land cover impact factor for the RoLiLc-model is fixed to 1.51, the average of the assessed catchments (Compare chapter 4.4.1.3). Land cover impact factor fixation of the RoLiLc-model is necessary to make it result in a single value per runoff and lithology. However, if the land cover impact factor was 1 (e.g. for forested catchments), the resulting values would be 0.66 times as high as shown in Figure 28.

The comparison with the model results of the GEM-CO2 model, calibrated on data from catchments in France (based on data from Meybeck, 1986) shows a similar order of lithological class CO_2 consumption per runoff as the RoLiLc-model (Figure 28 A). Still, RoLiLc results in larger total CO_2 consumption per runoff (except for carbonate rocks and SC). The GEMS-CO2 model is calibrated with runoff data measured in the calibrating catchments, which Meybeck (1986) amounts to 268 mm a^{-1}. Thus the calibrating runoff seems to be in the same range for the GEM-CO2 model and the RoLiLc-model. However, the data from Meybeck originate mostly from forested catchments (Meybeck, 1987), which would consume only two thirds of the CO_2 than using the average land cover impact factor as applied for the RoLiLc-model (which is 1.51). Considering this, and considering that the GEMS-CO2 model is linear, both models would result in similar CO_2 consumption per lithological class and runoff.

The comparison with the Hartmann (2009) model shows that although predicting lower CO_2 consumption for small runoff values, the Hartmann (2009) model surpasses the CO_2 consumption predicted by the RoLiLc-model for higher runoff values (Figure 28 B). For the lithological classes MT and PA, the runoff value at which the Hartmann (2009) model surpasses the RoLiLc-model is about 130 mm a^{-1} and about 280 mm a^{-1}, respectively, for *basic volcanic rocks* (excluding pyroclastics in the Hartmann (2009) model) that runoff value is 700 mm a^{-1}. This effect can be attributed to the linear form of the Hartmann (2009) model compared to the exponential of the RoLiLc-model (with exponents smaller 1). However, additionally the average runoff in Japan is higher (1100 mm a^{-1} on average in Japan, compared to 260 mm on average used for North America), and the geologic evolution of the rocks very different to that in North America. Furthermore, the rank of lithological classes regarding their CO_2 consumption for a given runoff (Figure 28) is quite different for the

Hartmann (2009) model and the RoLiLc model, suggesting significantly different characteristics of rocks in both regions within lithological classes of the same name.

The comparison with the Hartmann CO_2 model (Hartmann, 2009) and the GEMS-CO2 model (Amiotte-Suchet and Probst, 1995; Amiotte-Suchet et al., 2003) points out the importance of regionally calibrating models and considering land cover influences.

4.4.4 Extrapolation to North America

Extrapolating the lumped models to a spatial explicit raster using the source data of the calibration of the lumped models needs to be validated in two ways. First, spatial explicit application of the lumped models needs to yield valid results for the calibration area. Second, the calibration area needs to adequately represent the extrapolation area.
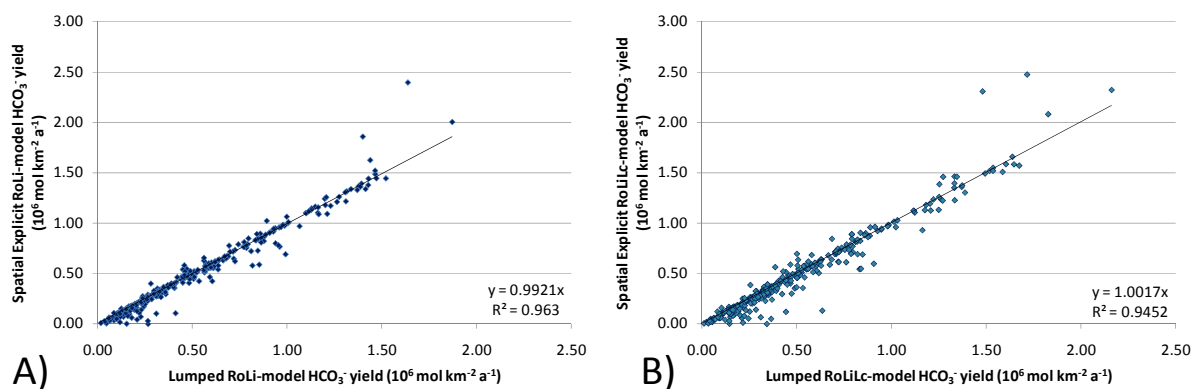
Figure 29: Comparison of lumped and spatial explicit application of the A) RoLi-model and B) RoLiLc-model. On the vertical axis, the average spatial explicit HCO_3^- yield for the 338 calibrating catchments is plotted, on the horizontal axis their yield as predicted by the lumped model.

The slope of a linear trend between lumped and spatial explicit results of the RoLi-model and RoLiLc-model for the calibrating catchments is 0.992 and 1.002, respectively (Figure 29 A and B). The trend correlation coefficients are r=0.98 and r=0.97, respectively. Thus, although spatial explicit results differ from lumped model predictions for single catchments, in general the trends suggest the validity of the spatial explicit application of the models.

The representativeness of the distribution of lithological and land cover classes within the calibrating area (338 catchments) for North America can be observed in figure 30 A and B. The distribution of lithological classes within the model calibration area is similar to that of North America. The main difference is an overrepresentation of sediments (SU+ and SS) and a corresponding underrepresentation of metamorphic and plutonic rocks (Figure 30 A). This is attributed to a lack of calibration catchments in northeastern North America (Compare figure 3 for distribution of lithological classes). However, both units are still represented in the calibration areas. Regarding land cover, the calibration dataset consists of considerably more *managed lands* (LC1) compared to the

entire North America (18.7 % versus 8.36 %; Figure 30 B) as well as more *needle leaved forest* (LC2; 28.9 % versus 22.1 %). *Grasslands* (LC5) are underrepresented in the calibration dataset (18.5 % versus 25.1 %). Despite the differences between the calibration area and North America, the calibration area in general represents the lithological classes and land cover classes occurring in North America.

However, both models show a tendency to underestimate low temperatures (Table 21). The average temperature of the calibrating area is higher than that of North America (8.4°C versus 1.63°C). This could lead to an underestimation of the results in the colder parts of North America, as the model is calibrated for warmer areas and model residuals show a negative trend for increasing temperatures (Table 21). Apart from the possible temperature bias, glaciation and permafrost are important factors to consider in far northern regions. However, not many studies assess the impact of those potential controlling factors of chemical weathering rates. For permafrost, studies emphasize the increased physical weathering intensity by frost shattering (Huh and Edmond, 1999) or high physical soil activity (Zakharova et al., 2005). They argue that these effects counteract the proposed lowering influence of low temperatures on weathering rates which would thus be not observable in CO_2 consumption (Huh and Edmond, 1999) and DSi fluxes (Zakharova et al., 2005). A similar effect of exposing fresh mineral surfaces to chemical weathering by grinding is attributed to glaciers (Reynolds and Johnson, 1972). However, sediment that was ground free by the glacier is transported and largely influences chemical weathering in downstream areas (Anderson et al., 1997; Anderson, 2007).

Considering these aspects, it is assumed that the extrapolation to North America is valid even though the calibrating areas are not representative concerning temperature. Nevertheless, measured data would be beneficial to validate the extrapolation in far-north regions.
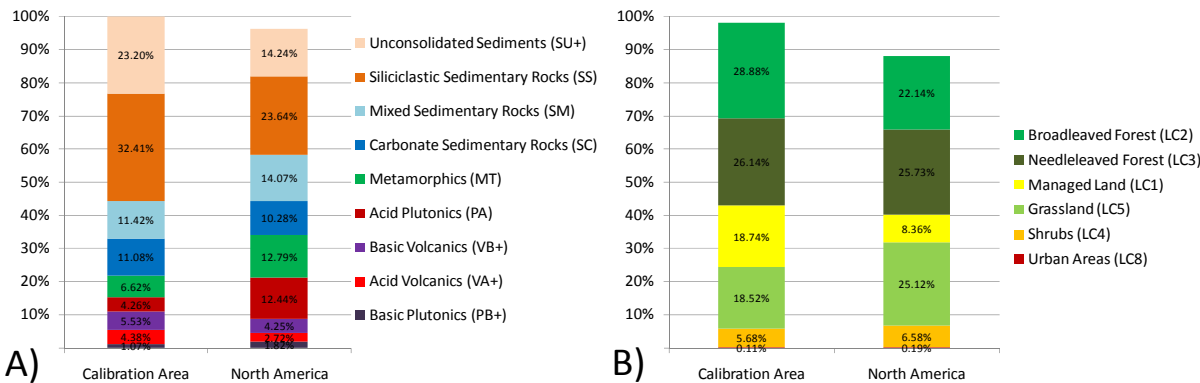
Figure 30: Comparison of A) lithological class and B) land cover proportions of the model calibration area and the area of North America. The part of the columns missing to 100 % is from other contributing classes not named in this comparison.

94
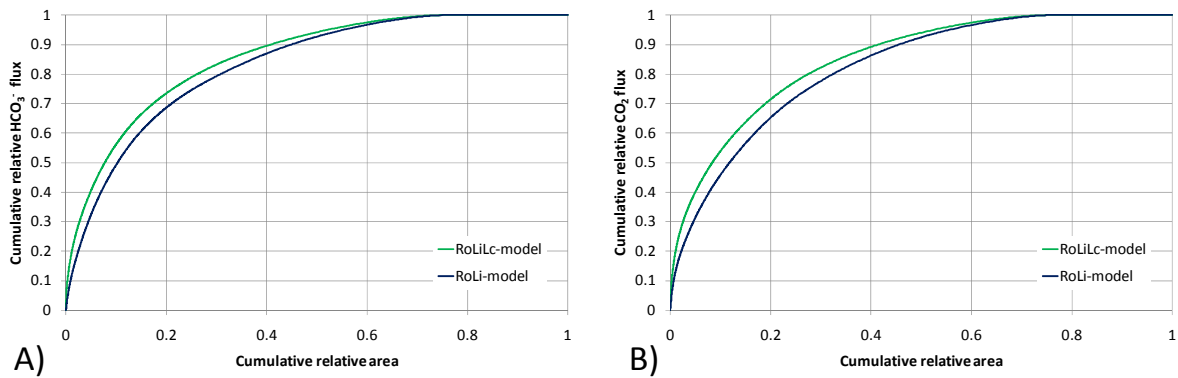
Figure 31: Contribution of highly active weathering areas to A) HCO$_3^-$ flux and B) CO$_2$ consumption in North America calculated by the RoLi-model (blue line) and RoLiLc-model (green line).

Analyses of the spatial explicit model extrapolations show that the influence of high yielding areas is large for both HCO$_3^-$ flux and CO$_2$ consumption in North America (Figure 31 A and B). Half of the HCO$_3^-$ flux and CO$_2$ consumption calculated by the RoLi-model are generated in 10.2 % and 11.8 % of the area of North America, respectively. The RoLiLc model is more sensitive to high-yielding areas; 7.7 % and 8.4 % of the area contribute half of the HCO$_3^-$ flux and CO$_2$ consumption from North America calculated by that model. The numbers closely resemble the 9.1 % of world surface area Hartmann et al. (2009) report to be responsible for 50 % of the world CO$_2$ consumption by chemical weathering. This similarity once more underscores the therein named importance of small regions with high HCO$_3^-$ yields that should not be neglected when including chemical weathering in modeling the global carbon cycle.

Comparing the RoLi-model and the RoLiLc-model reveals that although they draw the same general picture, differences exist in detail. The CO$_2$ consumption both models calculate for North America varies by about 3 % (RoLi-model: 50.0 10^6 t C a^{-1}; RoLiLc-model: 51.4 10^6 t C a^{-1}). This is expected, as both models are significant and their residuals are normally distributed for the calibrating catchments (Figure 16 A and C). However, it is a further indicator that the calibrating catchments represent North America sufficiently. Both models show a similar pattern of high yielding regions (Figures 19 and 21). However, CO$_2$ consumption by chemical weathering calculated using the RoLiLc-model shows a higher spatial variability, due to high spatial variability in land cover. Most areas are predicted to consume slightly less CO$_2$ according to the RoLiLc-model than the RoLi-model (Figure 32). Nevertheless, some areas, especially in northern latitudes and south of the great lakes, show an increase in CO$_2$ consumption predicted by the RoLiLc-model compared to the RoLi-model. A very large increase of CO$_2$-fluxes can, of course, be observed for urban areas (LC8; figure 32). Although, they only cover 0.19 aerial % of North America, urban areas contribute 6 % of the CO$_2$ flux predicted by the RoLiLc-model. Whether these 3.1 10^6 t C a^{-1} can be accounted for as "consumed" from atmospheric/soil CO$_2$ depends on its origin, which cannot be determined by the presented model.

95

For simplicity, the term "CO_2 consumption" will be also used for the RoLiLc-model; however, regarding the CO_2 fluxes from urban areas, this term might be an overestimation.
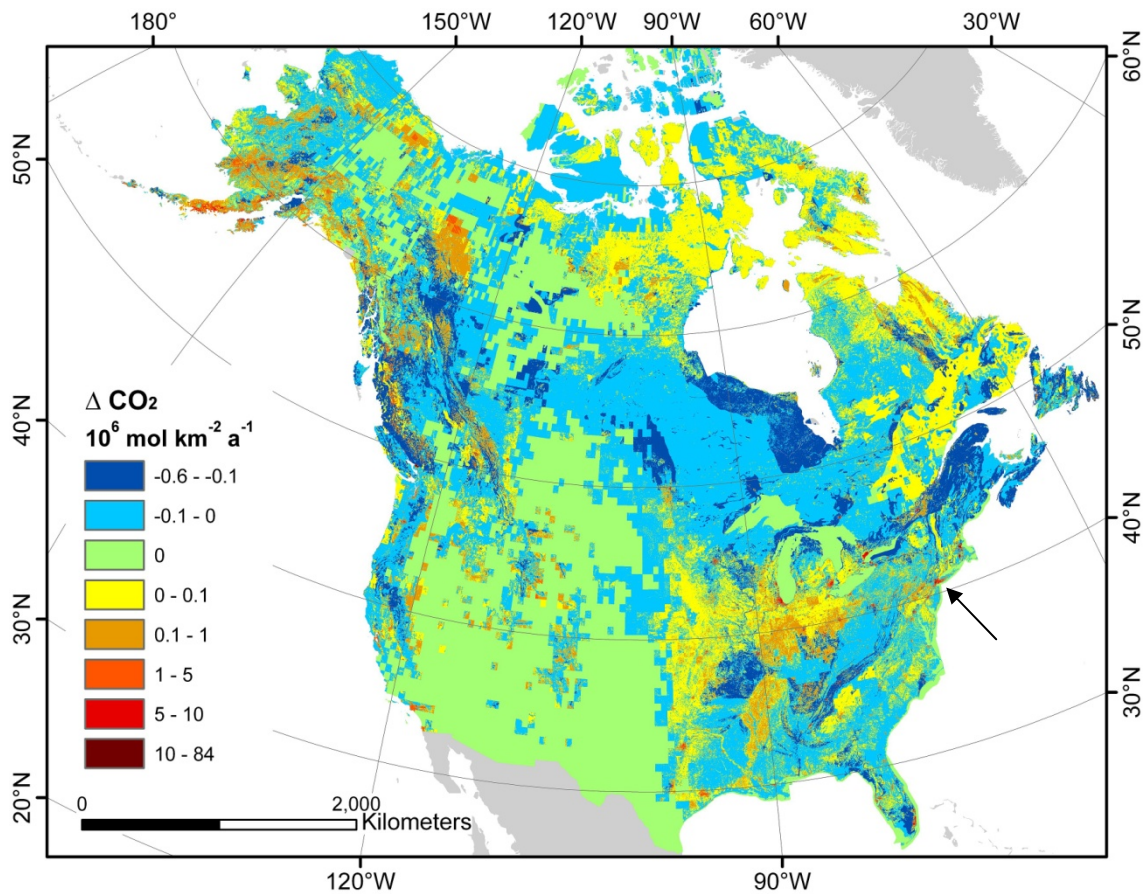
Figure 32: Difference of calculated CO_2 yield using the RoLiLc-model and the RoLi-model. Positive values indicate that the RoLiLc-model results in higher fluxes than the RoLi-model. Differences for urban areas (LC8) are especially high; as an example New York is highlighted with an arrow.

The about 50 10^6 t C a^{-1} calculated to be consumed by weathering by both models amount to 19 % or 21 % of the worldwide CO_2 consumption by chemical weathering calculated by Amiotte-Suchet et al. (2003) or Hartmann et al. (2009), respectively. Related to its proportion on world area, the CO_2 consumption rate in North America is elevated by 33 %-45 % compared to the global CO_2 consumption rate by chemical weathering (Table 23).

Table 23: Comparison of the RoLi-model and RoLiLc-model from this study with global studies on CO_2 consumption.

	This study: RoLi-model	This study: RoLiLc-model	Hartmann et al. (2009)	Amiotte-Suchet et al. (2003)
Extrapolation area	North America	North America	Wld. Exorheic	World
Average specific CO_2 consumption (10^6 mol km^{-2} a^{-1})	0.21	0.22	0.17	0.16
Total C flux (10^{12} mol a^{-1})	4.2	4.3	19.7	21.5
Total C flux (10^6 t a^{-1})	50	51	237	258

4.4.5 Model reliability

The presented models for HCO_3^- flux and CO_2 consumption are calibrated with catchments exhibiting little anthropogenic impact. However, some water bodies may be within the catchment areas and affect, most likely reduce, the bicarbonate concentration used for calculation of CO_2 consumption. Even in-river carbonate precipitation has been shown to significantly reduce HCO_3^- concentrations (Szramek and Walter, 2004). In-river HCO_3^- loss would cause the presented model to underestimate the calculated carbon fluxes from the terrestrial into the fluvial system.

Results of CO_2 consumption in relation to HCO_3^- fluxes are sensitive to the correction of carbonate contributions from non-carbonate lithological classes, which in turn is sensitive to the Ca/Na elemental ratios in the weathering product (water) and the educt (source rocks). The Ca/Na elemental ratios in water are sensitive to correction of non-silicate weathering sodium inputs (Table 17). However, to correct for the amount of sodium that does not stem from silicate weathering proved to be complicated (Compare chapter 4.2.2). Further, the ratios of Ca/Na in both source rock and water show strong regional variations. Thus, the correction for non-silicate weathering introduced sodium remains an uncertain factor in the model. In the matrix of assumed likely correction ratios (Table 17), the corrections induce variance in the CO_2/HCO_3^- ratio of up to about 10 %.

4.5 Conclusions from the CO₂-models

The presented multilithological models of HCO_3^- fluxes and CO_2 consumption by chemical weathering result in a CO_2 consumption of $50.00 \ 10^6$ t C a^{-1} (RoLi-model) or $51.39 \ 10^6$ t C a^{-1} (RoLiLc-model) in North America. This equals a specific consumption of about $0.2 \ 10^6$ mol CO_2 km^{-2} a^{-1}, 33-45 % above the world average (Amiotte-Suchet et al., 2003; Hartmann et al., 2009 for exorheic regions).

A comparison of HCO_3^- models using different predictors shows that the combination of runoff and lithology performs well in describing the HCO_3^- yields. However, including land cover classes in the model adds to model performance. The highest yielding lithological classes are carbonate-rich sedimentary rocks (SC, SM) and *basic plutonic rocks* (PB+), followed by *siliciclastic sedimentary rocks* (SS), *acid* and *basic volcanic rocks* (VA+, VB+), *acid plutonic rocks* (PA), *unconsolidated sediments* (SU+) and *metamorphic rocks* (MT). Of the assessed land cover classes, *urban areas* (LC8) show extraordinary high HCO_3^- yields, followed by *shrubs* (LC4), *grasslands* (LC5) and *managed lands* (LC1).

The method of using Ca/Na elemental ratios to correct for excess-calcium contributions to HCO_3^- fluxes from non-carbonate lithological classes, introduced by Hartmann (2009), has been applied and extended for the area of North America. It was shown that the used Ca/Na ratios are sensitive to corrections of non-silicate weathering derived sodium and calibration sample selection. Applying the

range of likely realized corrections for non-silicate weathering derived sodium results in differences in the atmospheric/soil CO_2 proportion on modeled HCO_3^- fluxes of about 10 %. Carbonate-rich lithological classes (SM and SC) are per definition attributed a CO_2/HCO_3^- ratio of 0.5, neglecting possible silicate mineral weathering induced HCO_3^- flux. *Basic plutonic rocks* (PB+), *acid* (VA+) and *basic volcanic rocks* (VB+) show no or little modeled carbonate contribution to their HCO_3^- fluxes; the modeled CO_2/HCO_3^- ratios are close to 1. Modeled carbonate contributions to HCO_3^- fluxes from siliciclastic sediments (SS and SU+) results in CO_2/HCO_3^- ratios of 0.93 and 0.83, respectively. The CO_2/HCO_3^- ratio of 0.63 for *metamorphic* and *acid plutonic rocks* (MT and PA) is the lowest ratio for not carbonate-rich lithological classes. Especially for the latter two lithological classes, carbonate contributions should not be neglected. The similarity of the CO_2/HCO_3^- ratios from this study compared to CO_2/HCO_3^- ratios calibrated in Japan by Hartmann (2009) suggests the general robustness of the approach. Significant differences in CO_2 consumption per runoff for different lithological classes compared to literature values highlight the importance of regionally calibrating large scale models and applying high resolution geodata (cf. Amiotte-Suchet and Probst, 1993; Amiotte-Suchet et al., 2003; Hartmann, 2009). The significant influence of land cover found in the here presented models should be considered in future models of large scale CO_2 consumption.

Spatial explicit extrapolation of the models underscores the conclusions of Hartmann et al. (2009) that small regions contribute large proportions of the total CO_2 consumption. In North America, the models suggest that 8.4 – 11.8 % (depending on the applied model) of the area account for 50 % of the CO_2 consumption by chemical weathering. To sufficiently represent these small areas is important for earth system models (ESM); yet this is difficult considering the resolutions of typical ESM are 2° to 3.75°. However, the presented extrapolation (with a grid size of 0.04 km²) uses only binary lithology information per cell. If this was extended to information on the proportion per lithological class per cell for ESM, their representation of small but highly contributing regions could be improved. Further, lithological classes are clustered in the presented models regarding their CO_2 consumption in dependence of runoff. This suggests that the use of a smaller number of classes in ESM may be adequate to represent the CO_2 consumptions per lithological class. However, further research is needed to approach the problem to appropriately translate scale sensitive information, e.g., lithology, to coarse scale datasets.

5 Concluding remarks

The presented work consists of three parts which will be summarized below, followed by implications for future research.

The first part of the work is the development of a high resolution lithological map of North America to be used as a tool for regional scale modeling. 17 geological maps were assembled and combined with 43 references for lithology information. The new lithological map consists of 262 111 polygons, with an average size of 75 km². This amounts to 178 times as many represented geological features than in the most advanced comparable map (Dürr et al., 2005). The features are grouped into lithological classes of three independent levels. 19 major lithological classes are defined, further detailed by 8+11 minor classes (Table 2). However, lithological classes always aggregate different rock types. The definition precision of this aggregate depends on spatial resolution and data quality. Comparison with existing maps highlights large differences in the distribution of lithological classes in North America. The comparison suggests that lithological classes from different maps comprise different rocks, even if they have the same name. Thus, mixing inconsistent lithological information sources into one model, e.g., by calibrating on one map and applying the model to another, shout be treated with great care.

The second part consists of the calibration and development of a large scale model for dissolved silica (DSi) mobilization by chemical rock weathering in the conterminous USA. The DSi model was calibrated on 142 river catchments applying the new map and using a multilithological approach originally introduced and tested for the Japanese Archipelago (Hartmann et al., 2010). The calibrating catchments were chosen for small anthropogenic and water body impacts. The model predicts the observed DSi yields in the calibration catchments well (r=0.94) by using the predictors runoff and lithology only. Apart from reconfirming the importance of basic igneous rocks (PB+, VB+) for DSi mobilization known from previous studies (Bluth and Kump, 1994; Hartmann et al., 2010), the DSi model found carbonate-rich lithological classes (SC and SM) to be important contributors for DSi yields.

Further comparisons with existing DSi mobilization models (Bluth and Kump, 1994; Hartmann et al., 2010) revealed some differences for the contribution of individual lithological classes. This is in part attributed to regional variations in geological settings and suggests the importance of regional calibration of large scale models. Apart from runoff and lithology the DSi model shows significant trends of relative model residuals with land cover and temperature. Although those trends suggest a control of these factors of DSi mobilization by chemical weathering, they could not be included into the model equations as significant predictors.

In the third part, a model for consumption of atmospheric/soil CO_2 by chemical weathering is presented. It uses the same techniques as the DSi model for predicting fluvial HCO_3^- fluxes and is calibrated on 338 catchments with low anthropogenic impact. Correction of HCO_3^- fluxes for carbonate contribution is necessary to quantify CO_2 consumption. In addition to contributions of carbonate-rich lithological classes (classes SM and SC), carbonate contributions from silicate dominated lithological classes were corrected, using Ca/Na elemental ratios as introduced by Hartmann (2009). Calculation of those ratios is complicated by a number of possible Ca or Na sources (e.g. street salt).

Two models for HCO_3^- are developed that are later corrected for carbonate contributions. One model uses runoff and lithology, the second adds land cover, as predictors for HCO_3^- flux and thus CO_2 consumption. Carbonate-rich lithological classes consume most CO_2 per runoff due to their low resistance to weathering. However, *basic plutonic rocks* are also predicted to exhibit a large CO_2 consumption per runoff. In contrast, *basic volcanic rocks* follow in a group of lithological classes consuming less CO_2 per runoff. The model incorporating land cover classes as predictors shows HCO_3^- fluxes to increase with *urban areas*, *shrublands*, *grasslands* and *managed lands*. For the first time, land cover is included as a predictor into a multilithological forward model for CO_2 consumption by chemical weathering. Although prediction quality of the models for HCO_3^- flux is high (r=0.80 and 0.84), correction for carbonate contribution from predominantly silicate lithological classes contains significant uncertainties. A comparison of different reasonable Ca/Na ratios for correction shows a variation of CO_2/HCO_3^- ratios of up to 10 % for individual lithological classes. The extrapolation of the models results in a total CO_2 consumption of 50.0 10^6 t C a^{-1} for the model using runoff and lithology as predictors and 51.4 10^6 t C a^{-1} for the model additionally using land cover. Both models draw the same general picture but show some variances in detail. The models show the importance of the northern Rocky Mountains for CO_2 consumption and that of small, highly active areas in general. Depending on the applied model, 8.4 % to 11.8 % of the area of North America are responsible for 50 % of the total CO_2 consumption.

Although their prediction quality is high, the presented models only resolve lateral fluxes. A large step towards integrating known processes into empirical models would be to allow for more dimensions. To split shallow from deep runoff would enable future models to differentiate between controlling factors that dominate on the surface, e.g., land cover, and those that dominate deeper flows, like lithology. Moreover, while the presented models are based on data of detail unmatched by other studies on this spatial extend, only one data value per monitoring station is used that is assumed to represent a long-term average. Increasing the temporal resolution could allow models to resolve seasonal changes. Additionally, the presented approach assumes the assessed systems to be

in a steady-state, which requires the systems parameters to be fairly constant. Although in the observed timeframe of decades, this may be the case for some parameters, e.g. lithology and slope, land cover or temperature may change in that time. Thus, the necessary simplification to assume a steady state may not be valid in all cases. Future models might allow these parameters to change to assess unsteady state conditions.

In summary, although the presented models already allow for extensive interpretations regarding processes influencing dissolved elementary fluxes, it is still a long way to go until confinement of nature's complexity into one global scale model.

6 Acknowledgements

7 References

Aalto, R., Dunne, T. and Guyot, J.L., 2006. Geomorphic controls on Andean denudation rates. Journal of Geology 114 (1), 85-99.

Abu Ghazleh, S., Hartmann, J., Jansen, N. and Kempe, S., 2009. Water input requirements of the rapidly shrinking Dead Sea. Naturwissenschaften 96 (5), 637-643.

Ahnert, F., 1970. Functional Relationships between Denudation, Relief, and Uplift in Large Mid-Latitude Drainage Basins. American Journal of Science 268 (3), 243-263.

Alexander, R.B., Ludtke, A.S., Fitzgerald, K.K. and Schertz, T.L., 1996. Data from Selected U.S. Geological Survey National Stream Water-Quality Monitoring Networks (WQN) on CD-ROM, US Geological Survey, Reston.

Alexandre, A., Meunier, J.D., Colin, F. and Koud, J.M., 1997. Plant impact on the biogeochemical cycle of silicon and related weathering processes. Geochimica et Cosmochimica Acta 61 (3), 677-682.

Amiotte-Suchet, P. and Probst, J.L., 1993. Modeling of Atmospheric CO_2 Consumption by Chemical-Weathering of Rocks - Application to the Garonne, Congo and Amazon Basins. Chemical Geology 107 (3-4), 205-210.

Amiotte-Suchet, P. and Probst, J.L., 1995. A Global-Model for Present-Day Atmospheric Soil CO_2 Consumption by Chemical Erosion of Continental Rocks (GEM-CO2). Tellus Series B-Chemical and Physical Meteorology 47 (1-2), 273-280.

Amiotte-Suchet, P., Probst, J.L. and Ludwig, W., 2003. Worldwide distribution of continental rock lithology: Implications for the atmospheric/soil CO_2 uptake by continental weathering and alkalinity river transport to the oceans. Global Biogeochemical Cycles 17 (2), GB1038.

Anderson, S.P., 2007. Biogeochemistry of glacial landscape systems. Annual Review of Earth and Planetary Sciences 35, 375-399.

Anderson, S.P., Drever, J.I. and Humphrey, N.F., 1997. Chemical weathering in glacial environments. Geology 25 (5), 399-402.

April, R., Newton, R. and Truettner-Coles, L., 1986. Chemical weathering in two Adirondack watersheds: Past and present-day rates. Geological Society of America Bulletin 97 (10), 1232-1238.

Arino, O., Gross, D., Ranera, F., Bourg, L., Leroy, M., Bicheron, P., Latham, J., Di Gregorio, A., Brockman, C., Witt, R., Defourny, P., Vancutsem, C., Herold, M., Sambale, J., Achard, F., Durieux, L., Plummer, S. and Weber, J.-L., 2007. GlobCover: ESA service for global land cover from MERIS, Proceedings of the International Geoscience and Remote Sensing Symposium (IGARSS) 2007. IEEE International, Barcelona, 2412 - 2415.

Arrhenius, S., 1896. On the influence of cabonic acid in the air upon the temperature of the ground. Philosophical Magazine, Fith Series 4, 237-276.

Aspler, L.B. and Chiarenzelli, J.R., 1997. Initiation of similar to 2.45-2.1 Ga intracratonic basin sedimentation of the Hurwitz Group, Keewatin Hinterland, Northwest Territories, Canada. Precambrian Research 81 (3-4), 265-297.

Baker, A., Cumberland, S. and Hudson, N., 2008. Dissolved and total organic and inorganic carbon in some British rivers. Area 40 (1), 117-127.

Balogh-Brunstad, Z., Keller, C.K., Bormann, B.T., O'Brien, R., Wang, D. and Hawley, G., 2008. Chemical weathering and chemical denudation dynamics through ecosystem development and disturbance. Global Biogeochemical Cycles 22 (1), GB1007.

Barnes, R.T. and Raymond, P.A., 2009. The contribution of agricultural and urban activities to inorganic carbon fluxes within temperate watersheds. Chemical Geology 266 (3-4), 327-336.

Bartoli, F., 1983. The biogeochemical cycle of silicon in two temperate forest ecosystems. Ecological Bulletins (35), 469-476.

Batjes, N.H., 2006. ISRIC-WISE derived soil properties on a 5 y 5 ardcminutes global grid (ver. 1.1), ISRIC - World Soil Information, Wageningen.

Beikman, H.M., 1980. Geologic Map of Alaska. U.S. Geological Survey.

Berg, A. and Banwart, S.A., 2000. Carbon dioxide mediated dissolution of Ca-feldspar: implications for silicate weathering. Chemical Geology 163 (1-4), 25-42.

Berner, R.A., 1995. Chemical weathering and its effect on atmospheric CO_2 and climate. Chemical Weathering Rates of Silicate Minerals 31, 565-583.

Berner, R.A. and Kothavala, Z., 2001. GEOCARB III: A revised model of atmospheric CO_2 over phanerozoic time. American Journal of Science 301 (2), 182-204.

Berner, R.A., Lasaga, A.C. and Garrels, R.M., 1983. The carbonate-silicate geochemical cycle and its effect on atmospheric carbon-dioxide over the past 100 million years. American Journal of Science 283 (7), 641-683.

Bettis, E.A., Muhs, D.R., Roberts, H.M. and Wintle, A.G., 2003. Last glacial loess in the conterminous USA. Quaternary Science Reviews 22 (18-19), 1907-1946.

Beusen, A.H.W., Bouwman, A.F., Dürr, H.H., Dekkers, A.L.M. and Hartmann, J., 2009. Global patterns of dissolved silica export to the coastal zone: Results from a spatially explicit global model. Global Biogeochemical Cycles 23, GB0A02.

Blackadar, R.G., Davison, W.L. and Trettin, H.P., 1968. Geology Moffet Inlet-Fitzgerald Bay, District of Franklin. Geological Survey of Canada.

Blecker, S.W., McCulley, R.L., Chadwick, O.A. and Kelly, E.F., 2006. Biologic cycling of silica across a grassland bioclimosequence. Global Biogeochemical Cycles 20 (3), GB3023.

Blum, A.E., 1994. Feldspars in weathering. In: I. Parsons (Ed.), Feldspars and their reactions. NATO ASI Series C. Kluwer Academic Publishers, Dordrecht, 595-630.

Blum, J.D., Klaue, A., Nezat, C.A., Driscoll, C.T., Johnson, C.E., Siccama, T.G., Eagar, C., Fahey, T.J. and Likens, G.E., 2002. Mycorrhizal weathering of apatite as an important calcium source in base-poor forest ecosystems. Nature 417 (6890), 729-731.

Blume, H.-P., 1996. Böden städtisch-industrieller Verdichtungsräume. In: H.-P. Blume (Ed.), Handbuch der Bodenkunde. Ecomed, Landsberg, Chapter 3.4.4.9.

Bluth, G.J.S. and Kump, L.R., 1991. Phanerozoic paleogeology. American Journal of Science 291 (3), 284-308.

Bluth, G.J.S. and Kump, L.R., 1994. Lithologic and climatologic controls of river chemistry. Geochimica et Cosmochimica Acta 58 (10), 2341-2359.

Boeglin, J.L. and Probst, J.L., 1998. Physical and chemical weathering rates and CO_2 consumption in a tropical lateritic environment: the upper Niger basin. Chemical Geology 148 (3-4), 137-156.

Bolin, B., Degens, E.T., Kempe, S. and Ketner, P., 1979. The global carbon cycle - Scope Report 13. Unwin Brothers, Surrey, pp. 491.

Bonneville, S., Smits, M.M., Brown, A., Harrington, J., Leake, J.R., Brydson, R. and Benning, L.G., 2009. Plant-driven fungal weathering: Early stages of mineral alteration at the nanometer scale. Geology 37 (7), 615-618.

Bootsma, H.A., Hecky, R.E., Johnson, T.C., Kling, H.J. and Mwita, J., 2003. Inputs, outputs, and internal cycling of silica in a large, tropical lake. Journal of Great Lakes Research 29, 121-138.

Bowser, C.J. and Jones, B.F., 2002. Mineralogic controls on the composition of natural waters dominated by silicate hydrolysis. American Journal of Science 302 (7), 582-662.

Brady, P.V. and Carroll, S.A., 1994. Direct effects of CO_2 and temperature on silicate weathering - possible implications for climate control. Geochimica et Cosmochimica Acta 58 (7), 1853-1856.

Brady, P.V., Dorn, R.I., Brazel, A.J., Clark, J., Moore, R.B. and Glidewell, T., 1999. Direct measurement of the combined effects of lichen, rainfall, and temperature on silicate weathering. Geochimica et Cosmochimica Acta 63 (19-20), 3293-3300.

Brady, P.V. and Walther, J.V., 1989. Controls on silicate dissolution rates in neutral and basic pH solutions at 25-degrees-C. Geochimica et Cosmochimica Acta 53 (11), 2823-2830.

Brantley, S.L., Goldhaber, M.B. and Ragnarsdottir, K.V., 2007. Crossing disciplines and scales to understand the Critical Zone. Elements 3 (5), 307-314.

Broecker, W.S., 1982. Glacial to interglacial changes in ocean chemistry. Progress in Oceanography 11 (2), 151-197.

Buschkuehle, M., 2003. Sedimentology and stratigraphy of middle and upper devonian carbonates in northern Alberta: A contribution to the carbonate-hosted Pb-Zn (MVT) targeted geoscience initiative. EUB/AGS Geo-Note 2002-14, Alberta Geologial Survey.

Cannon, W.F., Kress, T.H., Sutphin, D.M., Morey, G.B., Meints, J. and Barber-Delach, R., 1999. Digital geologic map and mineral deposits of the lake superior region USGS Open-File Report. U.S. Geological Survey.

Chadwick, O.A., Derry, L.A., Vitousek, P.M., Huebert, B.J. and Hedin, L.O., 1999. Changing sources of nutrients during four million years of ecosystem development. Nature 397 (6719), 491-497.

CIESIN and CIAT, 2005. Gridded population of the world version 3 (GPWv3): Population grids, http://sedac.ciesin.columbia.edu/gpw, accessed on 20. July 2007.

Clark, J.F., Simpson, H.J., Bopp, R.F. and Deck, B., 1992. Geochemistry and loading history of phosphate and silicate in the Hudson estuary. Estuarine Coastal and Shelf Science 34 (3), 213-233.

Clarke, F.W., 1924. The data of geochemistry. U.S. Geological Survey Bulletin, 770. Government Press, Washington D.C:, pp. 841.

Collins, M.B., 1981. Sediment yield studies of headwater catchments in Sussex, Se England. Earth Surface Processes and Landforms 6 (6), 517-539.

Conley, D.J., 2002. Terrestrial ecosystems and the global biogeochemical silica cycle. Global Biogeochemical Cycles 16 (4), GB1121.

Conley, D.J., Likens, G.E., Buso, D.C., Saccone, L., Bailey, S.W. and Johnson, C.E., 2008. Deforestation causes increased dissolved silicate losses in the Hubbard Brook Experimental Forest. Global Change Biology 14 (11), 2548-2554.

Conley, D.J., Schelske, C.L. and Stoermer, E.F., 1993. Modification of the biogeochemical cycle of silica with eutrophication. Marine Ecology-Progress Series 101 (1-2), 179-192.

Coynel, A., Schafer, J., Hurtrez, J.E., Dumas, J., Etcheber, H. and Blanc, G., 2004. Sampling frequency and accuracy of SPM flux estimates in two contrasted drainage basins. Science of the Total Environment 330 (1-3), 233-247.

Dahlgren, R.A., Ugolini, F.C. and Casey, W.H., 1999. Field weathering rates of Mt. St. Helens tephra. Geochimica et Cosmochimica Acta 63 (5), 587-598.

Dai, A.G., Qian, T.T., Trenberth, K.E. and Milliman, J.D., 2009. Changes in continental freshwater discharge from 1948 to 2004. Journal of Climate 22 (10), 2773-2792.

Dalai, T.K., Krishnaswami, S. and Sarin, M.M., 2002. Major ion chemistry in the headwaters of the Yamuna river system: Chemical weathering, its temperature dependence and CO_2 consumption in the Himalaya. Geochimica et Cosmochimica Acta 66 (19), 3397-3416.

DeMaster, D.J., 1981. The supply and accumulation of silica in the marine environment. Geochimica et Cosmochimica Acta 45 (10), 1715-1732.

Derry, L.A., Kurtz, A.C., Ziegler, K. and Chadwick, O.A., 2005. Biological control of terrestrial silica cycling and export fluxes to watersheds. Nature 433 (7027), 728-731.

Dessert, C., Dupre, B., Gaillardet, J., Francois, L.M. and Allegre, C.J., 2003. Basalt weathering laws and the impact of basalt weathering on the global carbon cycle. Chemical Geology 202 (3-4), 257-273.

Dicken, C.L., Nicholson, S.W., Horton, J.D., Foose, M.P. and Mueller, J.A.L., 2005a. Integrated Geologic Map Databases for the United States: Alabama, Florida, Georgia, Mississippi, and South Carolina, U.S. Geological Survey Open-File Report.

Dicken, C.L., Nicholson, S.W., Horton, J.D., Foose, M.P. and Mueller, J.A.L., 2007. Integrated Geologic Map Databases for the United States: Alabama, Florida, Georgia, Mississippi, North Carolina, and South Carolina, U.S. Geological Survey Open-File Report.

Dicken, C.L., Nicholson, S.W., Horton, J.D., Kinney, S.A., Gunther, G., Foose, M.P. and Mueller, J.A.L., 2005b. Integrated Geologic Map Databases for the United States: Delaware, Maryland, New York, Pennsylvania, and Virginia, U.S. Geological Survey Open-File Report. U. S. Geological Survey.

Douglas, R.J.W., Gabrielse, H., Wheeler, J.O., Stott, D.F. and Belyea, H.R., 1970. Geology of Western Canada, Geology and Economic Minerals of Canada. Geological Survey of Canada, 364-488.

Douglas, R.J.W., Norris, A.W. and Norris, D.K., 1974. Geology, Great Slave, District of Mackenzie. Geological Survey of Canada.

Drever, J.I., 1994. The effect of land plants on weathering rates of silicate minerals. Geochimica et Cosmochimica Acta 58 (10), 2325-2332.

Drever, J.I. and Hurcomb, D.R., 1986. Neutralization of atmospheric acidity by chemical-weathering in an alpine drainage-basin in the North Cascade Mountains. Geology 14 (3), 221-224.

Drever, J.I. and Zobrist, J., 1992. Chemical weathering of silicate rocks as a function of elevation in the southern Swiss Alps. Geochimica et Cosmochimica Acta 56 (8), 3209-3216.

Dürr, H.H., Meybeck, M. and Dürr, S.H., 2005. Lithologic composition of the Earth's continental surfaces derived from a new digital map emphasizing riverine material transfer. Global Biogeochemical Cycles 19 (4), GB4S10.

Dürr, H.H., Meybeck, M., Hartmann, J., Laruelle, G.G. and Roubeix, V., 2009. Global spatial distribution of natural riverine silica inputs to the coastal zone. Biogeosciences Discussions 6, 1345-1401.

Eckhardt, F.E.W., 1979. Über die Einwirkung heterotropher Mikroorganismen auf die Zersetzung silikatischer Minerale. Zeitschrift für Pflanzenernährung und Bodenkunde 142 (3), 434-445.

Edmond, J.M., Palmer, M.R., Measures, C.I., Grant, B. and Stallard, R.F., 1995. The fluvial geochemistry and denudation rate of the Guayana Shield in Venezuela, Colombia, and Brazil. Geochimica et Cosmochimica Acta 59 (16), 3301-3325.

Environment Canada Pacific and Yukon Water Quality Monitoring and Surveillance Division, 2008. Pacific and Yukon ENVIRODAT database, http://waterquality.ec.gc.ca/, accessed on 25 March 2009.

Epstein, E., 1994. The anomaly of silicon in plant biology. Proceedings of the National Academy of Sciences of the United States of America 91 (1), 11-17.

Epstein, E., 1999. Silicon. Annual Review of Plant Physiology and Plant Molecular Biology 50, 641-664.

Ernst, R.E. and Buchan, K.L., 2004. Igneous rock associations in Canada 3. Large Igneous Provinces (LIPs) in Canada and adjacent regions: 3 Ga to present. Geoscience Canada 31 (3), 103-126.

ESRI, 2008. Data & Maps 9.3. ESRI Geoinformatik GmbH, Kranzberg.

Fekete, B.M., Vörösmarty, C.J. and Grabs, W., 2000. Global, composite runoff fields based on observed river discharge and simulated water balances, http://www.grdc.sr.unh.edu/, accessed on 11. January 2006.

Fekete, B.M., Vörösmarty, C.J. and Grabs, W., 2002. High-resolution fields of global runoff combining observed river discharge and simulated water balances. Global Biogeochemical Cycles 16 (3), GB1042.

Fraysse, F., Pokrovsky, O.S. and Meunier, J.D., 2009. Experimental study of terrestrial plant litter interaction with aqueous solutions. Geochimica et Cosmochimica Acta 74 (1), 70-84.

Frazier, W.J. and Schwimmer, D.R., 1987. Regional Stratigraphy of North America. Plenum Press, New York, pp. 719.

Fulweiler, R.W. and Nixon, S.W., 2005. Terrestrial vegetation and the seasonal cycle of dissolved silica in a southern New England coastal river. Biogeochemistry 74 (1), 115-130.

Gaillardet, J., Dupre, B., Louvat, P. and Allegre, C.J., 1999. Global silicate weathering and CO_2 consumption rates deduced from the chemistry of large rivers. Chemical Geology 159 (1-4), 3-30.

Garrels, R.M. and Mackenzie, F.T., 1967. Origin of chemical compositions of some springs and lakes. Advances in Chemistry Series (67), 222-242.

Genthon, C., Barnola, J.M., Raynaud, D., Lorius, C., Jouzel, J., Barkov, N.I., Korotkevich, Y.S. and Kotlyakov, V.M., 1987. Vostok ice core - climatic response to CO_2 and orbital forcing changes over the last climatic cycle. Nature 329 (6138), 414-418.

Geological Survey of Canada, 2008. Geoscience Data Repository - Bedrock Geological maps, http://gdr.nrcan.gc.ca/index_e.php, accessed on 17. June 2008.

Gibbs, M.T. and Kump, L.R., 1994. Global chemical erosion during the last glacial maximum and the present - sensitivity to changes in lithology and hydrology. Paleoceanography 9 (4), 529-543.

Gibbs, R.J., 1967. Geochemistry of amazon river system: Part I. Factors that control salinity and composition and concentration of suspended solids. Geological Society of America Bulletin 78 (10), 1203-1232.

Gislason, S.R., Oelkers, E.H., Eiriksdottir, E.S., Kardjilov, M.I., Gisladottir, G., Sigfusson, B., Snorrason, A., Elefsen, S., Hardardottir, J., Torssander, P. and Oskarsson, N., 2009. Direct evidence of the feedback between climate and weathering. Earth and Planetary Science Letters 277 (1-2), 213-222.

Goldich, S.S., 1938. A study in rock-weathering. Journal of Geology 46 (1), 17-58.

Goolsby, D.A., Battaglin, W.A., Lawrence, G.B., Artz, R.S., Aulenbach, B.T., Hooper, R.P., Keeney, D.R. and Stensland, G.J., 1999. Flux and sources of nutrients in the Mississippi–Atchafalaya river basin: Topic 3 Report for the integrated assessment on hypoxia in the Gulf of Mexico. NOAA Coastal Ocean Program Decision Analysis Series. NOAA Coastal Ocean Program, Silver Spring, pp. 130.

Gordey, S.P. and Makepeace, A.J., 2000. Yukon Digital Geology. Exploration and Geological Services Division (EGSD), Yukon Region, Indian and Northern Affairs Canada.

Government of Alberta, 2009. River Network Station Water Quality Data, http://www.environment.gov.ab.ca/, accessed on 9. April 2009.

Grosbois, C., Negrel, P., Grimaud, D. and Fouillac, C., 2001. An overview of dissolved and suspended matter fluxes in the loire river basin: Natural and anthropogenic inputs. Aquatic Geochemistry 7 (2), 81-105.

Hadlari, T. and Rainbird, R.H., 2000. Sequence Stratigraphy and Sedimentology of the Paleoproterozoic Baker Lake Group in the Baker Lake Basin, Thirty Mile Lake, Nunavut. 2000-C9, Geological Survey of Canada.

Hadlari, T., Rainbird, R.H. and Donaldson, J.A., 2006. Alluvial, eolian and lacustrine sedimentology of a Paleoproterozoic half-graben, Baker Lake Basin, Nunavut, Canada. Sedimentary Geology 190 (1-4), 47-70.

Hagedorn, B. and Cartwright, I., 2009. Climatic and lithologic controls on the temporal and spatial variability of CO_2 consumption via chemical weathering: An example from the Australian Victorian Alps. Chemical Geology 260 (3-4), 234-253.

Hamblin, A.P., 1997. Stratigraphic architecture of the Oldman Formation, Belly River Group, surface and subsurface of southern Alberta. Bulletin of Canadian Petroleum Geology 45 (2), 155-177.

Hamilton, W.N., Langenberg, C.W. and Price, M., 2004. Bedrock geology of Alberta. Alberta Geological Survey.

Han, Y. and Huh, Y., 2009. A geochemical reconnaissance of the Duman (Tumen) River and the hot springs of Mt. Baekdu (Changbai): Weathering of volcanic rocks in mid-latitude setting. Chemical Geology 264 (1-4), 162-172.

Hartmann, J., 2008. Analysis of CO_2-consumption and dissolved silica fluxes caused by chemical weathering: Steps towards modeling dissolved matter fluxes on regional an global scales, Technische Universität Darmstadt, Darmstadt, pp. 132.

Hartmann, J., 2009. Bicarbonate-fluxes and CO_2-consumption by chemical weathering on the Japanese Archipelago - Application of a multi-lithological model framework. Chemical Geology 265 (3-4), 237-271.

Hartmann, J., Dürr, H.H., Jansen, N. and Meybeck, M., submitted. Differences between the geochemical composition of the continental crust and the terrestrial surface. Submitted to Journal of Geochemical Exploration.

Hartmann, J., Jansen, N., Dürr, H.H., Harashima, A., Okubo, K. and Kempe, S., 2010. Predicting riverine dissolved silica fluxes into coastal zones from a hyperactive region and analysis of their first order controls. International Journal of Earth Sciences 99 (1), 207-230.

Hartmann, J., Jansen, N., Dürr, H.H., Kempe, S. and Köhler, P., 2009. Global CO2-consumption by chemical weathering: what is the contribution of highly active weathering regions? Global and Planetary Change 69 (4), 185-194.

Hartmann, J., Jansen, N., Kempe, S. and Dürr, H.H., 2007. Geochemistry of the river rhine and the upper danube: Recent trends and lithological influence on baselines. Journal of Environmental Science for Sustainable Society 1, 39-46.

Hartmann, J., Kunimatsu, T. and Levy, J.K., 2008. The impact of Eurasian dust storms and anthropogenic emissions on atmospheric nutrient deposition rates in forested Japanese catchments and adjacent regional seas. Global and Planetary Change 61 (3-4), 117-134.

Hayes, B.J.R., Christopher, J.E., Rosenthal, L., Los, G., McKercher, B., Minken, D., Tremblay, Y.M. and Fennell, J., 1994. Chapter 19: Cretaceous Mannville Group of the Western Canada Sedimentary Basin in Geological Atlas of the Western Canada Sedimentary Basin.

Hedin, L.O., Granat, L., Likens, G.E., Buishand, T.A., Galloway, J.N., Butler, T.J. and Rodhe, H., 1994. Steep declines in atmospheric base cations in regions of europe and North America. Nature 367 (6461), 351-354.

Heinen, E.A. and McManus, J., 2004. Carbon and nutrient cycling at the sediment-water boundary in western Lake Superior. Journal of Great Lakes Research 30, 113-132.

Hijmans, R.J., Cameron, S.E., Parra, J.L., Jones, P.G. and Jarvis, A., 2005. Very high resolution interpolated climate surfaces for global land areas. International Journal of Climatology 25 (15), 1965-1978.

Hinderer, M., 2006. Chemical budgets of small catchments in SW Germany. Grundwasser 11 (3), 164-178.

Holland, H.D., 1978. The chemistry of the atmosphere and oceans. Wiley, New York, pp. 351.

Horton, T.W., Chamberlain, C.P., Fantle, M. and Blum, J.D., 1999. Chemical weathering and lithologic controls of water chemistry in a high-elevation river system: Clark's Fork of the Yellowstone River, Wyoming and Montana. Water Resources Research 35 (5), 1643-1655.

Huh, Y. and Edmond, J.M., 1999. The fluvial geochemistry of the rivers of Eastern Siberia: III. Tributaries of the Lena and Anabar draining the basement terrain of the Siberian Craton and the Trans-Baikal Highlands. Geochimica et Cosmochimica Acta 63 (7-8), 967-987.

Humborg, C., Ittekkot, V., Cociasu, A. and von Bodungen, B., 1997. Effect of Danube river dam on Black Sea biogeochemistry and ecosystem structure. Nature 386 (6623), 385-388.

Humborg, C., Pastuszak, M., Aigars, J., Siegmund, H., Morth, C.M. and Ittekkot, V., 2006. Decreased silica land-sea fluxes through damming in the Baltic Sea catchment - significance of particle trapping and hydrological alterations. Biogeochemistry 77 (2), 265-281.

IPCC, 2007. Climate Change 2007: The Physical Science Basis; Contribution of Working Group I. Fourth Assessment Report of the Intergovernmental Panel on Climate Change. Cambridge University Press, Cambridge, pp. 987.

Irish, E.J.W., 1971. Geology, Southern Plains of Alberta, west of fourth meridian. Geological Survey of Canada.

Jansen, N., Hartmann, J., Lauerwald, R., Dürr, H.H., Kempe, S., Loos, S. and Middelkoop, H., 2010. Dissolved Silica mobilization in the conterminous USA. Chemical Geology 270 (1-4), 90-109.

Jansen, N., Hartmann, J., Lauerwald, R. and Kempe, S., in prep. Bicarbonate fluxes and CO_2 consumption related to chemical weathering on the North American Continent.

Jarvis, A., Reuter, H.I., Nelson, A. and Guevara, E., 2006. Hole-filled seamless SRTM data V3, International Centre for Tropical Agriculture (CIAT), available from http://srtm.csi.cgiar.org.

Johns, S.M. and Young, M.D., 2006. Bedrock Geology and economic potential of the Archean Mary River Group, nothern Baffin Island, Nunavut. 2006-C5, Geological Survey of Canada.

Kalbitz, K., Solinger, S., Park, J.H., Michalzik, B. and Matzner, E., 2000. Controls on the dynamics of dissolved organic matter in soils: A review. Soil Science 165 (4), 277-304.

Kaushal, S.S., Groffman, P.M., Likens, G.E., Belt, K.T., Stack, W.P., Kelly, V.R., Band, L.E. and Fisher, G.T., 2005. Increased salinization of fresh water in the northeastern United States.

Proceedings of the National Academy of Sciences of the United States of America 102 (38), 13517-13520.

Keene, W.C., Pszenny, A.A.P., Galloway, J.N. and Hawley, M.E., 1986. Sea-salt corrections and interpretation of constituent ratios in marine precipitation. Journal of Geophysical Research-Atmospheres 91 (D6), 6647-6658.

Kempe, S., 1979. Carbon in the rock cycle. In: B. Bolin, E.T. Degens, S. Kempe and P. Ketner (Eds.), The Global Carbon Cycle. Scientific Committee On Problems of the Environment (SCOPE), Old Woking, 343-375.

Kempe, S., 1982. Long-term records of CO_2 pressure fluctuations in fresh waters In: E.T. Degens (Ed.), Transport of carbon and minerals in major world rivers part 1. Geologisch-Paläontologisches Institut Universität Hamburg, Hamburg, 91-332.

Kempe, S. and Degens, E.T., 1985. An early soda ocean? Chemical Geology 53 (1-2), 95-108.

Kempe, S. and Werner, M.S., 2003. The Kuka'iau Cave, Mauna Kea, Hawaii, created by water erosion: A new Hawaiian cave type. Journal of Cave and Karst Studies 65 (1), 53-67.

Kennedy, M.J., Chadwick, O.A., Vitousek, P.M., Derry, L.A. and Hendricks, D.M., 1998. Changing sources of base cations during ecosystem development, Hawaiian Islands. Geology 26 (11), 1015-1018.

Kristiansen, S. and Hoell, E.E., 2002. The importance of silicon for marine production. Hydrobiologia 484 (1-3), 21-31.

Kump, L.R., Brantley, S.L. and Arthur, M.A., 2000. Chemical, weathering, atmospheric CO_2, and climate. Annual Review of Earth and Planetary Sciences 28, 611-667.

Lehner, B., Verdin, K. and Jarvis, A., 2008. New global hydrography derived from spaceborne elevation data. EOS Transactions 89 (10), 93-94.

Lenton, T.M. and Britton, C., 2006. Enhanced carbonate and silicate weathering accelerates recovery from fossil fuel CO_2 perturbations. Global Biogeochemical Cycles 20 (3), GB3009.

Lerman, A., Wu, L.L. and Mackenzie, F.T., 2007. CO_2 and H_2SO_4 consumption in weathering and material transport to the ocean, and their role in the global carbon balance. Marine Chemistry 106 (1-2), 326-350.

Livingstone, D.A., 1963. Chemical composition of rivers and lakes. In: M. Fleischer (Ed.), Data of Geochemistry, Sixth Edition. USGS Professional Papers United States Government, Washington, 1-61.

Lofgren, S., 2001. The chemical effects of deicing salt on soil and stream water of five catchments in southeast Sweden. Water Air and Soil Pollution 130 (1-4), 863-868.

Lucas, Y., 2001. The role of plants in controlling rates and products of weathering: Importance of biological pumping. Annual Review of Earth and Planetary Sciences 29, 135-163.

Ludington, S., Moring, B.C., Miller, R.J., Flynn, K.S., Hopkins, M.J. and Haxel, G.A., 2005. Preliminary integrated databases for the United States - Western States: California, Nevada, Arizona, Washington, Oregon, Idaho, and Utah, U.S. Geological Survey Open-File Report. U.S. Geological Survey.

Ludwig, W., Amiotte-Suchet, P., Munhoven, G. and Probst, J.L., 1998. Atmospheric CO_2 consumption by continental erosion: present-day controls and implications for the last glacial maximum. Global and Planetary Change 17, 107-120.

Ma, J.F. and Takahashi, E., 1989. Release of silicon from rice straw under flooded conditions. Soil Science and Plant Nutrition 35 (4), 663-667.

Macdonald, R. and Slimmon, W.L., 1999. Geological map of Saskatchewan (Digital). Saskatchewan Industry and Resources.

Massey, F.P., Ennos, A.R. and Hartley, S.E., 2007. Herbivore specific induction of silica-based plant defences. Oecologia 152 (4), 677-683.

Massey, N.W.D., MacIntyre, D.G., Desjardins, P.J. and Cooney, R.T., 2005. Digital Map of British Columbia: Whole Province. B.C. Ministry of Energy and Mines.

Mast, M.A., Drever, J.I. and Baron, J., 1990. Chemical weathering in the Loch Vale watershed, Rocky-Mountain-National-Park, Colorado. Water Resources Research 26 (12), 2971-2978.

McMechan, M.E. and Dawson, F.M., 1995. Geology, Wapiti, West of Sixth Meridian, Alberta. Geological Survey of Canada.

Meybeck, M., 1986. Composition chimique des ruisseaux non pollués de France. Science Géologique Bulletin 39 (1), 3-77.

Meybeck, M., 1987. Global chemical weathering of surficial rocks estimated from river dissolved loads. American Journal of Science 287 (5), 401-428.

Miller, W.R. and Drever, J.I., 1977. Chemical weathering and related controls on surface water chemistry in the Absaroka Mountains, Wyoming. Geochimica et Cosmochimica Acta 41 (12), 1693-1702.

Milliman, J.D. and Syvitski, J.P.M., 1992. Geomorphic tectonic control of sediment discharge to the ocean - the importance of small mountainous rivers. Journal of Geology 100 (5), 525-544.

Millot, R., Gaillardet, J., Dupre, B. and Allegre, C.J., 2002. The global control of silicate weathering rates and the coupling with physical erosion: new insights from rivers of the Canadian Shield. Earth and Planetary Science Letters 196 (1-2), 83-98.

Miretzky, P., Conzonno, V. and Cirelli, A.F., 2001. Geochemical processes controlling silica concentrations in groundwaters of the Salado River drainage basin, Argentina. Journal of Geochemical Exploration 73 (3), 155-166.

Moll, S.J., Bie, S., Peterson, D., Pray, D.C., Wilson, F.H., Schmidt, J.M., Riehele, J.R. and Miller, T.P., 1997. Polygon Data from 1980 "Geologic Map of Alaska". U.S. Geological Survey.

Montgomery, D.R., 2003. Predicting landscape-scale erosion rates using digital elevation models. Comptes Rendus Geoscience 335 (16), 1121-1130.

Montgomery, D.R. and Brandon, M.T., 2002. Topographic controls on erosion rates in tectonically active mountain ranges. Earth and Planetary Science Letters 201 (3-4), 481-489.

Moulton, K.L., West, J. and Berner, R.A., 2000. Solute flux and mineral mass balance approaches to the quantification of plant effects on silicate weathering. American Journal of Science 300 (7), 539-570.

NADP, 2008a. National Atmospheric Deposition Program (NRSP-3), http://nadp.sws.uiuc.edu/, accessed on 14 June 2008.

NADP, 2008b. National Atmospheric Deposition Program: Isopleth maps, http://nadp.sws.uiuc.edu/isopleths/annualmaps.asp, accessed on 26 August 2008.

Navarre-Sitchler, A. and Brantley, S., 2007. Basalt weathering across scales. Earth and Planetary Science Letters 261 (1-2), 321-334.

Navarre-Sitchler, A. and Thyne, G., 2007. Effects of carbon dioxide on mineral weathering rates at earth surface conditions. Chemical Geology 243 (1-2), 53-63.

Neff, J.C., Ballantyne, A.P., Farmer, G.L., Mahowald, N.M., Conroy, J.L., Landry, C.C., Overpeck, J.T., Painter, T.H., Lawrence, C.R. and Reynolds, R.L., 2008. Increasing eolian dust deposition in the western United States linked to human activity. Nature Geoscience 1 (3), 189-195.

Nicholson, S.W., Dicken, C.L., Foose, M.P. and Mueller, J.A.L., 2007. Integrated geologic map databases for the United States: The Upper Midwest States: Minnesota, Wisconsin, Michigan, Illinois and Indiana, Geological Survey Open-File Report, Reston.

Nicholson, S.W., Dicken, C.L., Horton, J.D., Foose, M.P., Mueller, J.A.L. and Hon, R., 2006. Preliminary Integrated Geologic Map Databases for the United States: Connecticut, Maine, Massachusetts, New Hampshire, New Jersey, Rhode Island, Vermont, U.S. Geological Survey Open-File Report. U.S. Geological Survey, Reston.

Nicholson, S.W., Dicken, C.L., Horton, J.D., Labay, K.A., Foose, M.P. and Mueller, J.A.L., 2005. Preliminary integrated Geologic Map Databases for the United States: Kentucky, Ohio, Tennessee, and West Virginia, U.S. Geological Survey Open-File Report. U.S. Geological Survey, Reston.

Officer, C.B. and Ryther, J.H., 1980. The Possible Importance of Silicon in Marine Eutrophication. Marine Ecology-Progress Series 3 (1), 83-91.

Okulitch, A.V., 2006. Phanerozoic bedrock geology, Lake Athabasca, Alberta - Saskatchewan, Open File 5280. Geological Survey of Canada.

Oliva, P., Dupre, B., Martin, F. and Viers, J., 2004. The role of trace minerals in chemical weathering in a high-elevation granitic watershed (Estibere, France): Chemical and mineralogical evidence. Geochimica et Cosmochimica Acta 68 (10), 2223-2243.

Oliva, P., Viers, J. and Dupré, B., 2003. Chemical weathering in granitic environments. Chemical Geology 202 (3-4), 225-256.

Ollerenshaw, N.C., 1970. Marble Mountain, Alberta. Geological Survey of Canada.

Paces, T., 1983. Rate constants of dissolution derived from the measurements of mass balance in hydrological catchments. Geochimica et Cosmochimica Acta 47 (11), 1855-1863.

Pagani, M., Caldeira, K., Berner, R. and Beerling, D.J., 2009. The role of terrestrial plants in limiting atmospheric CO_2 decline over the past 24 million years. Nature 460 (7251), 85-U94.

Perrin, A.S., Probst, A. and Probst, J.L., 2008. Impact of nitrogenous fertilizers on carbonate dissolution in small agricultural catchments: Implications for weathering CO_2 uptake at regional and global scales. Geochimica et Cosmochimica Acta 72 (13), 3105-3123.

Pierson-Wickmann, A.C., Aquilina, L., Martin, C., Ruiz, L., Molénat, J., Jaffrézic, A. and Gascuel-Odoux, C., 2009. High chemical weathering rates in first-order granitic catchments induced by agricultural stress. Chemical Geology 265 (3-4), 369-380.

Pisias, N.G. and Shackleton, N.J., 1984. Modeling the Global Climate Response to Orbital Forcing and Atmospheric Carbon-Dioxide Changes. Nature 310 (5980), 757-759.

Pollock, S.M., Goodarzi, F. and Riediger, C.L., 2000. Mineralogical and elemental variation of coal from Alberta, Canada: an example from the No. 2 seam, Genesee Mine. International Journal of Coal Geology 43 (1-4), 259-286.

Porder, S., Hilley, G.E. and Chadwick, O.A., 2007. Chemical weathering, mass loss, and dust inputs across a climate by time matrix in the Hawaiian Islands. Earth and Planetary Science Letters 258 (3-4), 414-427.

Powers, D.L., 1931. Subsurface Study of Pale Beds and Foremost Formation in Lethbridge-Brooks Area of Southern Alberta. AAPG Bulletin 15.

Pruett, R.J. and Murray, H.H., 1991. Clay mineralogy, alteration history, and economic geology of the whitemud formation, southern Saskatchewan, Canada. Clays and Clay Minerals 39 (6), 586-596.

Rad, S., Louvat, P., Gorge, C., Gaillardet, K. and Allegre, C.J., 2006. River dissolved and solid loads in the Lesser Antilles: New insight into basalt weathering processes. Journal of Geochemical Exploration 88 (1-3), 308-312.

Ragueneau, O., Conley, D.J., DeMaster, D.J., Dürr, H.H. and Dittert, N., 2009. Si transformations along the land-ocean-continuum: Implications for the global carbon cycle. In: K.K. Liu, L. Atkinson, R. Quinones and L. Talaue-McManus (Eds.), Carbon and nutrient fluxes in continental margins. Global Change - The IGBP Series. Springer, Berlin.

Raymo, M.E., Ruddiman, W.F. and Froelich, P.N., 1988. Influence of late cenozoic mountain building on ocean geochemical cycles. Geology 16 (7), 649-653.

Raymond, P.A. and Cole, J.J., 2003. Increase in the export of alkalinity from North America's largest river. Science 301 (5629), 88-91.

Raymond, P.A., Oh, N.H., Turner, R.E. and Broussard, W., 2008. Anthropogenically enhanced fluxes of water and carbon from the Mississippi River. Nature 451 (7177), 449-452.

Raynaud, D., Jouzel, J., Barnola, J.M., Chappellaz, J., Delmas, R.J. and Lorius, C., 1993. The ice record of greenhouse gases. Science 259 (5097), 926-934.

Reynolds, R.C. and Johnson, N.M., 1972. Chemical weathering in the temperate glacial environment of the Northern Cascade Mountains. Geochimica et Cosmochimica Acta 36 (5), 537-554.

Richardson, R.J.H., Langenberg, C.W., Chao, D. and Fietz, D.W., 1990. Coal compilation project: Entrance, NTS 83F/5. Open File Report 1990-02, Alberta Geological Survey.

Riebe, C.S., Kirchner, J.W. and Finkel, R.C., 2004. Erosional and climatic effects on long-term chemical weathering rates in granitic landscapes spanning diverse climate regimes. Earth and Planetary Science Letters 224 (3-4), 547-562.

Rosfjord, C.H., Webster, K.E., Kahl, J.S., Norton, S.A., Fernandez, I.J. and Herlihy, A.T., 2007. Anthropogenically driven changes in chloride complicate interpretation of base cation trends in lakes recovering from acidic deposition. Environmental Science & Technology 41 (22), 7688-7693.

Rosling, A., 2009. Trees, Mycorrhiza and Minerals -Field Relevance of in vitro Experiments. Geomicrobiology Journal 26 (6), 389-401.

Roth, J., 1893. Allgemeine und chemische Geologie, Dritter Band - Zweite Abteilung: Verwitterung, Zersetzung und Zerstörung der Gesteine. Verlag von WIlhelm Hertz (Bessersche Buchhandlung), Berlin, pp. 530.

Roy, S., Gaillardet, J. and Allegre, C.J., 1999. Geochemistry of dissolved and suspended loads of the Seine river, France: Anthropogenic impact, carbonate and silicate weathering. Geochimica et Cosmochimica Acta 63 (9), 1277-1292.

Rozalen, M., Huertas, F.J. and Brady, P.V., 2009. Experimental study of the effect of pH and temperature on the kinetics of montmorillonite dissolution. Geochimica et Cosmochimica Acta 73 (13), 3752-3766.

Saccone, L., Conley, D.J., Koning, E., Sauer, D., Sommer, M., Kaczorek, D., Blecker, S.W. and Kelly, E.F., 2007. Assessing the extraction and quantification of amorphous silica in soils of forest and grassland ecosystems. European Journal of Soil Science 58 (6), 1446-1459.

Saccone, L., Conley, D.J., Likens, G.E., Bailey, S.W., Buso, D.C. and Johnson, C.E., 2008. Factors that control the range and variability of amorphous silica in soils in the Hubbard Brook Experimental Forest. Soil Science Society of America Journal 72 (6), 1637-1644.

Schau, M., 1993. Geology, northern Melville Peninsula, District of Franklin, Northwest Territories. Geological Survey of Canada.

Schelske, C.L., 1985. Biogeochemical silica mass balances in Lake-Michigan and Lake-Superior. Biogeochemistry 1 (3), 197-218.

Schelske, C.L. and Stoermer, E.F., 1971. Eutrophication, silica depletion, and predicted changes in algal quality in Lake Michigan. Science 173 (3995), 423-424.

Schledewitz, D.C.P. and Lindal, D., 2005. Bedrock Geology Compilation Map Series, NTS 54M, scale 1: 250 000. Manitoba Geological Survey.

Schnoor, J.L., 1990. Kinetics of chemical weathering: a comparison of laboratory and field weathering rates. In: W. Stumm (Ed.), Aquatic Chemical Kinetics. Wiley-Interscience, New York, 475-504.

Schwartzman, D.W. and Volk, T., 1989. Biotic enhancement of weathering and the habitability of earth. Nature 340 (6233), 457-460.

Sferratore, A., Billen, G., Garnier, J., Smedberg, E., Humborg, C. and Rahm, L., 2008. Modelling nutrient fluxes from sub-arctic basins: Comparison of pristine vs. dammed rivers. Journal of Marine Systems 73 (3-4), 236-249.

Sferratore, A., Garnier, J., Billen, G., Conley, D.J. and Pinault, S., 2006. Diffuse and point sources of silica in the Seine river watershed. Environmental Science & Technology 40 (21), 6630-6635.

Siebert, S., Döll, P., Hoogeveen, J., Faures, J.M., Frenken, K. and Feick, S., 2005. Development and validation of the global map of irrigation areas. Hydrology and Earth System Sciences 9 (5), 535-547.

Sieracki, M.E., Verity, P.G. and Stoecker, D.K., 1993. Plankton community response to sequential silicate and nitrate depletion during the 1989 North-Atlantic spring bloom. Deep-Sea Research Part II-Topical Studies in Oceanography 40 (1-2), 213-225.

Smayda, T.J., 1990. Novel and nuisance phytoplankton blooms in the sea: evidence for a global epidemic. In: E. Granéli, B. Sundström, L. Edler and D.M. Anderson (Eds.), Toxic marine phytoplankton: proceedings of the Fourth International Conference on Toxic Marine Phytoplankton held June 26-30 in Lund, Sweden. Elsevier, New York, 29-40.

Stallard, R.F., 1995. Tectonic, environmental, and human aspects of weathering and erosion - a global review using a steady-state perspective. Annual Review of Earth and Planetary Sciences 23, 11-39.

Stallard, R.F. and Edmond, J.M., 1983. Geochemistry of the Amazon 2: The influence of geology and weathering environment on the dissolved load. Journal of Geophysical Research 88, 9671-9688.

Stewart, B.W., Capo, R.C. and Chadwick, O.A., 2001. Effects of rainfall on weathering rate, base cation provenance, and Sr isotope composition of Hawaiian soils. Geochimica et Cosmochimica Acta 65 (7), 1087-1099.

Stoeser, D.B., Green, G.N., Morath, L.C., Heran, W.D., Wilson, A.B., Moore, D.W. and Van Gosen, B.S., 2005. Preliminary Integrated Geologic Map Databases for the United States Central States: Montana, Wyoming, Colorado, New Mexico, Kansas, Oklahoma, Texas, Missouri, Arkansas, and Louisiana, North Dakota, South Dakota, Nebraska, and Iowa, U.S. Geological Survey Open-File Report. U.S. Geological Survey.

Street-Perrott, F.A. and Barker, P.A., 2008. Biogenic silica: a neglected component of the coupled global continental biogeochemical cycles of carbon and silicon. Earth Surface Processes and Landforms 33 (9), 1436-1457.

Struyf, E. and Conley, D.J., 2009. Silica: an essential nutrient in wetland biogeochemistry. Frontiers in Ecology and the Environment 7 (2), 88-94.

Struyf, E., Opdekamp, W., Backx, H., Jacobs, S., Conley, D.J. and Meire, P., 2009. Vegetation and proximity to the river control amorphous silica storage in a riparian wetland (Biebrza National Park, Poland). Biogeosciences 6 (4), 623-631.

Szramek, K. and Walter, L.M., 2004. Impact of carbonate precipitation on riverine inorganic carbon mass transport from a mid-continent, forested watershed. Aquatic Geochemistry 10 (1-2), 99-137.

Tella, S., Paul, D., Berman, R.G., Davis, W.J., Peterson, T.D., Pehrsson, S.J. and Kerswill, J.A., 2007. Bedrock geology compilation and regional synthesis of parts of Hearne and Rae domains, western Churchill Province, Nunavut - Manitoba. Geological Survey of Canada.

Transportation Research Board, 1991. Highway deicing : comparing salt and calcium magnesium acetate. Special report. National Research Council, Washington, D.C., pp. 170.

Treguer, P., Nelson, D.M., Vanbennekom, A.J., Demaster, D.J., Leynaert, A. and Queguiner, B., 1995. The Silica Balance in the World Ocean - a Reestimate. Science 268 (5209), 375-379.

Triplett, L.D., Engstrom, D.R., Conley, D.J. and Schellhaass, S.M., 2008. Silica fluxes and trapping in two contrasting natural impounds of the upper Mississippi River. Biogeochemistry 87 (3), 217-230.

Uchikawa, J. and Zeebe, R.E., 2008. Influence of terrestrial weathering on ocean acidification and the next glacial inception. Geophysical Research Letters 35 (23), L23608.

USGS, 2000. HYDRO1k Elevation Derivative Database, http://eros.usgs.gov/products/elevation/gtopo30/hydro/, accessed on 2006/10/12.

USGS, 2001. Geochemistry of unconsolidated sediments in the US from the PLUTO database, U.S. Geological Survey, Reston, VA.

USGS, 2008a. Geochemistry of rock samples from the National Geochemical Database, USGS, Reston, VA.

USGS, 2008b. National Water Information System, http://waterdata.usgs.gov/nwis, accessed on 2008/06/24.

Velbel, M.A. and Price, J.R., 2007. Solute geochemical mass-balances and mineral weathering rates in small watersheds: Methodology, recent advances, and future directions. Applied Geochemistry 22 (8), 1682-1700.

Viers, J., Dupre, B. and Gaillardet, J., 2009. Chemical composition of suspended sediments in World Rivers: New insights from a new database. Science of the Total Environment 407 (2), 853-868.

Walker, J.C.G., Hays, P.B. and Kasting, J.F., 1981. A negative feedback mechanism for the long-term stabilization of Earths surface-temperature. Journal of Geophysical Research-Oceans and Atmospheres 86 (NC10), 9776-9782.
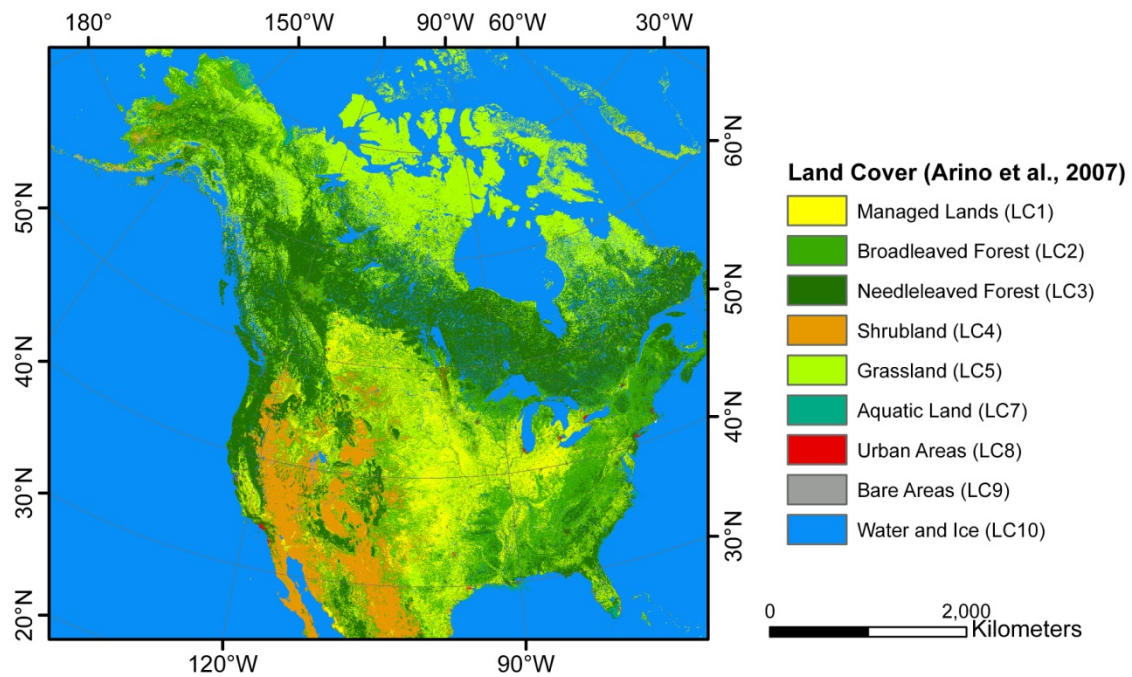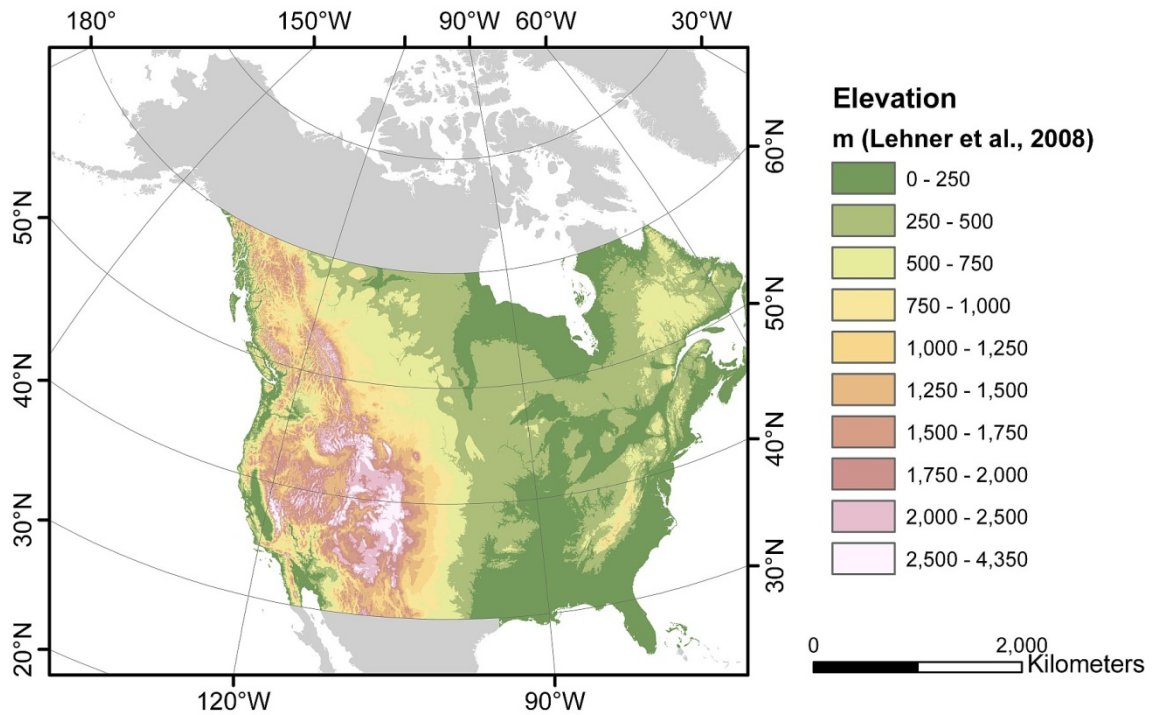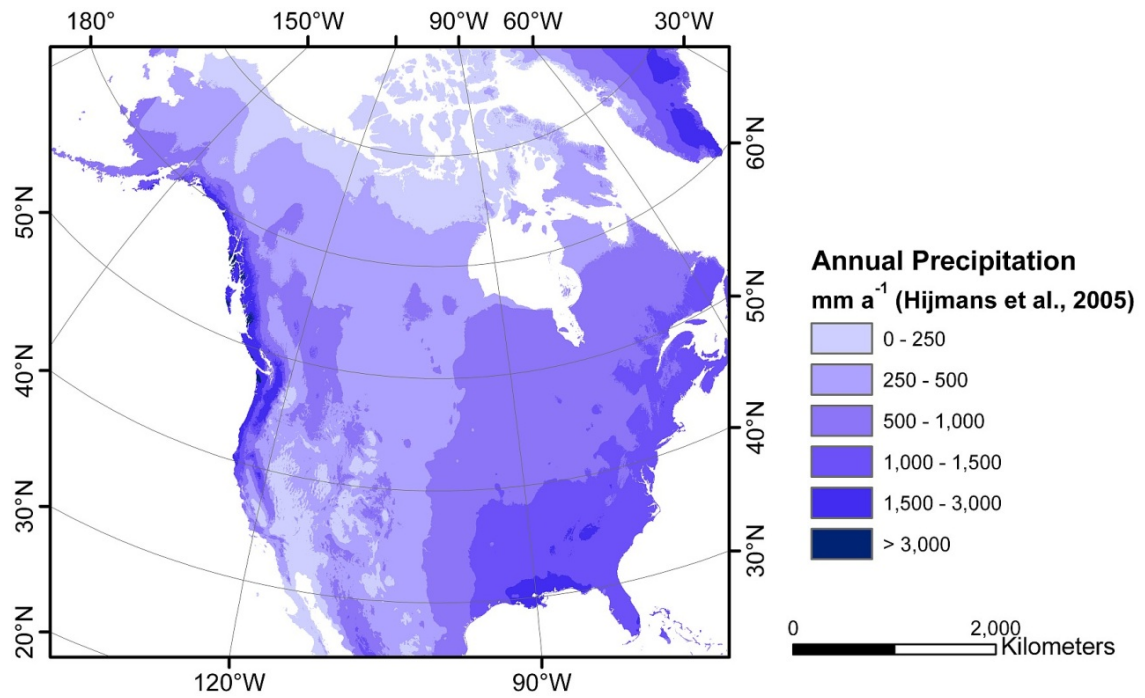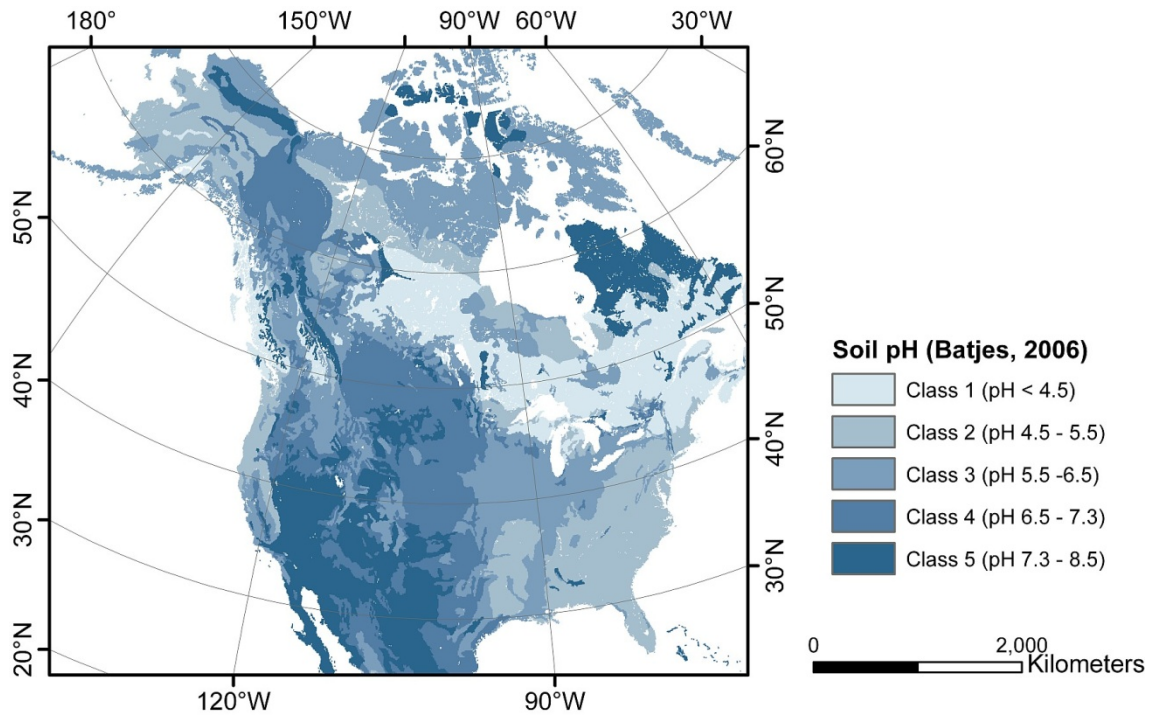
Watmough, S.A. and Dillon, P.J., 2004. Major element fluxes from a coniferous catchment in central Ontario, 1983-1999. Biogeochemistry 67 (3), 369-398.

West, A.J., Galy, A. and Bickle, M., 2005. Tectonic and climatic controls on silicate weathering. Earth and Planetary Science Letters 235 (1-2), 211-228.

Wheeler, J.O., Hoffman, P.F., Card, K.D., Davidson, A., Sanford, B.V., Okulitch, A.V. and Roest, W.R., 1997. Geological Map of Canada. Geological Survey of Canada.

White, A.F. and Blum, A.E., 1995. Effects of climate on chemical-weathering in watersheds. Geochimica et Cosmochimica Acta 59 (9), 1729-1747.

White, A.F., Blum, A.E., Bullen, T.D., Vivit, D.V., Schulz, M. and Fitzpatrick, J., 1999a. The effect of temperature on experimental and natural chemical weathering rates of granitoid rocks. Geochimica et Cosmochimica Acta 63 (19-20), 3277-3291.

White, A.F., Bullen, T.D., Vivit, D.V., Schulz, M.S. and Clow, D.W., 1999b. The role of disseminated calcite in the chemical weathering of granitoid rocks. Geochimica et Cosmochimica Acta 63 (13-14), 1939-1953.

Williams, M., Hopkinson, C., Rastetter, E., Vallino, J. and Claessens, L., 2005. Relationships of land use and stream solute concentrations in the Ipswich River basin, northeastern Massachusetts. Water Air and Soil Pollution 161 (1-4), 55-74.

Wolock, D.M. and McCabe, G.J., 2000. Differences in topographic characteristics computed from 100- and 1000-m resolution digital elevation model data. Hydrological Processes 14 (6), 987-1002.

Yeo, G., Jefferson, C.W. and Ramaekers, P., 2002. A preliminary comparison of Manitou Falls Formation stratigraphy in four Athabasca Basin deposystems, Saskatchewan Geological Survey.

Zakharova, E.A., Pokrovsky, O.S., Dupre, B. and Zaslavskaya, M.B., 2005. Chemical weathering of silicate rocks in Aldan Shield and Baikal Uplift: insights from long-term seasonal measurements of solute fluxes in rivers. Chemical Geology 214 (3-4), 223-248.

Zeebe, R.E. and Caldeira, K., 2008. Close mass balance of long-term carbon fluxes from ice-core CO_2 and ocean chemistry records. Nature Geoscience 1 (5), 312-315.

8 Appendixes

A Maps of selected assessed factors

Below, the maps for elevation, land cover, soil-pH, annual precipitation and temperature are given that are used in the studies of North America. The grey-shaded area in the elevation map is outside the applied HydroSheds data for North America.

Soil pH (Batjes, 2006)

Class 1 (pH < 4.5)
Class 2 (pH 4.5 - 5.5)
Class 3 (pH 5.5 -6.5)
Class 4 (pH 6.5 - 7.3)
Class 5 (pH 7.3 - 8.5)

Annual Precipitation
mm a^{-1} **(Hijmans et al., 2005)**

0 - 250
250 - 500
500 - 1,000
1,000 - 1,500
1,500 - 3,000
> 3,000

Runoff (Fekete et al., 2000)

mm a^{-1}

- 0 - 50
- 50 - 150
- 150 - 350
- 350 - 700
- 700 - 1,500
- > 1,500

Annual Mean Temperature

(Hijmans et al. 2005)

- < -15 °C
- -15 °C - -7.5 °C
- -7.5 °C - 0 °C
- 0 °C - 7.5 °C
- 7.5 °C - 15 °C
- > 15 °C
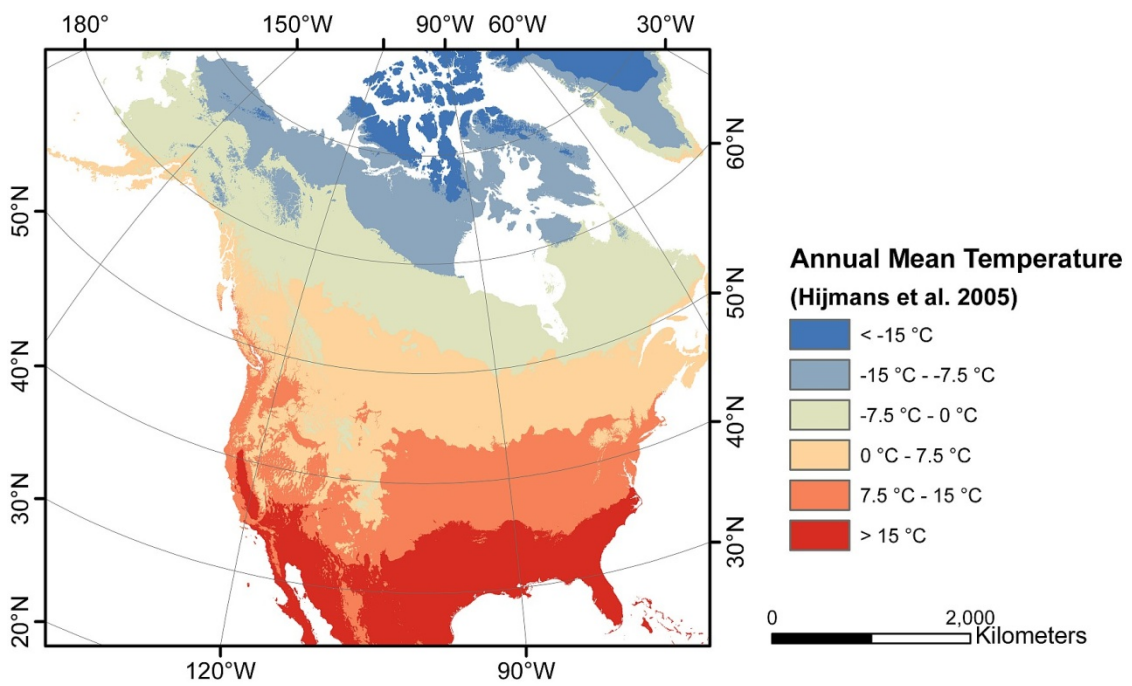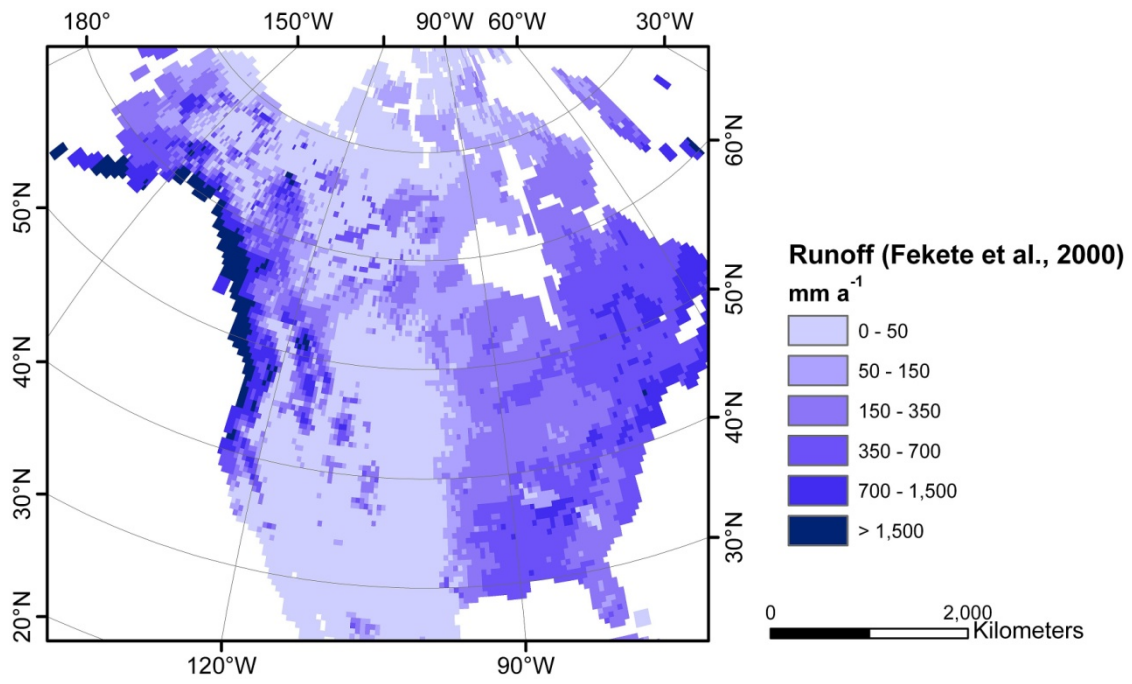
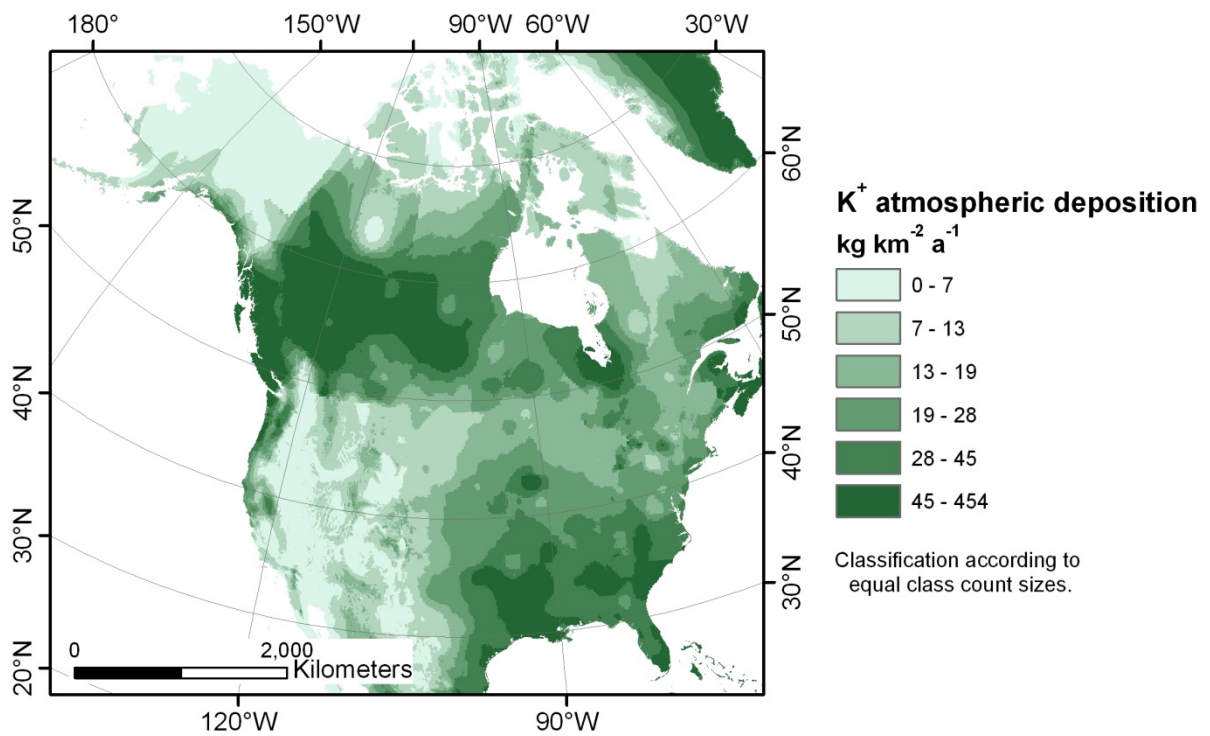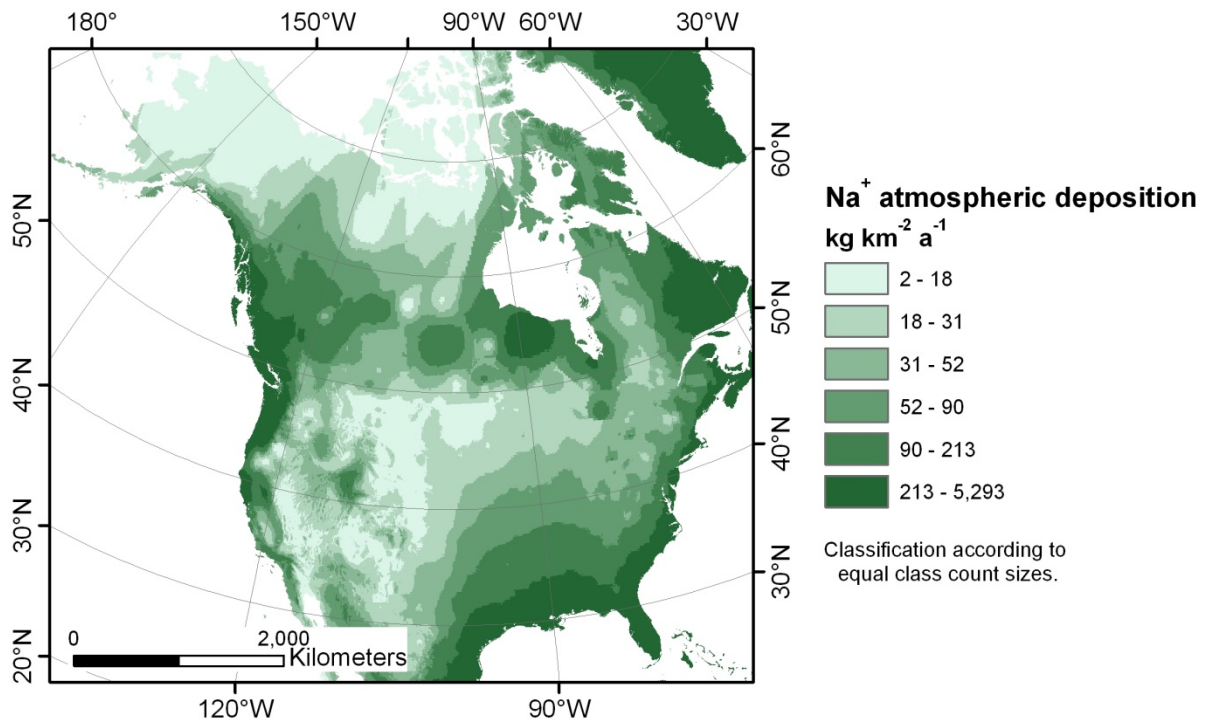# B Atmospheric input map

Following the watershed mass balance approach, it is crucial to know and subtract precipitation-derived element fluxes from total fluxes in rivers to calculate weathering derived element fluxes. To do this in North America, for each ion of the group Na^+, K^+, Ca^{2+}, Mg^{2+}, Cl^-, NO_3^- and SO_4^{2-} a raster layer with a grid size of 1 km² is calculated, representing the atmospheric input fluxes of each dissolved ion.
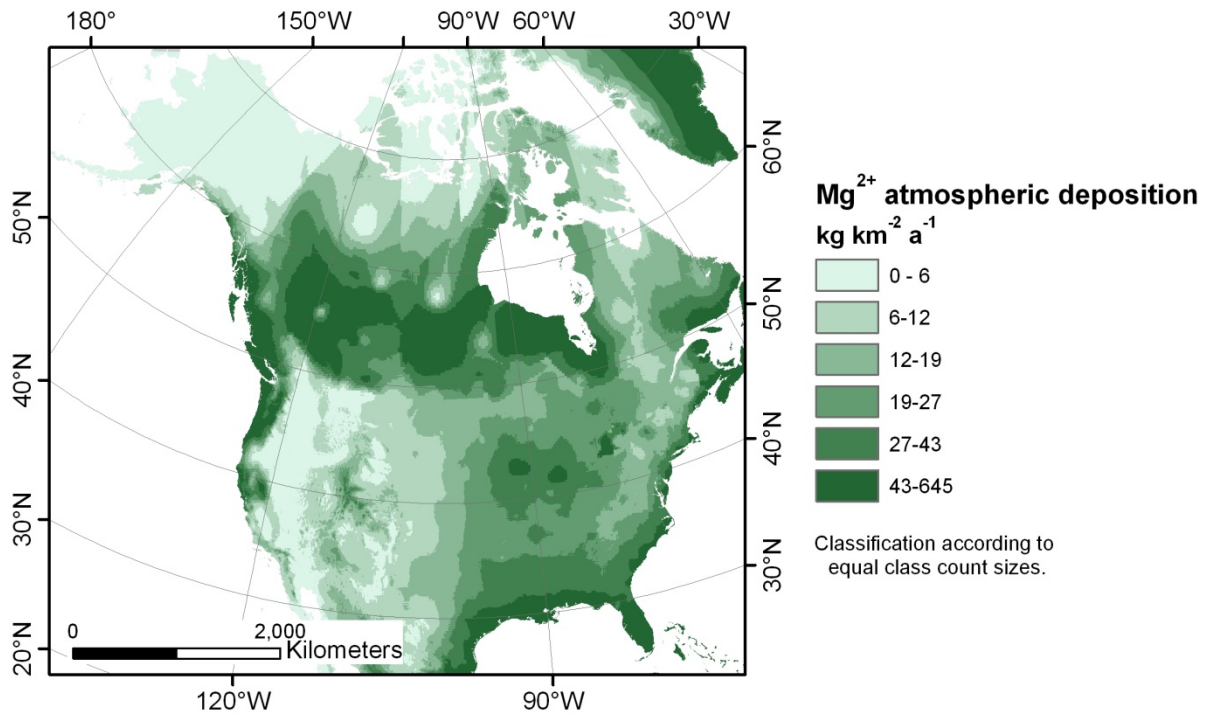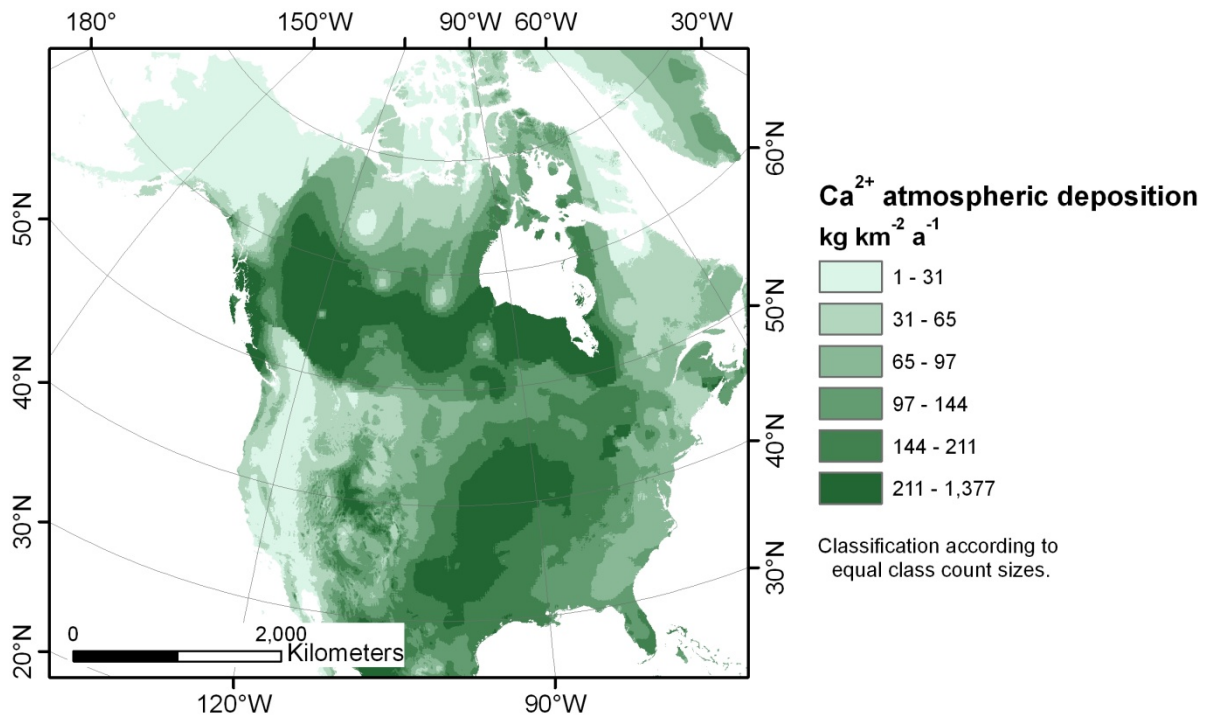
The raster is calculated as a product of ion concentration in precipitation and annual average precipitation (Hijmans et al., 2005). Ready prepared ion concentration maps are available for the conterminous U.S. (NADP, 2008b). However, for the rest of the continent, interpolated maps are generated from individual stations.
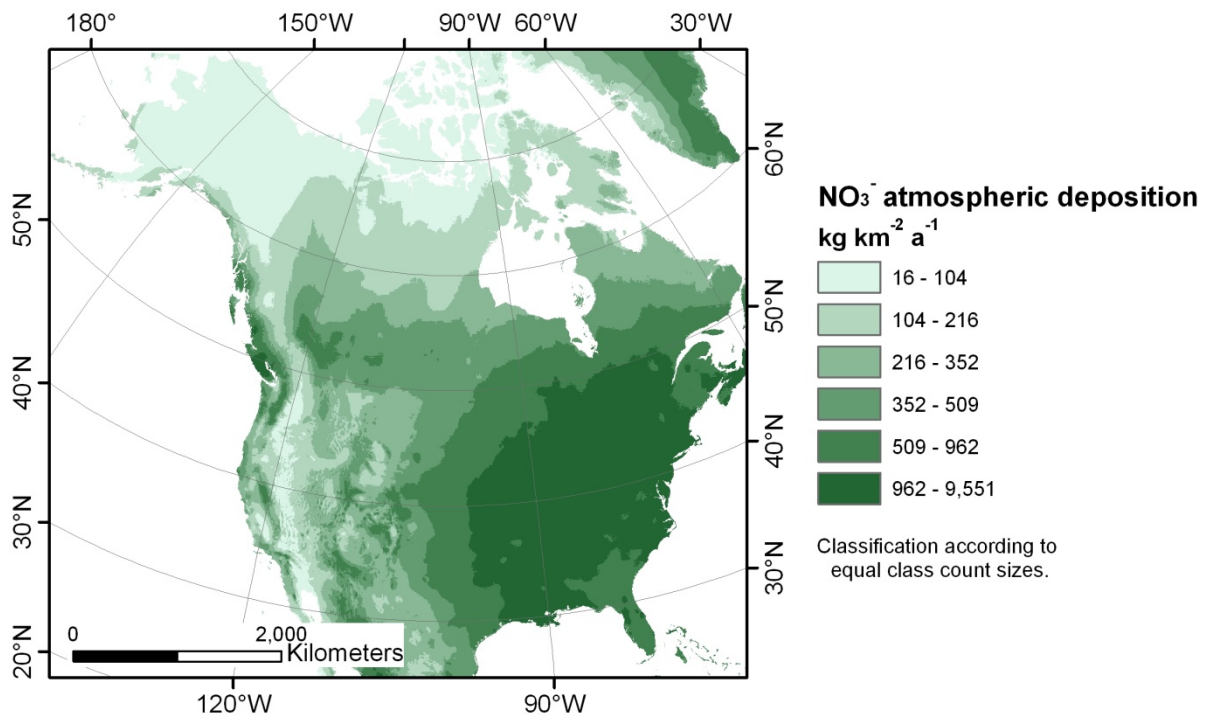
12 monitoring stations from Canada (Meteorological Service of Canada, 2008) and 8 stations in non-conterminous U.S. territories (NADP, 2008a) are used for interpolation. For each element and station, average concentrations were calculated. However, only periods of 12 consecutive monthly samples per station were used to represent a complete annual cycle. At the perimeter of the available continuous maps for the conterminous USA, virtual stations were placed in small intervals using the concentration information given in those maps. This provides additional input data for the interpolation as well as ensures a smooth transition from the interpolated maps to the maps of the National Atmospheric Deposition Program (2008b).

The interpolated maps are generated using "inverse distance weighting" interpolation functionality of ArcGIS (power=2). After a first iteration, two stations were duplicated, one was moved 400 km northeast to extend the maximum extent of the interpolations; the second, only including a value for K^+, reduces an artificial northward K^+-tailing from stations that are positioned further south.

The interpolated maps are combined with the existing (NADP, 2008b), while preference is given to the latter for the area which they cover. The finished combined maps are shown below.

Na⁺ atmospheric deposition
kg km⁻² a⁻¹

	2 - 18
	18 - 31
	31 - 52
	52 - 90
	90 - 213
	213 - 5,293

Classification according to
equal class count sizes.

K⁺ atmospheric deposition
kg km⁻² a⁻¹

	0 - 7
	7 - 13
	13 - 19
	19 - 28
	28 - 45
	45 - 454

Classification according to
equal class count sizes.

119

Ca²⁺ atmospheric deposition
kg km⁻² a⁻¹

- 1 - 31
- 31 - 65
- 65 - 97
- 97 - 144
- 144 - 211
- 211 - 1,377

Classification according to
equal class count sizes.

Mg²⁺ atmospheric deposition
kg km⁻² a⁻¹

- 0 - 6
- 6-12
- 12-19
- 19-27
- 27-43
- 43-645

Classification according to
equal class count sizes.

Cl⁻ atmospheric deposition
kg km^{-2} a^{-1}

	5 - 31
	31 - 54
	54 - 99
	99 - 154
	154 - 350
	350 - 9,293

Classification according to
equal class count sizes.

NO₃⁻ atmospheric deposition
kg km^{-2} a^{-1}

	16 - 104
	104 - 216
	216 - 352
	352 - 509
	509 - 962
	962 - 9,551

Classification according to
equal class count sizes.

SO$_4^{2-}$ atmospheric deposition
kg km^{-2} a^{-1}

	9 - 128
	128 - 260
	260 - 420
	420 - 690
	690 - 1,132
	1,132 - 4,993

Classification according to
equal class count sizes.

C Model parameters for Na_{sil}, Ca_{hco3} and $CO2/HCO_3$-HCO_3

Model b-parameters for the Na_{sil} model for the three Na_{sil} correction scenarios (Equation 8 A).

	Na_{sil1}		$Na_{sil0858}$		$Na_{sil0731}$	
	Estimation	p-level	Estimation	p-level	Estimation	p-level
b_{PAMT}	0.5775	0.0000	0.3944	0.0000	0.3275	0.0000
b_{VA}	0.9621	0.0000	0.9765	0.0000	1.0596	0.0000
b_{VBPB}	0.6935	0.0004	0.7570	0.0001	0.8373	0.0000
b_{SC}	0.5624	0.0000	0.3858	0.0000	0.2600	0.0000
b_{SU}	0.1878	0.0000	0.2916	0.0000	0.3527	0.0000
b_{SS}	0.4959	0.0000	0.5282	0.0000	0.5831	0.0000
b_{SM}	0.8286	0.0059	0.5883	0.0171	0.6743	0.0008

Model b-parameters for the Ca_{hco3} model for the five Ca_{hco3} correction scenarios (Equation 8 B). All b-parameters are significant with $p_{max} = 0.018$.

	Na_{sil1}	$Na_{sil0858}$		$Na_{sil0731}$	
	Ca_{alkso4}	$Ca_{alkclso4}$	Ca_{alkso4}	$Ca_{alkclso4}$	Ca_{alkso4}
	Estimation	Estimation	Estimation	Estimation	Estimation
b_{PAMT}	0.9476	0.9337	0.9539	0.8544	0.9182
b_{VA}	0.4317	0.4717	0.4683	0.4728	0.4637
b_{VBPB}	0.7217	0.7270	0.7237	0.7465	0.7329
b_{SC}	0.8409	0.8462	0.8586	0.8418	0.8693
b_{SU}	0.8008	0.7762	0.8228	0.7211	0.8052
b_{SS}	0.5646	0.5122	0.5188	0.5306	0.5448
b_{SM}	0.9774	0.9874	0.9882	0.9557	0.9642

Model b-parameters for the HCO_3^- model used for CO_2/HCO_3^- calculation for the three Na_{sil} correction scenarios (Equation 9).

	HCO_3 for Na_{sil1}		HCO_3 for $Na_{sil0858}$		HCO_3 for $Na_{sil0731}$	
	Estimation	p-level	Estimation	p-level	Estimation	p-level
b_0	0.0142	0.0040	0.0115	0.0029	0.0123	0.0017
b_{SU}	0.5196	0.0000	0.5363	0.0000	0.5129	0.0000
b_{PAMT}	0.3767	0.0000	0.3982	0.0000	0.4159	0.0000
b_{PB}	0.7404	0.0000	0.7688	0.0000	0.7524	0.0000
b_{SC}	0.7109	0.0000	0.7739	0.0000	0.7809	0.0000
b_{SM}	0.7279	0.0000	0.7576	0.0000	0.7553	0.0000
b_{SS}	0.5625	0.0000	0.5912	0.0000	0.5788	0.0000
b_{VA}	0.6233	0.0000	0.6685	0.0000	0.6532	0.0000
b_{VB}	0.4908	0.0000	0.5212	0.0000	0.5137	0.0000

D Curriculum Vitae

Nils Jansen was born in Aachen on 20th June 1980.

Working experience

March 2009 – ongoing	**Research assistant**, Institute for Biogeochemistry and Marine Chemistry, University of Hamburg
October 2006 – February 2009	**Research assistant**, Division of Physical Geology and Global Cycles, Darmstadt University of Technology, Germany
September 2004 – July 2007	**Graduate assistant** at the Hydrogeological Mapping Institute of the Chair of Engineering- and Hydrogeology, RWTH Aachen University
May 2002 – January 2004	**Graduate assistant** at the Geological Institute, RWTH Aachen University.

Academic Education

April 2009 – ongoing	**PhD-Student** at University of Hamburg
October 2006 – March 2009	**PhD-Student** at Darmstadt University of Technology
4. September 2006	**Diplom Geologie** at RWTH Aachen, Thesis title: „Faziesabhängigkeit geogener Arsengehalte in oligozänen Sedimenten der Niederrheinischen Bucht"
October 2000 – September 2009	**Studying geology** at RWTH Aachen (focus on hydrogeology and geochemistry)
August 1990 – May 1999	**Secondary School**, Rhein-Maas-Gymnasium, Aachen

E   Individual contributions to the list of publications

Jansen, N., Hartmann, J., Lauerwald, R. and Kempe, S., in prep. Bicarbonate fluxes and CO$_2$ consumption related to chemical weathering on the North American Continent.	**Research Idea:** N. Jansen, J. Hartmann **Analysis Framework:** N. Jansen, J. Hartmann **Data preparation:** N. Jansen, R. Lauerwald **Analysis:** N. Jansen **Results:** N. Jansen **Discussion:** N. Jansen, J. Hartmann, R. Lauerwald, S. Kempe
Jansen, N., Hartmann, J., Lauerwald, R., Dürr, H.H., Kempe, S., Loos, S. and Middelkoop, H., 2010. Dissolved Silica mobilization in the conterminous USA. Chemical Geology 270 (1-4), 90-109.	**Research Idea:** N. Jansen, J. Hartmann **Analysis Framework:** N. Jansen, J. Hartmann **Data preparation:** N. Jansen, R. Lauerwald **Analysis:** N. Jansen **Results:** N. Jansen **Discussion:** N. Jansen, J. Hartmann, R. Lauerwald, H.H. Dürr, S. Kempe, S. Loos, H. Middelkoop
Hartmann, J., Dürr, H.H., **Jansen, N.** and Meybeck, M., submitted. Differences between the geochemical composition of the continental crust and the terrestrial surface. Submitted to Journal of Geochemical Exploration.	**Research Idea:** J. Hartmann, H. H. Dürr **Analysis Framework:** J. Hartmann, H. H. Dürr **Data preparation:** J. Hartmann, H. H. Dürr, N. Jansen **Analysis:** J. Hartmann, H. H. Dürr, N. Jansen **Results:** J. Hartmann **Discussion:** J. Hartmann, H. H. Dürr, M. Meybeck
Abu Ghazleh, S., Hartmann, J., **Jansen, N.** and Kempe, S., 2009. Water input requirements of the rapidly shrinking Dead Sea. Naturwissenschaften 96 (5), 637-643.	**Research Idea:** S. Abu Ghazleh, S. Kempe **Analysis Framework:** S. Kempe, J. Hartmann, S. Abu Ghazleh, N. Jansen **Data preparation:** N. Jansen, S. Abu Ghazleh, J. Hartmann **Analysis:** S. Kempe, S. Abu Ghazleh, J. Hartmann, N. Jansen **Results:** S. Abu Ghazleh, J. Hartmann, S. Kempe **Discussion:** J. Hartmann, S. Kempe, S. Abu Ghazleh, N. Jansen
Hartmann, J., **Jansen, N.**, Dürr, H.H., Harashima, A., Okubo, K. and Kempe, S., 2010. Predicting riverine dissolved silica fluxes into coastal zones from a hyperactive region and analysis of their first order controls. International Journal of Earth Sciences 99 (1), 207-230.	**Research Idea:** J. Hartmann **Analysis Framework:** J. Hartmann **Data preparation:** J. Hartmann, N. Jansen, K. Okubo, A. Harashima, H. H. Dürr **Analysis:** J. Hartmann, N. Jansen **Results:** J. Hartmann **Discussion:** J. Hartmann, A. Harashima
Hartmann, J., **Jansen, N.**, Dürr, H.H., Kempe, S. and Köhler, P., 2009. Global CO$_2$-consumption by chemical weathering: what is the contribution of highly active weathering regions? Global and Planetary Change 69 (4), 185-194.	**Research Idea:** J. Hartmann **Analysis Framework:** J. Hartmann **Data preparation:** N. Jansen, J. Hartmann, H. H. Dürr **Analysis:** J. Hartmann **Results:** J. Hartmann **Discussion:** J. Hartmann, S. Kempe
Hartmann, J., **Jansen, N.**, Kempe, S. and Dürr, H.H., 2007. Geochemistry of the river Rhine and the upper Danube: Recent trends and lithological influence on baselines. Journal of Environmental Science for Sustainable Society 1, 39-46.	**Research Idea:** J. Hartmann **Analysis Framework:** J. Hartmann **Data preparation:** J. Hartmann, N. Jansen, H. H. Dürr **Analysis:** J. Hartmann **Results:** J. Hartmann **Discussion:** J. Hartmann, S. Kempe